

Waves in Inhomogeneous Media

Proefschrift

ter verkrijging van de graad van doctor
aan de Technische Universiteit Delft,
op gezag van de Rector Magnificus Prof. dr. ir. J. T. Fokkema,
voorzitter van het College voor Promoties,
in het openbaar te verdedigen op dinsdag 20 maart 2007 om 15.00 uur

door

Sijmen GERRITSEN

natuurkundig ingenieur
geboren te Zevenaar.

Dit proefschrift is goedgekeurd door de promotor:
Prof. dr. ir. G. E. W. Bauer

Samenstelling van de promotiecommissie:

Rector Magnificus,	voorzitter
Prof. dr. ir. G. E. W. Bauer	Technische Universiteit Delft, promotor
Prof. dr. ir. C. P. A. Wapenaar	Technische Universiteit Delft
Prof. dr. Yu. V. Nazarov	Technische Universiteit Delft
Prof. dr. G. W. 't Hooft	Universiteit Leiden
Prof. dr. B. A. van Tiggelen	Centre National de la Recherche Scientifique, Grenoble, Frankrijk
Dr. J. M. Thijssen	Technische Universiteit Delft
Dr. M. S. Ferreira	Trinity College Dublin, Ierland

Het onderzoek in dit proefschrift is financieel ondersteund door de stichting voor Fundamenteel Onderzoek der Materie (FOM).



Published by: Sijmen Gerritsen
Printed by: Sieca Repro B.V., Delft
Casimir PhD Series, Delft-Leiden, 2007-01
ISBN/EAN: 978-90-8593-025-9

Copyright © 2007 by Sijmen Gerritsen
All rights reserved. No part of the material protected by this copyright notice may be reproduced or utilized in any form or by any means, electronic or mechanical, including photocopying, recording or by any information storage and retrieval system, without permission from the publisher.
Printed in the Netherlands

De woorden die hij prevelde waren niet te begrijpen, maar dat het belangrijke woorden waren, daar mogen we zeker van zijn.

Herman Brusselmans, *De man die werk vond*

PREFACE

This thesis is the result of the four memorable years I spent as a PhD student in the Theoretical Physics group at the TU Delft. It all began in the summer of 2002, when I came to Delft to apply for a position. Among some friendly PhDs, I met one professor who was disappointed to hear that I was not into video games, one professor who gave me a hard time during my presentation because I neglected localization effects in the explanation of my results (I had no idea what he was talking about), and an enthusiastic young postdoc who offered me a position in Israel, which was a perfectly safe place, she assured me several times. Gerrit Bauer (the video games professor) offered me a position on a joint project with the geophysics department to study classical waves in complex media. Improving methods to find oil using theoretical physics seemed like an interesting topic to work on. I decided to try my luck in Delft and started in the autumn of that year.

It quickly became clear to me that it would take quite some effort to turn an “natuurkundig ingenieur” with some experience in numerical calculations, and a bit of background in theoretical physics, into a full-fledged theoretician and a part-time geophysicist. Furthermore, shortly before I arrived in Delft, the department of Applied Physics had been reorganized and the theory group was now part of the department of Nanoscience. Trying to do classical physics with seismic waves on a kilometer scale, I was surrounded by people occupied with nanotubes, quantum noise and electron spin dynamics. It was a great opportunity to follow seminars in both the Nanoscience and the Geophysics departments, and to get acquainted with some of the main principles of these interesting fields and the new directions they are heading. Still, in this somewhat schizophrenic setting I sometimes got lost as well.

The past four years have definitely been all about “Strikes and gutters” (ups and downs), to quote The Dude. However, it has been great to get into contact with the incredibly rich field of waves in complex media and to discover that there are still many classical problems left to be solved. The excellent talks and discussion between (young) scientists from many different disciplines and

backgrounds at the “Imaging, Communication and Disorder” summer school in Corsica in June 2006, made it the absolute best “week at the office” for me as a PhD student. Maybe in the end, I only partially became that full-fledged theoretician and part-time geophysicist, but it has been worth the effort.

The fact that only my name is printed on the cover suggests that I managed to do the research and write this thesis all by myself. This could not be further from the truth. The main purpose of this preface is to acknowledge the persons that have in any way been involved in making the completion of this task easier. Before I mention anyone in particular, I have to thank the (very well organized) “Stichting Fundamenteel Onderzoek der Materie” (FOM) for paying my salary and providing excellent training opportunities for their PhDs.

So, let’s get personal (and all emotional). I am in many ways indebted to my supervisor Gerrit. Here I can mention his ability to manage the group, travel the world and supervise his students, all at the same time. Or say that he is an expert on the politics of academia and weird culinary traditions. However, besides his friendliness, I think his most admirable character trait is his patience. It looks like the guinea pig turned out alright in the end, and his willingness to give me time and space to learn from my mistakes is most to thank for that. Mauro should be thanked for sharing the recursive Green function code, having me over in Dublin and discussing the numerics. Jos probably does not know how important his involvement in my PhD was. It may not have seemed much to him, but his cooperation came at a time when it was much appreciated. His skills, but definitely also his friendliness and openness made it a pleasure to work with him. I want to thank Kees Wapenaar and Deyan for giving me some insight in the interesting world of geophysics and of seismic interferometry in particular. The user committee members of the STW project “Wave propagation, reflection and localization in inhomogeneous media” should be thanked for sitting through my talks and discussing my work during the meetings.

My other colleagues of the theory group were always (very) willing to listen when I was boring them with earthquakes and finding oil. I want to thank all staff members, postdocs, PhDs, and students, that shared the floor with me. Some of them I should mention in particular. It has been more than interesting to be in the same group as Yuli Nazarov. His ability to understand the essence of a physics problem in only one or two slides during a presentation never failed to amaze me. It was even more so a pleasure to discuss, and (dis)agree with him on topics unrelated to physics. I admire Miriam for her endless enthusiasm, the group is a more lively place because of it. I want to thank Yvonne for the numerous occasions she helped me out, and Yaroslav for being the group’s “Big Friendly Giant”.

Several PhD students in the group made the struggle a bit easier, by sharing the experience. I had a good start working in the same office as Oleg and Jens, a well-balanced couple. The Italian coffee breaks with Gabriele were nice, and there should have been more. Thanks to Jeroen and Xuhui the group remained a lively place after these people left. Fabian is way too enthusiastic and outspoken to become a good theoretical physicist, and it has been good to have him around, as long as he wasn't nagging about the weather (but do keep on telling yourself that everything is better in Switzerland). I have to thank Wouter for never stop being "nice guy Eddie", even when I was constantly mocking his elitist treehugger friends. Also, I really appreciate the fact that he eventually decided not to bail out on me and continued his PhD. Without Omar's LaTeX support I would never have been able to finish this thesis at all. More importantly, he is one of the most likeable idiots I have ever met (and I know quite a few). He hardly ever stopped talking since the day we both started to work in Delft, and I am very thankful for that (not for the chaos in our office, though).

Having friends outside (theoretical) physics has definitely been beneficial for my mental health. First of all, Fetsje and Eefje should be thanked, as their support enabled me to throw those strikes again. I want to thank the young doctors Gitte, Mohand, and Pi for sharing their experiences and frustrations. The epic journeys to Belgium with VriendenweekendTM were a great way to forget about the hardships of the PhD for a weekend. Jelle and Daaf should be thanked for the (sort of) weekly dinners, I hope many will follow. The TriathlistTM initiative was and is an excellent way to blow off steam, I want to thank Rob, Gert, and Susanne for participating. My good friends Bart, Niek, and Maarten should be thanked for not getting totally fed up with my complaints (or at least not showing it). My family has been a great support. I am proud of my brothers and sister, and I guess I could use some of Wannes' courage, Mathijs' pragmatism and Lieke's ability to combine ambition with a no-stress attitude to life. The sacrifices my parents made for us are remarkable, and there is no way in which I can thank them enough.

Still, there is only one person who is solely responsible for the fact that I managed to finish my PhD research and this thesis. I owe it all to Leonie. If she does not change her mind we will get married on the 27th of April this year. I consider myself to be quite lucky. Bedankt meisje!

Delft, February 2007

CONTENTS

1. <i>Introduction</i>	1
1.1 Waves and inhomogeneous media	1
1.2 Imaging with waves in inhomogeneous media	2
1.2.1 Imaging inhomogeneous media in geophysics	2
1.2.2 Diffuse optical tomography for medical imaging	7
1.3 Some principles of wave propagation	11
1.3.1 Wave equations in continuum mechanics, electromagnetism and quantum mechanics	11
1.3.2 Scattering, radiative transfer and diffusion	13
1.3.3 Point sources and interfaces	16
1.4 This thesis	20
2. <i>Diffusion of monochromatic classical waves</i>	25
2.1 Introduction	25
2.2 Definitions and basic equations	27
2.2.1 Microscopic equations	27
2.2.2 Macroscopic equations	29
2.3 Scattering matrices	29
2.4 The configuration-averaged propagator	31
2.5 The configuration-averaged intensity and energy	32
2.5.1 The Bethe-Salpeter equation	32
2.5.2 Energy conservation and the Ward identity	33
2.5.3 Flux	35
2.5.4 Intensity	36
2.5.5 Energy density	39
2.6 The diffusion constant	41
2.7 Time domain correlations in 3D media	44
2.8 Conclusions	46
2.9 Appendix: Energy and intensity in 2D	48

Contents

3.	<i>Diffuse wave propagation and interfaces</i>	55
3.1	Introduction	55
3.2	Classical wave transmission through point contacts	56
3.3	Energy transmission coefficients for wide contacts	61
3.3.1	The specular interface	61
3.3.2	The ideally diffuse interface	62
3.4	Interfaces between diffusive media	65
3.5	The thermal boundary resistance	68
3.6	Spin wave propagation through interfaces	69
4.	<i>Interfaces in diffuse imaging problems</i>	75
4.1	Introduction	75
4.2	Formulation of the imaging problem	75
4.3	Smooth boundary conditions on the intensity	77
4.4	Including interface scattering in the boundary conditions	79
4.5	Conclusions	82
5.	<i>Recursive Green functions for 2D disordered systems</i>	85
5.1	Introduction	85
5.2	Recursive Green functions in 1D	86
5.3	Recursive Green functions in 2D	89
5.4	Optimization and performance	93
5.4.1	Optimization of the lead surface Green function calculation	93
5.4.2	Convergence as a function of N_q and η	95
5.4.3	Numerical accuracy and scaling of the numerical costs	97
5.5	Results: Head waves and disordered interfaces	99
5.5.1	Headwaves and smooth interfaces	100
5.5.2	Head waves and rough interfaces	101
5.6	Conclusions and discussion	105

1. INTRODUCTION

1.1 Waves and inhomogeneous media

Waves are literally everywhere. We observe them when we get seasick, listen to music or open our eyes. We use them to communicate, heat food and to cheer sports heroes. Of all the waves around us, we are only able to sense a small amount by our eyes and ears and we usually do not recognize them as such. Still, any undergraduate physics student will acknowledge that there is hardly any field in physics in which wave motion does not play an important role.

A wave is a disturbance that propagates through space. In the case of a sound wave, “space” is a medium (gas, fluid or solid) and the disturbance is a change in local particle position or velocity. Electromagnetic field disturbances do not need support of a medium, but can travel through vacuum. However, they can propagate through and interact with matter. We refer to sound and electromagnetic waves with continuously varying amplitudes as classical (or massless) waves. Quantum mechanics is the fundamental theory for matter as well as fields. Quantum matter waves related to fundamental particles (electrons, for example) do carry mass and the amplitude of the wave function is not an observable quantity; its modulus squared is. On the other hand, both classical and quantum matter waves transport energy and (linear and angular) momentum. Furthermore, quantized fields, such as photons, phonons and magnons are in the classical limit described by wave equations that are similar to the equations that govern the wave nature of particles in the quantum limit. These analogies, that will be further discussed in this introduction, allow physicists to transfer a method or formalism developed in one field without too much labor to a totally different one.

Interactions with inhomogeneities in the medium alter the propagation direction, velocity or amplitude of waves. When energy is (not) conserved during these interactions, waves are scattered (in)elastically. In this thesis we restrict ourselves to elastic scattering processes, and refer to them simply as scattering. How a wave is scattered depends on the difference in constitutive parameters

(like the wave velocity) of the inhomogeneity with the reference medium, its shape and its size compared to the wavelength.

1.2 *Imaging with waves in inhomogeneous media*

When observing the world around us visually, our brain continuously creates images based on the information it receives from the receptors in our eyes. These receptors detect the intensity and frequency of light that was emitted by a source that reaches the eye via reflections from the objects around us. We are able to make useful images from light waves because their wavelength is much smaller than the objects we see and the medium between the objects and our eyes affects light wave propagation relatively weakly. To create images from objects that are not observable with the naked (or lens-assisted) eye, techniques have been and are being developed that make use of the same principles, i.e. a source emitting waves illuminating an object with reflections that are picked up by a detector. Digital data processing is then often used to convert the measured data into an image. In this thesis we address two examples of such imaging techniques: imaging with sound waves in seismic exploration and (earthquake) seismology to investigate the structure of the earth's subsurface and medical imaging using light to acquire information about biological tissue. The main differences between these imaging methods and imaging with our eyes are that here the wavelengths are not always smaller than the objects to be imaged and often the opacity of the medium between the object and the detector seriously affects wave propagation.

1.2.1 *Imaging inhomogeneous media in geophysics*

In seismic exploration, information about the earth's interior is acquired by detecting waves, originating from active (man-made) sources, that have propagated through the subsurface [1], while in seismology passive sources (earthquakes and noise from microseismic sources) are used for this purpose [2, 3]. In both fields this essentially yields information about the position dependence of properties such as the propagation velocity and the mass density. The conventional approach to seismic imaging is to treat the subsurface of the earth as a layered structure, where every layer is described by a certain set of parameters. Recorded arrival times and amplitudes of reflected pulsed signals are then used to reconstruct the properties of the layers. Unfortunately, this “inverse problem” has unique solutions only in very idealized situations, which makes its

1. Introduction

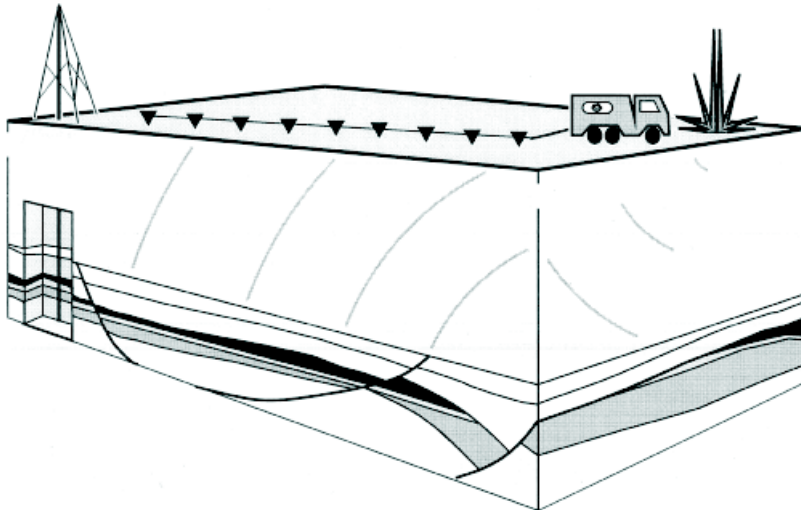


Fig. 1.1: Illustration of active seismic acquisition on land using a dynamite source and a cable of geophones. From Drikkoningen [4].

solution notoriously difficult when the underlying data set is incomplete and/or noisy.

An illustration of active seismic acquisition is shown in Fig. 1.1, where dynamite is used as a source and the reflected energy is detected by an array of geophones. The upper left panel of Fig. 1.2 shows a field seismic shot record from the geophones positioned at a certain offset from the source. The geophones record the ground movement from the time that the explosion creates a broadband pulse that propagates through the subsurface. From the arrival times of the reflected and refracted waves of which the travel paths are shown in the lower panels of Fig. 1.2, a subsurface model, with depth and wave propagation velocity of the layers, is deduced. The model of the near subsurface is shown in the middle of Fig. 1.2 and the model at larger depth is shown in the bottom. When this model is used to create a synthetic seismogram which is shown in the upper right panel, we can indeed recognize the reflection and refraction events in the original seismogram. However, it is clear that the original seismogram looks much more “noisy” than the synthetic one.

1.2. Imaging with waves in inhomogeneous media

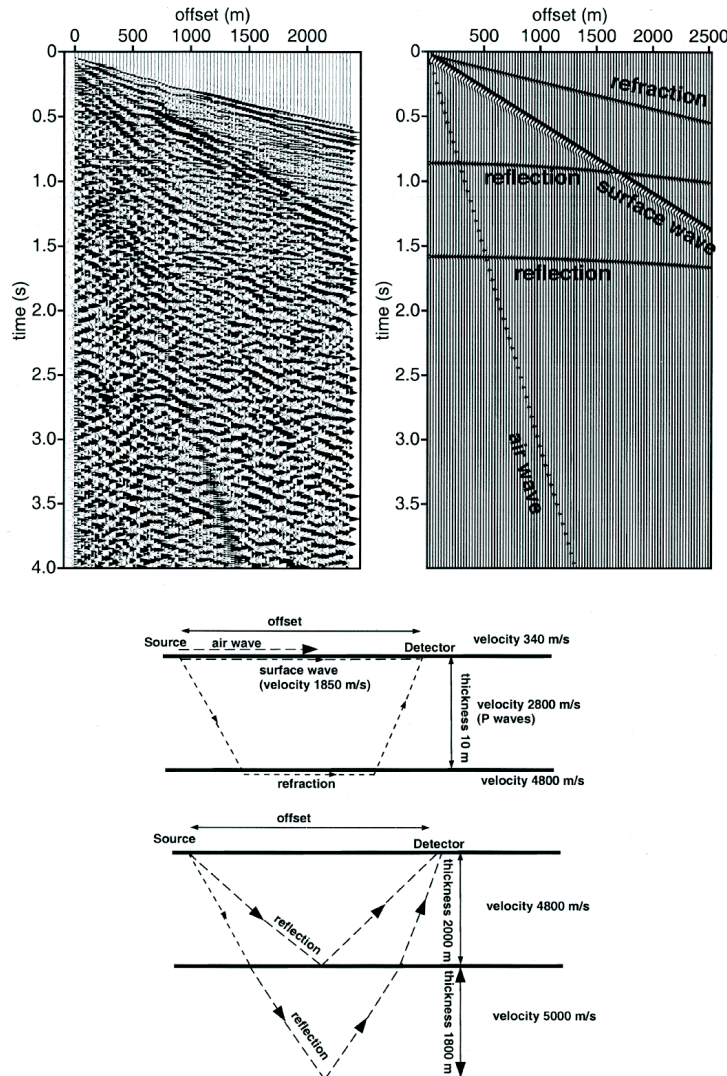


Fig. 1.2: Field seismic shot record from land survey (top left), its synthetic seismogram (top right) using the model of the near surface (middle) and at larger depths (bottom). From Driekoningen [4].

1. Introduction

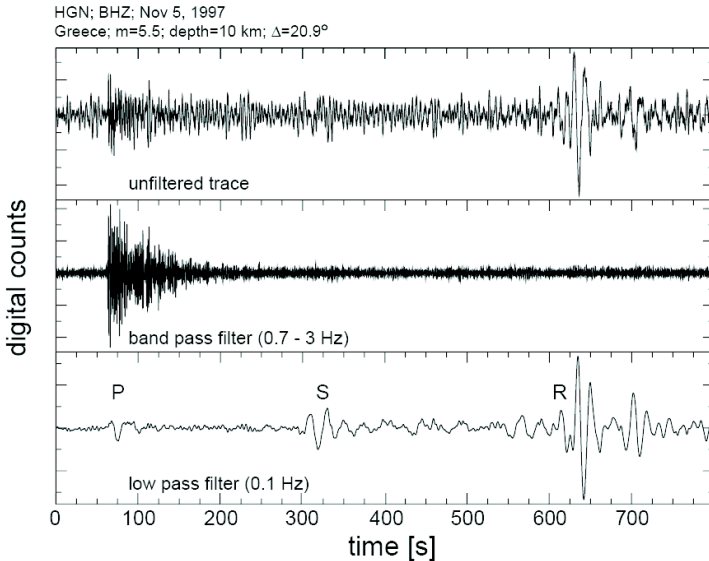


Fig. 1.3: Vertical ground motion recorded in The Netherlands after an earthquake in Greece (top panel). Also shown are the band-passed filtered seismogram (middle panel) and the low-passed filtered seismogram (bottom panel). From Snieder [6].

Deviations from the perfectly layered subsurface model, like lateral inhomogeneities, gradual changes in the constitutive parameters and roughness of the interfaces limit its applicability. In active seismic exploration of heterogeneous subsurface layers the extra scattering from these inhomogeneities shows up in the recorded time traces in the seismic records, where it can even completely mask the arrivals of the reflections and makes conventional imaging difficult. This is also the reason why the seismogram of Fig. 1.2 looks so irregular, although multiple reflections from the interfaces also contribute to this, but they can be corrected for. In seismology the scattered waves that follow the arrivals of directly propagated waves from earthquakes are known as coda waves [5]. An earthquake seismogram is shown in Fig. 1.3, where the ground movement in The Netherlands was recorded after an earthquake in Greece [6]. The top panel shows the unfiltered trace, while a low frequency filter shows the first

1.2. Imaging with waves in inhomogeneous media

arrival of the different modes of propagation (P for pressure, S for shear and R for Rayleigh (surface) waves) in the lowest panel. In the middle panel a filtered trace is shown, where the impulsive arrival is followed by a wave-train that is the so-called coda, which literally means “tail”.

The coda is caused by waves that have been delayed by multiple scattering [7]. As the (lateral) inhomogeneities in the subsurface responsible for the scattering are static, the coda is a deterministic signal [6]. The “noisy” looking data are therefore not stochastic in the sense that a second shot experiment for the setup that created the seismogram of Fig. 1.2 would yield (almost) the exact same result. Therefore, the multiply scattered coda contains information about the inhomogeneous medium that the waves traversed. One could even say that these waves contain even more information than the directly propagating waves, as they sampled a larger part of the medium. In order to image properties of distributions of inhomogeneities responsible for multiple scattering in the subsurface, we should relate them to coda properties by statistical methods.

Relating coda properties to medium properties is difficult, because the inhomogeneities can be both small and large compared to the wavelength [6]. Theories that describe (multiple) scattering are usually formulated for only one of the two regimes, as we will see in the following section. Tourin et al. [8] studied codas in laboratory experiments where ultrasonic transducers were used as sources and receivers and a water filled tank with iron wires modelled the multiple scattering system. For such disordered media with many similar scatterers with a size comparable to the wavelength, they showed that relatively simple diffusive models can be used to model the average intensity of the acoustic coda. However, such model experiments are not necessarily a good representation of the media that are responsible for the coda in seismograms. In the elastic subsurface, shear as well as pressure waves are present, mode conversions at boundaries have to be taken in to account, and the inhomogeneities can be very dissimilar. Margerin et al. [9] showed that the decay of the seismic coda (the coda Q) in earthquake data acquired in Mexico can be explained with a simple model of diffusively propagating elastic waves. The equipartitioning of energy of coda waves over the different elastic modes, a clear sign of multiple scattering in elastic inhomogeneous media, was calculated and measured by Hennino et al. [7]. Larose et al. [10] showed that interference of multiply scattered seismic waves can be observed, by measuring weak localization of seismic waves.

These studies gave strong evidence to support the theory that the seismic coda can be explained by multiple scattering of waves, instead of a combination of single scattering and absorption. Effective medium properties such as the Q-factor of the coda decay or the (average) mean free path can be derived from

1. Introduction

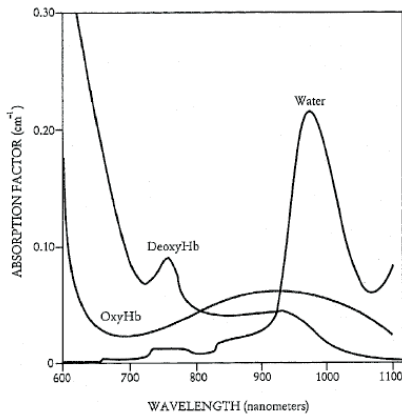
the averaged coda properties. However, it remains a challenge to extract more detailed information about the medium from seismic data sets, such as the frequency dependence of these properties. Besides the ongoing scientific interest in multiple scattering in seismic media, there is a huge economic incentive to study this topic. Squeezing more information out of data obtained by active seismic exploration could improve hydrocarbon reservoir characterization, giving more accurate information to limit the amount of unsuccessful (expensive) drilling operations before being able to successfully exploit a discovered reservoir.

1.2.2 *Diffuse optical tomography for medical imaging*

Medical doctors have several methods at their disposal to image biological tissue and the human body in particular. Three of these methods, projection radiography (x-rays), ultrasonography (ultrasound) [11], and optical tomography are based on imaging with waves with a source-detector setup. Radiography, and ultrasonography use waves that interact relatively weakly with the tissue so that multiple scattering of waves between source and object and object and receiver does not prohibitively perturb the image. Both methods have their limitations. Ionizing x-rays can damage tissue, while contrast between different types of (soft) tissue for this radiation is often low. Ultrasonography is limited by the low penetration through bone, and the high impedance mismatch with gas filled tissue (lungs). Furthermore, recording good quality ultrasound images requires highly skilled operators. Optical tomography, or diffuse optical tomography, uses near infrared (NIR) light waves for medical imaging and it works in a rather different way than radiography and ultrasonography. Here we discuss some basic principles, advantages and limitations of this technique.

In Fig. 1.4 in vitro absorption spectra of hemoglobin and water are plotted as a function of wavelength between 600 and 1100 nm. From this figure it can be seen that the absorption factor μ_a (the inverse of the absorption length) is low around 800 nm for three important constituents of biological tissue, i.e. water, oxygenated and deoxygenated hemoglobin [12]. Light in this NIR window can therefore be used to image biological tissue, which has great advantages, as light waves are not ionizing and they can be used for spectroscopy. However, there is one fundamental problem, as can be seen from the accompanying table to Fig. 1.4. In this table, the absorption factors and the scattering factors (μ_s , the inverse of the mean free path) are given at 780 and 820 nm, for different types of tissue. This shows that although absorption is low for these frequencies, light in tissue is scattered so strongly that a wave is scattered many times while crossing one cm of tissue. For most interesting medical imaging applications light

1.2. Imaging with waves in inhomogeneous media



Interaction of light and tissue

Tissue	Scattering factor $\mu_s'(\text{cm}^{-1})$	Absorption factor $\mu_a(\text{cm}^{-1})$	Number of samples
Human brain (820 nm)	17.5 (± 1)	0.04 (± 0.01)	33
Human breast (780 nm)	15 (± 2.3)	0.035 (± 0.01)	700
Rat brain (780 nm)	13.2 (± 0.8)	0.15 (± 0.02)	3
Rat white adipose tissue (780 nm)	18.6 (± 1.4)	0.07 (± 0.01)	5

Fig. 1.4: Plot of the absorption spectra of three important constituents of biological tissue: water, oxygenated and deoxygenated hemoglobin. The table shows the scattering and absorption factors in the NIR window for different types of tissue. From Yodh and Chance [12].

never travels directly from object to detector. NIR light propagates diffusively in biological tissue and imaging with diffuse signals requires a different approach compared to imaging with directly propagating waves. We discuss two practical examples of imaging with diffuse optical tomography (DOT), i.e. cancer tumor detection in breast tissue and studying the oxygenation of blood in the brain [13].

Conventional mammography (imaging of breast tissue) is done with (low-dose) x-rays. Besides the disadvantage of the radiation used (which prevents the method from being used for regular screening), the contrast between cancer and healthy tissue is not strong enough to detect all tumors (false-negatives). Furthermore, in a significant number of cases false-positives are reported, i.e. the imaging technique shows a tumor that is actually not there. Better and less damaging imaging techniques are therefore needed, and diffuse optical tomography appears to be a promising alternative, or at least a useful addition to existing methods [14].

When breast tissue is illuminated by an array of sources, the penetration depth of NIR light is up to 10 cm. In general, tumors contain more blood vessels than the surrounding tissue, and therefore the scattering and absorption properties

1. Introduction

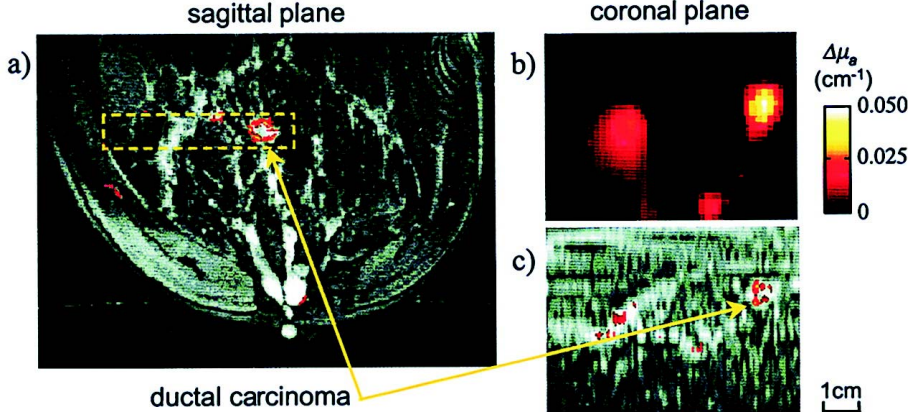


Fig. 1.5: (a) MRI image of a breast containing a ductal carcinoma (tumor). (b) DOT image of the volume of interest (dashed box in panel a), imaging plane perpendicular to the plane of the MRI image. Lighter regions represent higher scattering factor. (c) MRI image in the same plane as the DOT image. From Ntziachristos et al. [15].

of a tumor differ considerably from the surrounding medium. An array of detectors positioned on the breast measures the scattered light affected by the presence of a tumor. The measured data have to be processed to translate the properties of the scattered field into an image of the position dependence of the optical properties of the tissue. An example of an acquired image is shown in Fig. 1.5 [15]. Panel (a) shows an MRI image of a breast with an approximately 1 cm large tumor. The volume of interest, the dashed box in panel (a), is imaged with DOT perpendicular to the plane of the MRI image. This image is shown in panel (b), where the light region represents a different scattering parameter that coincides with the position of the tumor.

As light can propagate through bone, DOT can also be used for monitoring brain activity [13]. This application of DOT is based on the different absorptive properties of oxygenated and deoxygenated hemoglobin. Fig. 1.6 shows a setup to study the influence of electrical stimulation of a rat's forepaw on the oxygenation of the blood in its brain [16]. Arrays of fibers act as sources and detectors and the resulting spatially resolved DOT images are shown in Fig. 1.7. The relative increase in oxygenated hemoglobin and decrease in deoxygenated hemoglobin and a net increase of total hemoglobin caused by the stimulation

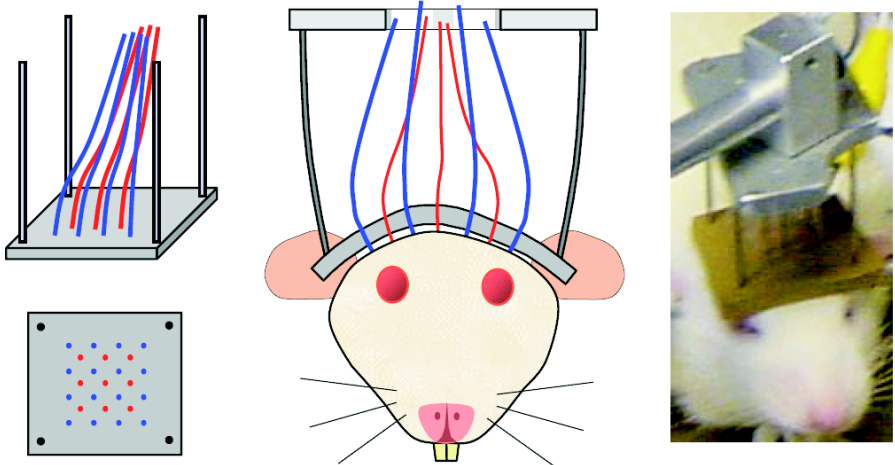


Fig. 1.6: Setup to study brain activity of rats using DOT. From Siegel et al. [16].

can be measured in this way. This is a non invasive and relatively inexpensive way to map brain functionality and it can just as well be used on human brains [17]. Furthermore, it can be used to image bleeding in the brain [18].

These two examples of possible applications show the potential of DOT for medical imaging purposes. We have not discussed how exactly the detected signals are processed into useful images. This is the difficult part of DOT, as the (diffuse) inverse problem that has to be solved is ill-defined. This means that relatively large changes in the multiple scattering medium might only have a small effect on the detected scattered field. What is problematic is that the imaged tissue is in general a complex medium, containing not only many small scatterers, but also larger objects, interfaces and boundaries with homogeneous media. Forward modelling of these media with a priori knowledge of the medium under study is already challenging and a lot of effort was and is being invested into modelling diffuse wave propagation and reconstructing scattering media from the information of the scattered field [18, 19, 20]. In order to further improve imaging with DOT, more studies of wave propagation in inhomogeneous media are needed, preferably leading to relatively straightforward formalisms and descriptions. In the following section we discuss some of the basic principles used to describe wave propagation in inhomogeneous media.

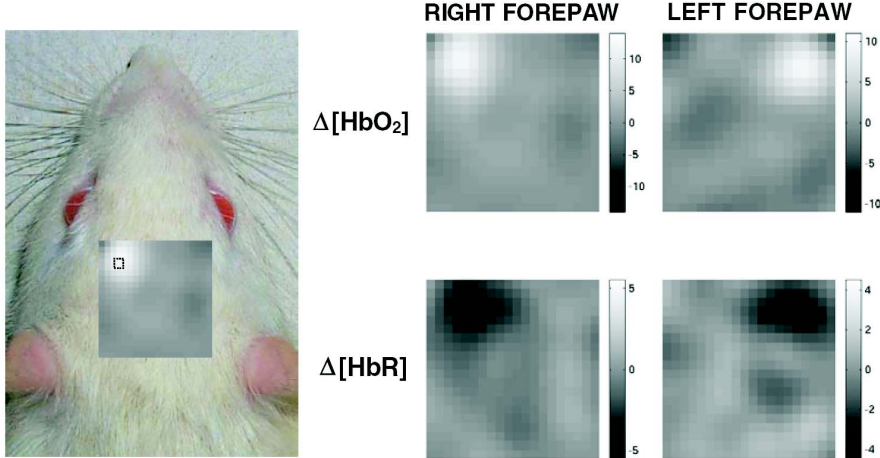


Fig. 1.7: DOT image of rat brain activity resulting from forepaw stimulation. Change in levels of oxygenated and deoxygenated hemoglobin show where the brain activity is high as a result of the stimulation. From Siegel et al. [16].

1.3 Some principles of wave propagation

1.3.1 Wave equations in continuum mechanics, electromagnetism and quantum mechanics

In a homogeneous, unbounded, isotropic, elastic medium, the displacement $\mathbf{u}(\mathbf{r}; t)$ originating from a bodyforce $\mathbf{f}(\mathbf{r}; t)$ is described by [3]

$$\rho \partial_t^2 \mathbf{u} = \mathbf{f} + (\lambda + 2\mu) \nabla (\nabla \cdot \mathbf{u}) - \mu \nabla \times (\nabla \times \mathbf{u}), \quad (1.1)$$

where ρ is the mass density of the medium and λ and μ are the Lamé moduli that are obtained from the stress-strain relations. The displacement \mathbf{u} can be expressed in terms of the scalar potential ψ and the vector potential ϕ by $\mathbf{u} = \nabla \psi + \nabla \times \phi$, with $\nabla \cdot \phi = 0$ and Eq. (1.1) then reduces to two independent wave equations. One that describes the propagation of the pressure or P-wave component with a particle displacement parallel to the propagation direction

$$\partial_t^2 \psi = \frac{\Psi}{\rho} + \alpha^2 \nabla^2 \psi, \quad (1.2)$$

1.3. Some principles of wave propagation

and one that describes the propagation of the two shear (S-)wave modes with a particle displacement perpendicular to the propagation direction

$$\partial_t^2 \phi = \frac{\Phi}{\rho} + \alpha^2 \nabla^2 \phi. \quad (1.3)$$

Here $\alpha = \sqrt{(\lambda + 2\mu)/\rho}$, and $\beta = \sqrt{\mu/\rho}$ are the P- and S-wave velocities, and Ψ and Φ are related to the bodyforce by $\mathbf{f} = \nabla \Psi + \nabla \times \Phi$. In a liquid $\mu = 0$ and only the P-wave polarization exists. We redefine $\psi = -\rho_0 \partial_t \phi$ and write

$$\nabla^2 \psi(\mathbf{r}; t) - \frac{1}{c_0^2} \partial_t^2 \psi(\mathbf{r}; t) = -\rho_0 Q(\mathbf{r}; t), \quad (1.4)$$

so that the amplitude is related to the pressure by $p = \partial_t \psi$ and to the local particle velocity by $\mathbf{v} = -\rho_0^{-1} \nabla \psi$. c_0 and ρ_0 are the acoustic wave velocity and the mass density of the homogeneous medium. Formulated in this way, the source term on the right hand side is a volume injection (an explosion, for example), which is related to the body force by $Q = -\partial_t \Psi / (c_0^2 \rho_0)$.

When the mass density in an acoustic medium can be considered constant, but the wave velocity is inhomogeneous, then c_0 in Eq. (1.4) is just replaced by a position dependent velocity $c(\mathbf{r})$ to describe waves in inhomogeneous media. By Fourier transforming the wave equation in the frequency domain, one obtains for a given frequency ω , in the absence of a source term

$$[-\nabla^2 + V(\mathbf{r}; \omega)] \psi(\mathbf{r}; \omega) = E(\omega) \psi(\mathbf{r}; \omega), \quad (1.5)$$

where $E(\omega) = \omega^2/c_0^2$, and a “scattering potential”

$$V(\mathbf{r}; \omega) = \frac{\omega^2}{c_0^2} \left(1 - \frac{c_0^2}{c^2(\mathbf{r})} \right), \quad (1.6)$$

is introduced, where c_0 is now a reference velocity. This means that scattering of classical waves is frequency dependent, and we further discuss this in the next subsection.

The Maxwell equations govern all classical electromagnetic phenomena. They can be summarized by two uncoupled wave equations [21]

$$\nabla^2 \Phi - \frac{1}{c^2} \partial_t^2 \Phi = -\frac{\rho}{\epsilon_0}, \quad (1.7)$$

$$\nabla^2 \mathbf{A} - \frac{1}{c^2} \partial_t^2 \mathbf{A} = -\mu_0 \mathbf{J}, \quad (1.8)$$

1. Introduction

that describe the propagation of electromagnetic waves in vacuum. Here the potentials Φ and \mathbf{A} are related to the electric field by $\mathbf{E} = -\nabla\Phi - \partial_t\mathbf{A}$ and to the magnetic flux density $\mathbf{B} = \nabla \times \mathbf{A}$. ρ is the charge density, \mathbf{J} the current density, ϵ_0 and μ_0 the vacuum permittivity and permeability and c the propagation speed. In the absence of source terms (\mathbf{J}, ρ) this yields two modes in which the magnetic flux and electric field components are perpendicular. The analogy between these equations and Eqs. (1.2)-(1.3) that describe the propagation of sound waves is clear.

For electrons in a potential V , the time-independent Schrödinger equation [22]

$$\left[-\frac{\hbar^2}{2m} \nabla^2 + V(\mathbf{r}) \right] \psi_E(\mathbf{r}) = E\psi_E(\mathbf{r}) \quad (1.9)$$

is the eigenvalue equation for the electron states with energy E . The analogy to the classical wave equation in the frequency domain (Eq. (1.5)) is obvious. However, the amplitude of the wavefunctions is not an observable. Another difference is that the potential does not depend on energy for the electrons, whereas the impurity potential for classical waves does depend on frequency.

1.3.2 Scattering, radiative transfer and diffusion

We first discuss scattering of acoustic waves in the frequency domain, where inhomogeneities are described by the impurity potential $V(\mathbf{r}; \omega)$ given by Eq. (1.5). Let us take a system with a single finite region with wave velocity different from the surrounding medium (but equal mass density), and assume that this velocity changes abruptly from one value to the other (on a lengthscale much smaller than the wavelength). Incoming and outgoing solutions of the homogeneous wave equations in the frequency domain can then be matched by the appropriate boundary conditions. This is the basic principle of scattering theory. When the density is allowed to vary as well, and/or shear modes are supported, this principle is still applicable, although the boundary conditions are formulated differently and mode conversion has to be taken into account.

When one medium with wave velocity c_i is embedded in another medium with velocity c_0 an incoming plane wave with wave vector $\kappa_0 = \omega/c_0$ is scattered, giving rise to a total wave field that, sufficiently far from the embedded object, is [22]

$$\psi_{tot}(\mathbf{r}; \omega) \propto e^{i\kappa_0 \cdot \mathbf{r}} + f_{\kappa_0}(\hat{\mathbf{r}}) \frac{e^{i\kappa_0 r}}{r}, \quad (1.10)$$

the sum of the unperturbed and scattered contributions (here the origin is taken

at the center of the scatterer). The angular dependence of the scattered amplitude is described by $f_{\kappa}(\hat{\mathbf{r}})$. When the scatterer is spherical f_{κ} is a function of the polar angle θ only. When it furthermore has a radius a much smaller than the wavelength the scattered contribution does not depend on angles at all and

$$f_{\kappa}(\hat{\mathbf{r}}) = f_0 = \frac{e^{-2i\kappa_0 a}}{\kappa_0} \left(\frac{\kappa_0}{\kappa_i \cot \kappa_i a - i\kappa_0} - e^{i\kappa_0 a} \sin \kappa_0 a \right), \quad (1.11)$$

where $\kappa_i = \omega/c_i$. For larger spherical scatterers waves are scattered preferentially in the forward direction. When the scatterer (and the curvature of its surface) are much larger than the wavelength, scattering can be described by ray theory, which is the acoustic equivalent of geometric optics. Calculating the scattered field is most difficult when the size of the scatterer is of the order of the wavelength, the regime where Mie theory has to be applied [23].

When two or more scatterers are embedded in the reference medium the total wave field is a superposition of the incoming wave and an infinite series of multiply scattered terms. Numerical results can be obtained by numerical integration of the wave equation. Exact analytic calculations become prohibitively complex soon, which means that approximation schemes become necessary. The multiply scattered response to an incoming wave depends on the exact configuration of the inhomogeneities. However, for large systems containing many scatterers, the responses for different realizations of the impurity configuration show similarities. Because of this ergodicity, statistical methods can be employed to study transport properties in these systems. Averaging over all the possible impurity ensembles yields an analytical formalism to study properties like the averaged amplitude and intensity and it couples the microscopic scattering equations to the macroscopic wave field properties [24]. A common approximation within this formalism is the independent scatterer approximation that neglects phase effects (interference of multiply scattered waves), which is appropriate when the density of scatterers is sufficiently low [8]. Using this approximation one finds that the configuration-averaged amplitude drops exponentially with a transport mean free path, related to the propagation of unscattered and forward scattered waves, or the coherent part of the wave field. The transport mean free path is the length scale over which all phase information is lost. It is equal to the scattering mean free path (average distance between successive scatterings) only when scattering is isotropic [25]. Information about the scattered waves is obtained from the configuration-averaged intensity using the ladder approximation to the Bethe-Salpeter equation [24], a topic that is discussed in more detail in chapter two of this thesis.

1. Introduction

Another way to study the intensity of multiply scattered waves is by solving the radiative transfer equation [23, 26]. It describes the propagation of the specific intensity \mathcal{I} at position \mathbf{r} travelling in direction \mathbf{n} and is equivalent to the Boltzmann equation for (elementary) particles. It neglects the phase of the waves. For time and position dependent problems the RTE becomes [27]

$$\ell_{sc} \mathbf{n} \cdot \nabla \mathcal{I}(\mathbf{r}, \mathbf{n}, t) + t_{sc} \partial_t \mathcal{I}(\mathbf{r}, \mathbf{n}, t) = \frac{1}{4\pi} \int d\mathbf{n}' p(\mathbf{n}; \mathbf{n}') \mathcal{I}(\mathbf{r}, \mathbf{n}', t) - \mathcal{I}(\mathbf{r}, \mathbf{n}, t). \quad (1.12)$$

The last term on the right-hand side is the specific intensity leaving a small volume around \mathbf{r} in direction \mathbf{n} , whereas the first term on that side describes the intensity that is scattered from direction \mathbf{n}' into direction \mathbf{n} with probability p . The terms on the left-hand side take the spatial and time variations into account. ℓ_{sc} is the scattering mean free path and t_{sc} the scattering time. The RTE is often the basis of Monte-Carlo type simulations of multiply scattered waves, for example for modelling the seismic coda [5, 9], or imaging with diffuse optical tomography [19]. Solving the RTE for monochromatic sources (the frequency domain) is in fact equivalent to solving the Bethe-Salpeter equation in the ladder approximation [27].

The local intensity I and the local intensity current \mathbf{J} are obtained by integrating out the specific direction of propagation

$$I(\mathbf{r}, t) = \int d\mathbf{n} \mathcal{I}(\mathbf{r}, \mathbf{n}, t), \quad \mathbf{J}(\mathbf{r}, t) = \frac{t_{sc}}{\ell_{sc}} \int d\mathbf{n} \mathcal{I}(\mathbf{r}, \mathbf{n}, t) \mathbf{n}. \quad (1.13)$$

When the current is small compared to the density, it can then be derived from the RTE that processes changing slowly in time are described by Fick's laws [27]

$$\mathbf{J}(\mathbf{r}, t) = -D \nabla I(\mathbf{r}, t), \quad (1.14)$$

and

$$\partial_t I(\mathbf{r}, t) = D \nabla^2 I(\mathbf{r}, t), \quad (1.15)$$

where only elastic scattering processes are considered. It means that the propagation of intensity becomes a diffusive process, with a diffusion constant D . For a 3D medium

$$D = \frac{1}{3} c_{\text{eff}} \ell_{tr}, \quad (1.16)$$

where ℓ_{tr} is the transport mean free path and $c_{\text{eff}} = \ell_{sc}/t_{sc}$ is the effective transport velocity [25].

1.3. Some principles of wave propagation

We started this section by describing single scattering events in the frequency domain. When the RTE is formulated in the time domain like in Eq. (1.12), the frequency dependence of the scattering mean free path and the scattering time (and thus of the scattering potential V defined by Eq. (1.5)) are disregarded. If we think of a time dependent source as a superposition of monochromatic sources, it is easy to see that such an approximation is only justified when the source is a narrowband pulse. Disregarding frequency dependence in time-dependent problems is often the only workable approximation, as it is too difficult to develop analytical formalisms that treat (broadband) pulse propagation taking all frequency dependent scattering properties into account.

The formalisms describing multiple scattering briefly reviewed here all rely on the assumption that interference of multiply scattered waves can be neglected. It is a useful assumption, for example, when one wants to calculate the average transmitted intensity through a scattering material. However, when one takes a better look at the scattered intensity, one finds that it consists of darker and brighter spots, so called speckles [24]. When looking at the backscattered intensity, it can be shown that constructive interference between reciprocal scattering paths enhances the averaged backscattered intensity around the source by a factor of two [24]. This has been verified experimentally for light waves [28], acoustic waves [29], and even seismic waves [10]. Constructive interference is known to limit the conductance of one-, and two-dimensional electronic conductors in mesoscopic physics, a prediction made by Anderson [30]. Interestingly enough, it was his work on the subject of strong (or Anderson) localization in electron transport that directed the attention of wave physicists to the subject of localization in the first place. Observing localization of light in 3D (strongly) scattering systems, has been a hot topic and source of debate during the last two decades [31]. Neither the properties of speckle patterns, nor localization effects can be described by formalisms that neglect phase effects. However, it is an appropriate approximation for most of the topics addressed in this thesis.

1.3.3 Point sources and interfaces

Let us close this section by discussing scattering of spherical and cylindrical waves at interfaces between semi-infinite homogeneous media. In particular, we want to introduce the concept of refracted head waves. Consider a point or line source in a 3D half-space characterized by a wave velocity c_1 positioned at a distance $z_0 > 0$ from an interface with another half-space with wave velocity $c_2 (> c_1)$ that emits spherical or cylindrical waves as depicted in Fig. 1.8. We only consider pressure modes. Waves hitting the surface are either reflected back

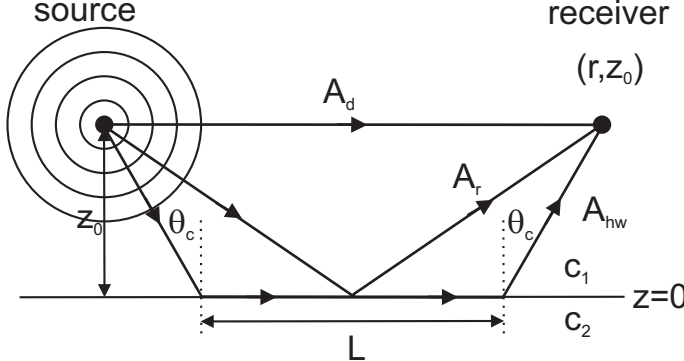


Fig. 1.8: Schematic representation of the travel paths of the direct waves (A_d), reflected waves (A_r) and head waves (A_{hw}) emitted by a cylindrical (2D) or spherical (3D) point source in the upper half space of two fluid half spaces characterized by wave velocities c_1 and c_2 ($> c_1$).

into the upper medium, or refracted into the lower lying medium. When the wave velocity in the lower lying medium is higher, refracted waves propagating along the boundary in this medium travel faster than the reflected waves on the other side. The interaction between the refracted waves and the boundary creates an upward travelling critically refracted or head wave. When the direct reflection between the source and the receiver placed at (r, z) has an angle of incidence less than the critical angle $\theta_c = \arcsin(c_1/c_2)$, only the direct reflection (labelled by A_r) is observed. For higher angles, refracted head waves travelling along the path labelled by A_{hw} in Fig. 1.8 are observed. The speed of propagation of these waves along the interface is the same as that of the lower medium. The signal from a pulsed source is therefore observed before the arrival of the directly reflected waves (A_r), when L is large enough. For very large L the head wave arrival even precedes the direct arrival (A_d).

The first exact description of these waves was published by Lamb in 1904 [32] and the reflection and refraction of spherical waves is therefore also referred to as “Lamb’s problem”. When one of the two half-spaces is elastic, i.e. shear waves are also supported, Rayleigh and Love waves (interface waves with an exponentially decaying amplitude with the distance from the interface) are present as well, but we restrict ourselves to solutions of the scalar wave equation here.

The starting point for an exact description of head wave propagation is the

1.3. Some principles of wave propagation

inhomogeneous wave equation [3]. The corresponding Green function equation

$$(\nabla^2 - c^{-2}(\mathbf{r}) \partial_t^2) G(\mathbf{r}, \mathbf{r}'; t) = \delta(\mathbf{r} - \mathbf{r}') \delta(t), \quad (1.17)$$

describes the response of the system to a point source in \mathbf{r}' , sending out a δ pulse at time $t = 0$. In terms of Green functions the response at a receiver at $(r, z > 0)$ can be written as $G_{tot} = G_0 + G_r$, where G_0 is the solution in the homogeneous medium and G_r describes both the reflected and the refracted waves. For an infinitely extended line source, the system is effectively two-dimensional. G_r in the frequency domain is then given by the integral expression

$$G_r((r, z), (0, z_0); \omega) = \frac{i}{2\pi} \int_0^\infty dp \frac{\cos(p\omega r)}{\sqrt{c_1^{-2} - p^2}} \frac{\sqrt{c_2^{-2} - p^2} - \sqrt{c_1^{-2} - p^2}}{\sqrt{c_2^{-2} - p^2} + \sqrt{c_1^{-2} - p^2}} \times e^{i\omega\sqrt{c_1^{-2} - p^2}(z_0 + z)}. \quad (1.18)$$

The Fourier transform of Eq. (1.17) into the time domain can be carried out analytically by the Cagniard-De Hoop method [33]

$$\begin{aligned} & G_r((r, z), (0, z_0); t) \\ &= \text{Im} \left\{ \frac{\sqrt{c_2^{-2} - p^2} - \sqrt{c_1^{-2} - p^2}}{\sqrt{c_1^{-2} - p^2} + \sqrt{c_2^{-2} - p^2}} \right\} \frac{\Theta(t - t_{hw}) - \Theta(t - R_0/c_1)}{2\pi\sqrt{t^2 - R_0^2/c_1^2}} \\ & \quad + \text{Re} \left\{ \frac{\sqrt{c_2^{-2} - p^2} - \sqrt{c_1^{-2} - p^2}}{\sqrt{c_1^{-2} - p^2} + \sqrt{c_2^{-2} - p^2}} \right\} \frac{\Theta(t - R_0/c_1)}{2\pi\sqrt{t^2 - R_0^2/c_1^2}}, \end{aligned} \quad (1.19)$$

where $R_0^2 = r^2 + (z_0 + z)^2$, Θ is the Heaviside step function and

$$p = \begin{cases} \frac{xt - (z_0 + z)\sqrt{R_0^2/c_1^2 - t^2}}{R_0^2} & \text{for } t \leq R_0/c_1, \\ \frac{xt + i(z_0 + z)\sqrt{t^2 - R_0^2/c_1^2}}{R_0^2} & \text{for } t \geq R_0/c_1. \end{cases}$$

The first term of Eq. (1.19) vanishes when the source-receiver distance in the horizontal plane is such that $r/R_0 \leq c_1/c_2$. Above a critical distance when $r/R_0 > c_1/c_2$ this first term describes headwaves with an arrival time of $t_{hw} = r/c_2 + \cos\theta_c(z + z_0)/c_1$. An example of a response from a narrow angle reflection ($\theta < \theta_c$) is shown in the upper panel of Fig. 1.9 where the reflected

1. Introduction

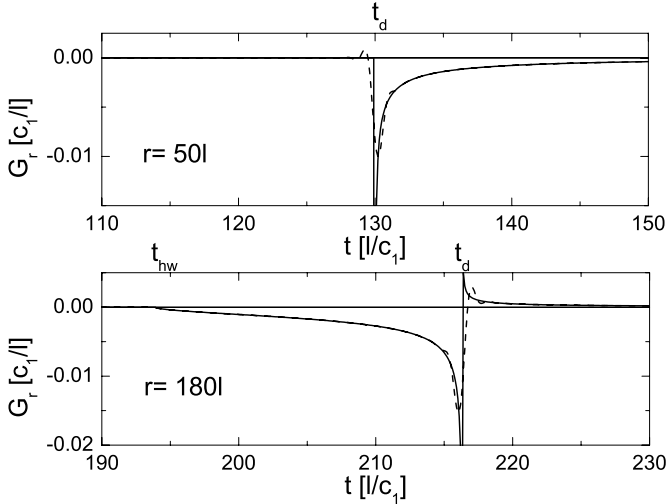


Fig. 1.9: Plot of the reflected response G_r as a function of time t for a narrow angle reflection ($\theta = \arctan(5/12)$, upper panel) and a wide angle reflection ($\theta = \arctan(9/6)$, lower panel). The solid line is the response to a delta function pulse in the time domain, whereas the dashed line shows a response to a wider pulse. Both source and receiver are positioned 60 unit lengths l from the interface between the upper medium with wave velocity c_1 and the lower medium with $c_2 = 2c_1$.

response G_r is plotted as a function of time in units of l/c_1 , where l is the unit length. Both source and receiver are positioned at a distance $z_0 = z = 60l$ from the interface to the second medium with wave velocity $c_2 = 2c_1$. When the source receiver distance is $50l$, a reflected pulse is observed (solid line for the infinite band, dashed line for a band-limited pulse) with an arrival time t_d , the travel time of directly reflected waves. In the lower panel of this figure a wide angle response is plotted when $r = 180l$. In this case a stretched head wave with arrival time t_{hw} is observed before the arrival of the primary reflection.

For point sources instead of line sources the head waves have the same travel time t_{hw} and their amplitude attenuates with the source receiver distance as $r^{-1/2}L^{-3/2}$ [3]. In earthquake data these arrivals can, for example, be traced

back to the Mohorovičić discontinuity, the interface between the earth's crust and mantle. Travel times and amplitudes are used to extract data on the lower lying medium. However, interface roughness and other inhomogeneities influence head wave propagation.

1.4 *This thesis*

In this thesis we study the theory of wave propagation in inhomogeneous media in search for answers to some questions in the field of waves in complex media, both on a fundamental level and from the point of view of the imaging applications discussed in the previous sections. In general, we restrict ourselves to scalar waves and media that are inhomogeneous in a sense that the constitutive parameters change on length scales much smaller than the wavelength such as sharp interfaces and small scale impurities. Throughout this thesis we use scattering theory to describe wave propagation in these systems and disregard absorption effects. These effects can be included at the cost of more complexity, but they do not alter the basic physics that we are interested in. Although much of the work is done with acoustic waves in mind, the results apply to any type of classical scalar waves. We intend to describe properties of wave propagation in inhomogeneous media in terms of relatively simple physical pictures and straightforward analytical and numerical models. The results are discussed in the next four chapters.

In chapter 2 wave propagation in one-, two and three-dimensional homogeneously disordered media is described. Here the media are considered to be infinitely large and filled with many randomly distributed similar scatterers that have a finite size smaller than the wavelength and a different wave velocity compared to the surrounding medium. The configuration-averaged intensity from a monochromatic point source in this medium as a function of distance from the source is calculated analytically, to investigate the transition from coherent to diffusive wave propagation. Furthermore, energy transport in these systems is described and the frequency dependence of properties like the mean free path, diffusion constant and effective energy transport velocity is discussed. We derive how general properties of the inhomogeneous medium, like the medium-scatterer wave velocity ratio can be obtained from the properties of the scattered wave-field.

In chapter 3 we apply the Landauer-Büttiker formalism that was originally developed to describe electronic currents in mesoscopic structures to classical waves. We use it to discuss diffuse energy currents through interfaces and yield

1. Introduction

a formalism that treats transport through interfaces between diffusive media in terms of an interface resistance. We show how analogies between different types of wave propagation can be exploited and apply this formalism to the thermal boundary resistance and the transport of spin waves (magnons). In chapter 4 we apply the concept of the interface resistance to a diffuse imaging problem, i.e. locating and characterizing a diffusive object embedded in a diffusive slab. When a refractive index mismatch between object and medium is present, interfaces affect the imaging process and they can be described by our formalism. Potentially this description could be applied to medical imaging of biological tissue.

The fifth and final chapter of this thesis deals with a numerical method, the recursive Green function technique, to solve the classical wave equation in two-dimensional layered media with lateral disorder. This method has been used frequently to calculate electronic transport in (disordered) metals and semiconductors and we demonstrate that it can also be applied to classical wave propagation problems in 2D by studying the influence of interface roughness on head wave propagation.

References

- [1] R.E. Sheriff, and L.P. Geldart, *Exploration Seismology*, (Cambridge University Press, 1995).
- [2] F.A. Dahlen, and J. Tromp, *Theoretical Global Seismology*, (Princeton University Press, 1998).
- [3] K. Aki, and P.G. Richards, *Quantitative Seismology*, (University Science Books, Sausalito, 2002).
- [4] G.G. Drijkoningen, *Introduction to Reflection Seismology*, (Lecture Notes, Technical University Delft, 2002).
- [5] H. Sato, and M.C. Fehler, *Seismic Wave Propagation and Scattering in the Heterogeneous Earth*, (Springer-Verlag, New York, 1998).
- [6] R. Snieder, in *Diffuse Waves in Complex Media*, edited by J.P. Fouque (Kluwer, Dordrecht, 1999).
- [7] R. Hennino, N. Trégourès, N.M. Shapiro, L. Margerin, M. Campillo, B.A. van Tiggelen, and R.L. Weaver, Phys. Rev. Lett. **86**, 3447 (2001).
- [8] A. Tourin, M. Fink, and A. Derode, Waves in Random Media **10**, R31 (2000).
- [9] L. Margerin, M. Campillo, N.M. Shapiro, and B. van Tiggelen, Geophysics Journal International **136**, 343 (1999).
- [10] E. Larose, L. Margerin, B.A. van Tiggelen, and M. Campillo, Phys. Rev. Lett. **93**, 048501 (2004).
- [11] F.J. Fry, *Ultrasound: Its Applications in Medicine and Biology* (Elsevier, Amsterdam, 1978).
- [12] A. Yodh, and B. Chance, Physics Today **48**, 34 (1995).

References

- [13] D.A. Boas, D.H. Brooks, E.L. Miller, C.A. DiMarzio, M. Kilmer, R.J. Gaudette, and Q. Zhang, IEEE Signal Processing Magazine **18**, 57 (2001).
- [14] B.W. Pogue, S.P. Poplack, T.O. McBride, W.A. Wells, K. Sunshine Osterman, U.L. Osterberg, and K.D. Paulsen, Radiology **218**, 261 (2001).
- [15] V. Ntziachristos, A.G. Yodh, M. Schnall, and B. Chance, Proc. Natl. Acad. Sci. USA **97**, 2767 (2000).
- [16] A.M. Siegel, J.P. Culver, J.B. Mandeville, and D.A. Boas, Physics in Medicine and Biology **48**, 1391 (2003).
- [17] J.C. Hebden, Psychophysiology **40**, 501 (2003).
- [18] A.P. Gibson, J.C. Hebden, and S.R. Arridge, Physics in Medicine and Biology **50**, R1 (2005).
- [19] S.R. Arridge, Inverse Problems **15**, R41, (1999).
- [20] S.B. Colak, D.G. Papaioannou, G.E. 't Hooft, M.B. van der Mark, H. Schomberg, J.C.J. Paasschens, J.B.M. Melissen, and N.A.A.J. van Asten, Appl. Opt. **36**, 180 (1997).
- [21] J.D. Jackson, *Classical Electrodynamics*, (Wiley, New York, 1998).
- [22] E. Merzbacher, *Quantum Mechanics* (Wiley, New York, 1961).
- [23] H.C. van de Hulst, *Multiple Light Scattering*, (Academic Press, New York, 1980).
- [24] P. Sheng, *Introduction to Wave Scattering, Localization and Mesoscopic Phenomena* (Academic Press, New York, 1995).
- [25] A. Lagendijk, and B.A. van Tiggelen, Physics Reports **270**, 143 (1996).
- [26] A. Ishimaru, *Wave Propagation and Scattering in Random Media*, (Academic Press, New York, 1978).
- [27] M.C.W. van Rossum, and Th.M. Nieuwenhuizen, Rev. Mod. Phys. **71**, 313 (1999).
- [28] M.P. van Albada, and A. Lagendijk, Phys. Rev. Lett. **55**, 2692 (1985).
- [29] A. Tourin, A. Derode, P. Roux, B.A. van Tiggelen, and M. Fink, Phys. Rev. Lett. **79**, 3637 (1997).

References

- [30] P.W. Anderson, Phys. Rev. **109**, 1492 (1958).
- [31] D.S. Wiersma, P. Bartolini, A. Lagendijk, and R. Righini, Nature **390**, 671 (1997).
- [32] H. Lamb, Phil. Trans. R. Soc. London **A203**, 1 (1904).
- [33] A.T. de Hoop, Applied Science Research **B8**, 349 (1960).

2. DIFFUSION OF MONOCHROMATIC CLASSICAL WAVES

2.1 *Introduction*

The ongoing interest in the field of classical waves in complex media is caused by the importance of detection and imaging techniques based on wave propagation and scattering. This ranges from electromagnetic waves in optical and near infrared tomography [1] and microwave radars [2] to acoustic waves in ultrasonics [3] and geophysics [4]. Complexity is often associated with inhomogeneities that cause scattering which considerably complicates most imaging processes. However, when used cleverly, the scattered field can also be used to improve imaging [5]. Although length scales (with respect to the wavelength) and the degree of the disorder may vary considerably from field to field, methods and results have been shown to be interchangeable without much difficulty [6]. Recent topics of interest include localization of classical waves [7, 8], the transition from ballistic to diffusive wave propagation [9, 10], acoustic time-reversal imaging [11], etc. Direct simulation by the exact solution of a well-known Helmholtz wave equation for a given realization of the medium is often the method of choice for given applications. The drawbacks of the brute force computational approach are the limited system size and statistics that can be achieved with given computer resources as well as the difficulty to distill general principles out from the plethora of output data. The need for simple models with transparent results therefore remains.

An analytic theory of wave propagation in disordered media necessarily relies on simple model scatterers, for which point scatterers, i.e. (regularized) δ functions in real space, are often chosen [12, 13]. Unfortunately, the scattering response of a single point scatterer can become non causal, a pathological behavior that can not be solved by a simple momentum cutoff [14]. Especially for the study of the frequency dependence over a wider range it is therefore necessary to use more realistic model scatterers.

In this chapter we study a simple but not unrealistic experiment for the determination of the scattering properties of scalar waves in a disordered bulk

2.1. Introduction

material. A signal is emitted by a source and detected by a receiver, both embedded in the medium at sufficiently large distances from the boundaries. Ultimately, we are interested in the detector signal caused by a pulsed (broad-band) signal emitted by the source. After a first arrival we then expect the so-called coda that arrives at later times due to multiple scattering at the random scatterers [15]. However, combining both the effects of multiple scattering and the full frequency dependence of the scattering processes renders an analytical treatment difficult without additional approximations, such as a complete neglect of the frequency dependence of the scattering amplitudes when fitting the diffusive halo. In order to understand how to justify certain approximations and eventually find better ones, we have carried out a study of the frequency dependence of the scattering properties of random media. We concentrate on the steady state in the presence of strictly monochromatic sources, which distinguishes the present work from related studies of the propagation of narrow band pulses [16, 17]. As main results we obtain the frequency dependence of macroscopic effective medium properties such as the mean free path and the diffusion constant that depend on the microscopic parameters of the random scatterers.

When the ratio between source-receiver distance and mean free path is small, wave propagation is predominantly ballistic. When this ratio is large, energy and intensity propagation is governed by the diffusion equation [13, 16]. Both these regimes are well understood. However, many imaging applications operate on length scales where the mean free path and the source-receiver distance are comparable. This is especially the case in geophysics where mean free paths range from a few hundred meters up to tens of kilometers [18]. The behavior at this crossover regime between ballistic and diffuse wave (intensity) propagation is of considerable interest [9] and also subject of the present study.

In this chapter we present an analytical formalism on monochromatic wave intensity and energy propagation in one-dimensional, two-dimensional and three-dimensional (3D) homogeneously disordered media using realistic model scatterers. We develop our formalism in real space, using a point source assumption, instead of incoming plane waves, an approach that is more natural for acoustic waves, but not often used in this field [19]. We determine the relative contributions of diffusively and coherently propagated waves as the source-receiver distance increases. We did not find many theoretical studies of wave propagation in two dimensional random media in the literature [6, 10, 20], although several experiments on quasi-2D systems have been carried out [10, 16, 21]. Another possible test for our 2D theory is comparison with numerical studies, which for very large systems are much cheaper than in the 3D case.

The remainder of this chapter is organized as follows. In sections 2.2-2.4 we start by defining our model system and the basic equations, addressing the scattering matrices of single scatterers and discussing the average amplitude propagators in the frequency domain. The intensity, energy flux, and energy density are discussed in section 2.5. Results on the frequency dependence of the diffusion constant and its dependence on the model parameters are discussed in section 2.6. In section 2.7 (that is not part of Ref. [22]) we discuss how the time-domain autocorrelator can be obtained from the results in the frequency domain. Generally, the results for 1D systems are easily obtained, whereas our results for 3D systems agree with findings previously reported by others. The mathematics in the 2D case is not trivial, however, and the derivations are summarized in the Appendix. We end with the conclusions.

2.2 Definitions and basic equations

2.2.1 Microscopic equations

We describe the propagation of (scalar) acoustic waves in a microscopic model system. Specifically, we consider a 1D, 2D, or 3D acoustic medium with wave velocity c_0 and a mass density ρ_0 . The medium contains n randomly distributed scatterers per unit length, area, or volume and we treat the dilute limit in which the average distance between scatterers is much larger than their radius a . The internal wave velocity of a scatterer is c_{int} and, for simplicity, the difference in mass density with the surrounding medium is disregarded. The waves are emitted by a monochromatic point source oscillating at frequency ω positioned at the origin. The wave amplitude ψ_ω , related to the pressure by $p_\omega = \partial_t \psi_\omega$ and to local particle velocity by $\mathbf{v}_\omega = -\rho_0^{-1} \nabla \psi_\omega$, then obeys the wave equation

$$(\nabla^2 - c^{-2}(\mathbf{r}) \partial_t^2) \psi_\omega(\mathbf{r}; t) = -Q \rho_0 \delta^{(d)}(\mathbf{r}) \cos(\omega t). \quad (2.1)$$

The source term chosen here corresponds to a volume injection term, with $\delta^{(d)}$ the Dirac delta function and d the dimension. The source emits plane waves for 1D, cylindrical waves for 2D and spherical waves for 3D media. In all cases Q is in units of length per unit time. The wave velocity profile of the entire medium $c(\mathbf{r})$ contains the information of the positions of the scatterers (in 1D $\mathbf{r} = x$).

The Green function of the Helmholtz equation (2.1) in the real space and frequency domain reads

$$(\nabla^2 + \kappa_0^2 - V(\mathbf{r}; \omega)) G(\mathbf{r}, \mathbf{r}'; \omega) = \delta^{(d)}(\mathbf{r} - \mathbf{r}'), \quad (2.2)$$

2.2. Definitions and basic equations

where $\kappa_0 = \omega/c_0$, the length of the wave vector in the homogeneous medium. $V(\mathbf{r}; \omega)$ is the scattering or impurity potential, a sum over all individual scattering potentials

$$V(\mathbf{r}; \omega) = \kappa_0^2 (1 - \gamma^{-2}) \sum_{i=1}^N \Theta(a - |\mathbf{r} - \mathbf{r}_i|). \quad (2.3)$$

Θ is the Heaviside step function, with $\Theta(x) = 0$ when $x < 0$ and 1 otherwise. The velocity contrast is defined as $\gamma = c_{int}/c_0$ so that the single scatterer potential is “attractive” when $\gamma < 1$ and “repulsive” when $\gamma > 1$. Eq. (2.3) describes a spherical potential, however, the precise shape is not relevant when the scatterers are sufficiently small compared to the wave length.

The amplitude of the wave field is related to the Green function

$$\psi_\omega(\mathbf{r}; t) = -Q\rho_0 \operatorname{Re} \{e^{-i\omega t} G(\mathbf{r}, \mathbf{r}' = 0; \omega)\}. \quad (2.4)$$

The intensity $I_\omega(\mathbf{r}; t)$ is the square of this expression. Related physical properties are the energy flux

$$\mathbf{F}_\omega(\mathbf{r}; t) = -\frac{1}{\rho_0} \partial_t \psi_\omega(\mathbf{r}; t) \nabla \psi_\omega(\mathbf{r}; t), \quad (2.5)$$

and the energy density

$$W_\omega(\mathbf{r}; t) = \frac{1}{2\rho_0} \left((\nabla \psi_\omega(\mathbf{r}; t))^2 + c^{-2}(\mathbf{r}) (\partial_t \psi_\omega(\mathbf{r}; t))^2 \right), \quad (2.6)$$

recognized as the sum of the potential and kinetic energy contributions respectively. For a monochromatic source with frequency ω these observables contain a time independent contribution and a second term oscillating with frequency 2ω . We concentrate on the constant part by time averaging over one period. Expressed in terms of the Green function this yields

$$I_\omega(\mathbf{r}) = \frac{Q^2 \rho_0^2}{2} |G(\mathbf{r}, \mathbf{r}' = 0; \omega)|^2, \quad (2.7)$$

$$\mathbf{F}_\omega(\mathbf{r}) = -\frac{Q^2 \rho_0 \omega}{2} \operatorname{Im} \{G(\mathbf{r}, \mathbf{r}' = 0; \omega) \nabla G^*(\mathbf{r}, \mathbf{r}' = 0; \omega)\}, \quad (2.8)$$

$$W_\omega(\mathbf{r}) = \frac{Q^2 \rho_0}{4} \left(|\nabla G(\mathbf{r}, \mathbf{r}' = 0; \omega)|^2 + \frac{\omega^2}{c^2(\mathbf{r})} |G(\mathbf{r}, \mathbf{r}' = 0; \omega)|^2 \right). \quad (2.9)$$

2.2.2 Macroscopic equations

The properties of the wave field depend, via the Green function, on the exact configuration of scatterers. However, in large systems, different realizations of the ensemble give similar responses (ergodicity). The similarities in the response can be studied by calculating the configurational average. This average is the connection between the microscopic description and the macroscopic (effective) medium properties.

The macroscopic (diffusively scattered) intensity of pulsed sources is sometimes described by the diffusion equation

$$\partial_t \langle I(\mathbf{r}; t) \rangle = D \nabla^2 \langle I(\mathbf{r}; t) \rangle, \quad (2.10)$$

where the brackets denote the configuration average and D is the diffusion constant. In spite of neglecting the frequency dependence of the diffusion constant in this case, this approximation is known to work well in cases where the source receiver distance is much larger than the mean free path and the incoming pulse is a narrowband signal [13, 16]. In the case of a narrowband pulse, one can also write a transport equation for a wave packet with some inner and outer frequencies. In this way the frequency dependence of D can be derived [17].

In order to obtain the steady-state diffuse intensity of a monochromatic wave field, the diffusion equation (2.10) is insufficient. The energy density (and not the intensity) of the wave field is the conserved property. Eq. (2.10) is therefore only valid if the intensity is strictly proportional to the energy density. In general, the averaged energy transport is governed by Fick's first law

$$\langle \mathbf{F}_\omega(\mathbf{r}) \rangle = -D(\omega) \nabla \langle W_\omega(\mathbf{r}) \rangle, \quad (2.11)$$

accounting for the frequency dependence of the diffusion constant. In the steady-state problem and outside the monochromatic source the proper Laplace equation is

$$\nabla^2 \langle W_\omega(\mathbf{r}) \rangle = 0. \quad (2.12)$$

2.3 Scattering matrices

Here we discuss the properties of a single model scatterer in the system ($N = 1$ in Eq. (2.3)). The response of a system containing a monochromatic source (in the origin), a receiver (at \mathbf{r}) and a single “s-wave” scatterer (at \mathbf{r}_i) can be expressed in terms of Green functions of the homogeneous system ($V = 0$) [23]:

$$G(\mathbf{r}, \mathbf{r}' = 0; \omega) = G_0(r; \omega) + G_0(|\mathbf{r} - \mathbf{r}_i|; \omega) t_0(\omega) G_0(r; \omega). \quad (2.13)$$

2.3. Scattering matrices

This expression is valid in the far field limit ($r, r_i \gg \lambda$) and when scattering is isotropic ($\lambda \gg a$), where λ is the wavelength.

The transition (t-) matrix elements for s-wave scattering are related to the scattering matrix elements by

$$t_0(\omega) = \begin{cases} 2i\kappa_0 R(\omega) & (1D), \\ 2i(S_0(\omega) - 1) & (2D), \\ 2\pi i\kappa_0^{-1}(S_0(\omega) - 1) & (3D). \end{cases} \quad (2.14)$$

In 1D, the s-wave scattering condition corresponds to equivalence of t_0 for either reflection or transmission. $R(\omega)$ is the reflection coefficient at a step discontinuity, and can be obtained by imposing flux conservation across the scatterer boundary. This gives [24]

$$R(\omega) = e^{-i\kappa_0 2a} \frac{R_0(1 - e^{i\kappa_0 4a/\gamma})}{1 - R_0^2 e^{i\kappa_0 4a/\gamma}}, \quad (2.15)$$

where $R_0 = (\gamma - 1) / (\gamma + 1)$. By imposing the same condition we can derive an expression for the scattering matrix element of the s-wave channel S_0 (related to the scattering phase shift δ_0 by $S_0 = \exp(i2\delta_0)$). In 2D [25]

$$S_0(\omega) = -\frac{\gamma J_0(\kappa_0 a/\gamma) H_1^{(2)}(\kappa_0 a) - J_1(\kappa_0 a/\gamma) H_0^{(2)}(\kappa_0 a)}{\gamma J_0(\kappa_0 a/\gamma) H_1^{(1)}(\kappa_0 a) - J_1(\kappa_0 a/\gamma) H_0^{(1)}(\kappa_0 a)}. \quad (2.16)$$

In 3D the Bessel (J_i) and Hankel ($H_i^{(j)}$) functions are replaced by the spherical Bessel (j_i) and Hankel ($h_i^{(j)}$) functions. The scattering matrix element then simplifies to [24]

$$S_0(\omega) = e^{-i2\kappa_0 a} \frac{\cot(\kappa_0 a/\gamma) + i\gamma}{\cot(\kappa_0 a/\gamma) - i\gamma}. \quad (2.17)$$

In this calculation of the scattering matrices, the difference in mass density is disregarded. However, including this does not fundamentally alter the calculation (the scattering matrix is still calculated from flux conservation). Furthermore, the scattering matrices calculated here describe acoustic wave scattering where only acoustic modes are allowed inside the scatterers. When solid scatterers are considered extra mode conversions from acoustic waves to shear waves back to acoustic waves occur which considerably complicates the calculation. In principle, this calculation can be done [26] and it is known that the extra mode conversions cause extra resonances in scattering properties of the scattering object [27].

2.4 The configuration-averaged propagator

Now we switch to the case of multiple scattering at the proposed model scatterers. The wave propagator in a disordered medium after configuration averaging is dressed with a self-energy Σ . In reciprocal space it reads [13]

$$\langle G(\mathbf{k}, \mathbf{k}'; \omega) \rangle = \frac{1}{\kappa_0^2 - \mathbf{k}^2 - \Sigma(\mathbf{k}; \omega)} (2\pi)^d \delta^{(d)}(\mathbf{k} - \mathbf{k}'). \quad (2.18)$$

When n , the density of scatterers, is low, interference between multiply scattered waves by different sites may be disregarded. In this “single site approximation” the self-energy does not depend on \mathbf{k} and it is simply given by [13]

$$\Sigma(\omega) = nt_0(\omega). \quad (2.19)$$

This approximation does not restrict the scattering strength since t_0 is the full scattering matrix of the single scatterer. Interference effects from multiple scattering at different scatterers cause localization known to be important in 1D (where the localization length is of the order of the mean free path) and in 2D media (where the localization length is a transcendental function of the mean free path). In 3D, localization can be disregarded except for very strong scattering media [7]. Here we restrict ourselves to purely non-localized transport phenomena, bearing in mind that we can always find a region where this type of transport is dominant.

Fourier transforming Eq. (2.18) with self-energy given by Eq. (2.19) to real space gives the averaged Green function that depends only on the source-receiver distance ($G(r; \omega) = \langle G(\mathbf{r}, \mathbf{r}' = 0; \omega) \rangle$). In 1D the amplitude propagators are exponentially damped plane waves

$$G(|x|; \omega) = \frac{1}{2i\kappa_e(\omega)} e^{i\kappa_e(\omega)|x|}, \quad (2.20)$$

in 2D they are cylindrical:

$$G(r; \omega) = \begin{cases} -\frac{i}{4} H_0^{(1)}(\kappa_e(\omega)r) & \text{if } \omega > 0, \\ \frac{i}{4} H_0^{(2)}(-\kappa_e(\omega)r) & \text{if } \omega < 0, \end{cases} \quad (2.21)$$

and in 3D spherical

$$G(r; \omega) = \frac{-1}{4\pi r} e^{i\kappa_e(\omega)r}, \quad (2.22)$$

[6]. In Eqs. (2.20-2.22) κ_e is the “renormalized” effective wave vector

$$\kappa_e(\omega) = \sqrt{\kappa_0^2 - nt_0(\omega)} \equiv \text{sgn}(\omega) \kappa_r(\omega) + i \frac{1}{2\ell_f(\omega)}. \quad (2.23)$$

$\kappa_r(\omega) = |\text{Re}\{\kappa_e(\omega)\}|$ and $\ell_f^{-1}(\omega) = 2|\text{Im}\{\kappa_e(\omega)\}|$, the mean free path. We retrieve the Green functions for the homogeneous systems (G_0) by letting n or t_0 go to zero. Properties of the averaged response to a pulsed signal can be studied by calculating the Fourier transform to the time domain, as was done in Refs. [14] and [28].

2.5 The configuration-averaged intensity and energy

We derive here the configuration averaged intensity, energy flux and energy density in the frequency domain.

2.5.1 The Bethe-Salpeter equation

Ensemble averaging the intensity of Eq. (2.7) gives us

$$\langle I_\omega(\mathbf{r}) \rangle = \frac{Q^2 \rho_0^2}{2} \Pi(r; \omega), \quad (2.24)$$

where $\Pi(r; \omega) = \langle |G(\mathbf{r}, \mathbf{r}' = 0; \omega)|^2 \rangle$ is the average of the squared Green function propagator. It is given by

$$\begin{aligned} \Pi(r; \omega) &= \Pi_0(r; \omega) + \int d^d \mathbf{r}_1 d^d \mathbf{r} d^d \mathbf{r}_3 d^d \mathbf{r}_4 \langle G(\mathbf{r}, \mathbf{r}_1; \omega) \rangle \langle G^*(\mathbf{r}, \mathbf{r}_2; \omega) \rangle \\ &\quad \times \Gamma(\mathbf{r}_1, \mathbf{r}_2, \mathbf{r}_3, \mathbf{r}_4; \omega) \langle G(\mathbf{r}_3, \mathbf{r}' = 0; \omega) G^*(\mathbf{r}_4, \mathbf{r}' = 0; \omega) \rangle. \end{aligned} \quad (2.25)$$

This is the Bethe-Salpeter equation in position space, where Π_0 is the coherent intensity ($\Pi_0 = |G\rangle|^2$) and Γ is the irreducible vertex function. The lowest order approximation that still accounts for multiple scattering is

$$\Gamma(\mathbf{r}_1, \mathbf{r}_2, \mathbf{r}_3, \mathbf{r}_4; \omega) = n\Gamma(\omega) \delta^{(d)}(\mathbf{r}_1 - \mathbf{r}_3) \delta^{(d)}(\mathbf{r}_1 - \mathbf{r}_2) \delta^{(d)}(\mathbf{r}_3 - \mathbf{r}_4), \quad (2.26)$$

reducing the Bethe-Salpeter equation to

$$\Pi(r; \omega) = \Pi_0(r; \omega) + n\Gamma(\omega) \int d^d \mathbf{r}_1 \Pi_0(|\mathbf{r} - \mathbf{r}_1|; \omega) \Pi(r_1; \omega). \quad (2.27)$$

In reciprocal space this integral equation becomes a geometric series that can be summed as

$$\Pi(k; \omega) = \frac{\Pi_0(k; \omega)}{1 - n\Gamma(\omega)\Pi_0(k; \omega)}. \quad (2.28)$$

In order to be able to calculate the Fourier transform of $\Pi(k; \omega)$, an expression for $\Pi_0(k; \omega)$ is needed. It is calculated as the Fourier transform of the coherent intensity and this results in 1D in

$$\Pi_0(k; \omega) = \frac{2\ell_f^3}{\left((2\kappa_r\ell_f)^2 + 1\right)\left((k\ell_f)^2 - 1\right)}, \quad (2.29)$$

in 2D in

$$\Pi_0(k; \omega) = \frac{\ell_f^2}{\pi} \frac{\arcsin\left(\frac{\sqrt{(2\kappa_r\ell_f)^2 - (k\ell_f)^2}}{\sqrt{1 + (k\ell_f)^2}}\right)}{\sqrt{1 + (k\ell_f)^2}\sqrt{(2\kappa_r\ell_f)^2 - (k\ell_f)^2}}, \quad (2.30)$$

and in 3D in [13]

$$\Pi_0(k; \omega) = \frac{\ell_f}{4\pi} \frac{\arctan(k\ell_f)}{k\ell_f}. \quad (2.31)$$

The calculation of the vertex function Γ is discussed in the next subsection.

2.5.2 Energy conservation and the Ward identity

It is well known that for a given approximation for the self-energy, the vertex correction cannot be freely chosen. Here we take advantage of the flux conservation constraint to obtain Γ without additional microscopic calculations. The energy flux from the monochromatic source (on average) points outwards. In the steady state case the following condition must hold for the averaged flux in direction \mathbf{n} :

$$\langle \mathbf{n} \cdot \mathbf{F}_\omega(\mathbf{r}) \rangle \propto \frac{1}{r^{d-1}} \mathbf{n} \cdot \hat{\mathbf{r}}, \quad (2.32)$$

where $\hat{\mathbf{r}}$ is the unit vector in the radial direction. In 1D this condition reads

$$\langle F_\omega(x) \rangle \propto \text{sgn}(x). \quad (2.33)$$

The microscopic expression for the average energy flux is

$$\begin{aligned} \langle \mathbf{n} \cdot \mathbf{F}_\omega(\mathbf{r}) \rangle &= -\frac{Q^2 \rho_0 \omega}{2} \text{Im} \{ \langle G(\mathbf{r}, \mathbf{r}' = 0; \omega) \mathbf{n} \cdot \nabla G^*(\mathbf{r}, \mathbf{r}' = 0; \omega) \rangle \} \\ &= -\frac{Q^2 \rho_0 \omega}{2} \text{Im} \left\{ \Pi'(\mathbf{r}; \omega) \right\}, \end{aligned} \quad (2.34)$$

which defines the function $\Pi'_0(\mathbf{k}; \omega)$. The vertex function is the same as for the intensity, so we can express Π'_0 in reciprocal space as

$$\Pi'_0(\mathbf{k}; \omega) = \frac{\Pi'_0(\mathbf{k}; \omega)}{1 - n\Gamma(\omega)\Pi_0(k; \omega)}. \quad (2.35)$$

$\Pi'_0(k; \omega)$ is the coherent energy flux in direction \mathbf{n} that is given by the Fourier transform of

$$\Pi'_0(\mathbf{r}; \omega) = G(r; \omega)\mathbf{n} \cdot \nabla G^*(r; \omega). \quad (2.36)$$

In 2D and 3D the averaged microscopic expression for the energy flux should match the macroscopic condition

$$\text{Im} \left\{ \Pi'_0(\mathbf{r}; \omega) \right\} = -\frac{C}{r^{d-1}}\mathbf{n} \cdot \hat{\mathbf{r}}, \quad (2.37)$$

which in reciprocal space reads

$$\text{Re} \left\{ \Pi'_0(\mathbf{k}; \omega) \right\} = -(\mathbf{n} \cdot \hat{\mathbf{k}})2^{d-1}\pi\frac{C}{k}, \quad (2.38)$$

where C is real and depends on frequency and the model parameters. $\Pi_0(k; \omega)$ is an even function of k . We know how $\Pi'_0(\mathbf{k}; \omega)$ depends on k , as the Fourier transform in 2D reads

$$\Pi'_0(\mathbf{k}; \omega) = -(\mathbf{n} \cdot \hat{\mathbf{k}})2\pi i \int_0^\infty dr J_1(kr) r G(r; \omega) \partial_r G^*(r; \omega), \quad (2.39)$$

and in 3D

$$\Pi'_0(\mathbf{k}; \omega) = -(\mathbf{n} \cdot \hat{\mathbf{k}})4\pi i \int_0^\infty dr j_1(kr) r^2 G(r; \omega) \partial_r G^*(r; \omega). \quad (2.40)$$

The Taylor series of $\Pi'_0(\mathbf{k}; \omega)$ around $k = 0$ only contains odd terms. So, in the limit that $k \rightarrow 0$, condition (2.38) can only be fulfilled by Eq. (2.35) when

$$n\Gamma(\omega) = \Pi_0^{-1}(k = 0; \omega). \quad (2.41)$$

In 1D showing that condition (2.33) can only be fulfilled when Eq. (2.41) is fulfilled as well is straightforward. The Ward identities are relations between self-energy and vertex corrections. We can identify Eq. (2.41) as the Ward identity for our problem. We now have all the ingredients to calculate the Fourier transform of Eqs. (2.28) and (2.35) to calculate the averaged intensity and energy flux respectively.

2.5.3 Flux

Using the Taylor expansions in the limit $k \rightarrow 0$, we find an expression for C (from Eq. (2.37)) in 2D and 3D:

$$C = \frac{\int_0^\infty dr \operatorname{Im} \{G(r; \omega) \partial_r G^*(r; \omega)\} r^d d^{-1}}{\frac{1}{2} \Pi_0^{-1}(k=0; \omega) \partial_k^2 \Pi_0(k; \omega)|_{k=0}}. \quad (2.42)$$

The average flux in 1D is obtained by directly Fourier transforming Eq. (2.35):

$$\langle F_\omega(x) \rangle = \frac{Q^2 \rho_0 |\omega|}{8} \frac{\kappa_r}{\kappa_r^2 + 1/(2\ell_f)^2} \operatorname{sgn}(x). \quad (2.43)$$

We show how to calculate C in 2D case in the Appendix. With the result, the projection of the average flux becomes

$$\langle \mathbf{n} \cdot \mathbf{F}_\omega(\mathbf{r}) \rangle = \frac{Q^2 \rho_0 |\omega|}{8\pi^2} \frac{\arctan(2\kappa_r \ell_f)}{r} \mathbf{n} \cdot \hat{\mathbf{r}}, \quad (2.44)$$

while in 3D calculating C from Eq. (2.42) is straightforward and the projection of the average flux then reads

$$\langle \mathbf{n} \cdot \mathbf{F}_\omega(\mathbf{r}) \rangle = \frac{Q^2 \rho_0 |\omega|}{2} \frac{\kappa_r}{(4\pi)^2 r^2} \mathbf{n} \cdot \hat{\mathbf{r}}. \quad (2.45)$$

Letting $\ell_f \rightarrow \infty$ ($\kappa_r \rightarrow |\kappa_0|$) recovers the flux of a monochromatic source in an unperturbed medium.

It is interesting to see that, in contrast to the 3D case, in 1D and 2D the average flux depends on both the mean free path and the real part of the effective wave vector. So the scattering mean free path limits the energy flux in 1D and 2D, but not in 3D. In a strongly scattering 2D medium, in which the wave energy is not (yet) localized, the dependence on the arctangent should be observable.

2.5.4 Intensity

The total average intensity is proportional to the propagator $\Pi(r; \omega)$, which can be obtained by calculating the Fourier transform

$$\Pi(r; \omega) = \int \frac{d^d \mathbf{k}}{(2\pi)^d} \frac{e^{i\mathbf{k} \cdot \mathbf{r}}}{\Pi_0^{-1}(k; \omega) - \Pi_0^{-1}(k=0; \omega)}. \quad (2.46)$$

$\Pi_0(k)$ is given by Eq. (2.29) in 1D, Eq. (2.30) in 2D, and Eq. (2.31) in the 3D case. In 1D and 2D this integral diverges because in the steady state case with a monochromatic source, energy does not escape fast enough to infinity due to the scatterers. This is analogous to the fact that the Poisson equation (the diffusion equation in steady state with source term) for a line or planar source has no well-defined solution.

The gradient of the intensity exists in all cases. In 1D it is constant and the derivative of $\Pi(x; \omega)$ is given by

$$\partial_x \Pi(x; \omega) = -\text{sgn}(x) \frac{1}{4\ell_f} \frac{1}{\kappa_r^2 + 1/(2\ell_f)^2}. \quad (2.47)$$

The gradient of Π in 2D is expressed as an integral by

$$\nabla \Pi(r; \omega) = -\hat{\mathbf{r}} \int_0^\infty \frac{dk}{2\pi} \frac{k^2 J_1(kr)}{\Pi_0^{-1}(k; \omega) - \Pi_0^{-1}(k=0; \omega)} \equiv \hat{\mathbf{r}} f(r; \omega),$$

which defines a function $f(r; \omega)$, that represents the gradient in the $\hat{\mathbf{r}}$ direction. We split this up into a coherent (*coh*) and a “totally diffusive” (*td*) part and a crossover correction (*cr*)

$$f(r; \omega) = f_{coh}(r; \omega) + f_{td}(r; \omega) + f_{cr}(r; \omega). \quad (2.48)$$

The coherent part is connected to the unscattered intensity, therefore

$$\begin{aligned} f_{coh}(r; \omega) &= \partial_r |G(r; \omega)|^2 \\ &= -\frac{1}{8} \text{Re} \left\{ (\kappa_r + i/2\ell_f) H_1^{(1)}((\kappa_r + i/2\ell_f)r) H_0^{(2)}((\kappa_r - i/2\ell_f)r) \right\}. \end{aligned} \quad (2.49)$$

In the Appendix it is shown that

$$f_{td}(r; \omega) = -\frac{\arctan(2\kappa_r \ell_f)}{\pi^2 2\kappa_r \ell_f} \frac{1}{r} g^{-1}(2\kappa_r \ell_f), \quad (2.50)$$

with

$$g(2\kappa_r\ell_f) = 1 - \frac{1}{(2\kappa_r\ell_f)^2} + \frac{1}{2\kappa_r\ell_f \arctan(2\kappa_r\ell_f)}. \quad (2.51)$$

This part decays as $1/r$, much slower than the coherent and crossover contributions. It is the part that describes the intensity gradient when energy transport is completely governed by Fick's first law, so we refer to this term as the “totally diffusive” part. When the total gradient is approximated by the just the sum of the coherent and the totally diffusive contribution, the gradient first decays exponentially until the source-receiver distance is approximately two to three mean free paths and then the $1/r$ decay is dominant. However, in this approximation it is neglected that close to the source the diffusive field is different compared to the field far away from the source. The third term of f , the crossover term, describes this difference. In the appendix it is shown that

$$f_{td}(r; \omega) + f_{cr}(r; \omega) = - \int_0^\infty \frac{dk}{2\pi} J_1(kr) k^2 \Pi_{sc}(k; \omega), \quad (2.52)$$

where

$$\Pi_{sc}(k; \omega) = \frac{\Pi_0^{-1}(k=0; \omega) \Pi_0(k; \omega)}{\Pi_0^{-1}(k; \omega) - \Pi_0^{-1}(k=0; \omega)}. \quad (2.53)$$

We did not find an analytical expression for the integral in Eq. (2.52) and thus we need to evaluate it numerically. The crossover term vanishes for $r/\ell_f \rightarrow 0$ or $r/\ell_f \gg 1$ and peaks at $r/\ell_f \approx 0.3$. Only around this value of r/ℓ_f , is the gradient (in absolute value) overestimated significantly (up to 25%) when we approximate it by just the sum of coherent and “totally diffusive” terms.

In 3D the Fourier transform (2.46) converges and the intensity is well defined. We rewrite

$$\Pi(r; \omega) = \frac{1}{16\pi^2 r \ell_f} \left(\frac{\ell_f}{r} e^{-r/\ell_f} + 3 + e^{-r/\ell_f} h(r/\ell_f) \right), \quad (2.54)$$

where

$$h(r/\ell_f) = \int_0^\infty d\xi \left(\frac{4(\xi+1)^2}{(2(\xi+1) - \ln(1+2/\xi))^2 + \pi^2} - 1 \right) e^{-\xi r/\ell_f}. \quad (2.55)$$

We were also not able to solve Eq. (2.55) analytically. In the 3D case, the intensity is a function of ℓ_f only (it does not depend on κ_r). Eq. (2.54) consists

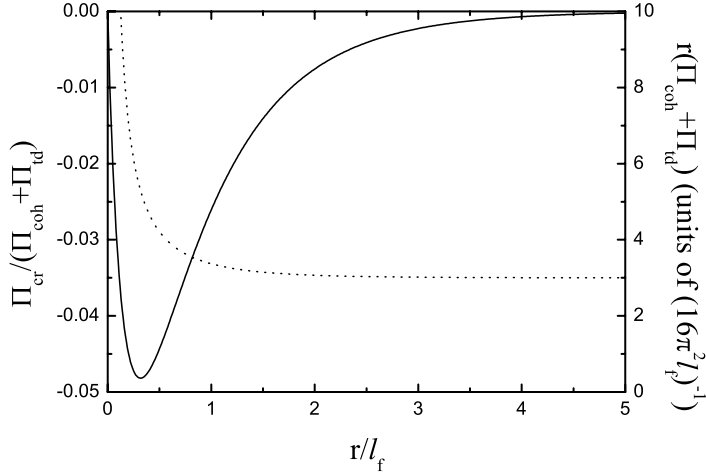


Fig. 2.1: $r(\Pi_{coh} + \Pi_{td})$ in units of $(16\pi^2\ell_f)^{-1}$ (dotted line, right axis) and $\Pi_{cr}/(\Pi_{coh} + \Pi_{td})$ (solid line, left axis) as a function of r/ℓ_f (the source-receiver distance in number of mean free paths) for the 3D disordered medium.

of three terms ($\Pi = \Pi_{coh} + \Pi_{td} + \Pi_{cr}$). The first term is proportional to the coherent intensity, the second term is the algebraically decaying diffuse term (the only term that is not exponentially decaying). We plot the sum of the first and second term multiplied by r (in units of $1/(16\pi^2\ell_f)$) in Fig. 2.1 as a function of r/ℓ_f (on the right axis). The third term is again the crossover correction to the total intensity if we approximate Π by only the first two terms. A plot of the crossover correction divided by the sum of the first two terms is shown in Fig. 2.1 (left axis). The crossover term vanishes for $r/\ell_f \rightarrow 0$ or $r/\ell_f \gg 1$ and peaks at $r/\ell_f \approx 0.3$. It can thus be concluded that the intensity can very well be approximated by just the sum of coherently and totally diffusively propagated intensities, as the total intensity in 3D is never overestimated by more than 5% using this approximation.

To complete this discussion we show the final results for the gradient of the

average intensity in 1D and 2D:

$$\partial_x \langle I_\omega(x) \rangle = -\frac{Q^2 \rho_0^2}{2} \operatorname{sgn}(x) \frac{1}{4\ell_f |\kappa_e|^2}, \quad (2.56)$$

$$\nabla \langle I_\omega(\mathbf{r}) \rangle \approx \hat{\mathbf{r}} \frac{Q^2 \rho_0^2}{2} (f_{coh}(r; \omega) + f_{td}(r; \omega)). \quad (2.57)$$

where f_{coh} and f_{td} are given by Eqs. (2.49) and (2.50), respectively. The average intensity in 3D is approximated well by

$$\langle I_\omega(\mathbf{r}) \rangle \approx \frac{Q^2 \rho_0^2}{2} \frac{1}{16\pi^2 r \ell_f} \left(\frac{\ell_f}{r} e^{-r/\ell_f} + 3 \right). \quad (2.58)$$

We obtain these expressions from our first-principles calculations that enable us to study not only the ballistic and diffusive limits, but also the crossover regime when $r/\ell_f \approx 1$. From this we observe that we can approximate the average intensity well by only the coherent and diffusive contributions. Furthermore, we saw that already at $r/\ell_f \approx 0.3$ the diffusive intensity is higher than the coherent intensity. This does not mean that when a pulsed source is used we should see signs of the crossover to the diffusive regime at this point because the diffuse peak is much broader than the coherent peak so this crossover point is at larger values of r/ℓ_f as was previously reported [9]. Obviously, our present model system has been assumed to be boundless. In a finite slab geometry boundary scattering, which is beyond the scope of this study, would of course affect the results.

2.5.5 Energy density

To derive a first-principles expression for the diffusion constant from Fick's Law (2.11), we still have to calculate the average energy density given by

$$\langle W_\omega(\mathbf{r}) \rangle = \frac{Q^2 \rho_0}{4} \left(\left\langle |\nabla G(\mathbf{r}, \mathbf{r}' = 0; \omega)|^2 \right\rangle + \left\langle \omega^2 c^{-2}(\mathbf{r}) |G(\mathbf{r}, \mathbf{r}' = 0; \omega)|^2 \right\rangle \right). \quad (2.59)$$

The first term is the average potential energy density and the second term corresponds to the kinetic energy.

We start with the potential energy term in 2D and 3D. We define

$$\left\langle |\nabla G(\mathbf{r}, \mathbf{r}' = 0; \omega)|^2 \right\rangle = \Pi''(r; \omega). \quad (2.60)$$

The Fourier transform of $\Pi_0'' (= |\langle \nabla G \rangle|^2)$ diverges, which means that we can not use the same procedure as we used for the intensity and the flux. According to the Bethe-Salpeter equation

$$\Pi''(r; \omega) = \Pi_0''(r; \omega) + \Pi_0^{-1}(k=0; \omega) \int d^d \mathbf{r}_1 \Pi_0''(r_1; \omega) \Pi(|\mathbf{r} - \mathbf{r}_1|; \omega). \quad (2.61)$$

This integral diverges as well because of the strong singularities in Π_0'' (also when the gradient is calculated in the 2D case). When averaging, scatterers are effectively moved around the medium, and for every configuration, the contribution to the total average response is calculated. However, because of the stronger singularities in Π_0'' (as every scatterer becomes a new source of spherical waves) this is not possible when the receiver position coincides with a scatterer position. The reason for this is the point receiver assumption and the far field scattering approximation. We can circumvent this problem by omitting a small volume/area around \mathbf{r}_1 with radius of approximately one wavelength. This slightly modifies the probability distribution function from “completely random” to “non-overlapping” (with the receiver) in order to avoid the divergencies. We then find that Π'' is given by:

$$\Pi''(r; \omega) = |\kappa_e|^2 \Pi(r; \omega). \quad (2.62)$$

In principle, our original expression for Π should now be multiplied by a factor $\exp(-r_o/\ell_f)$, where r_o is the radius of omission so as long as the mean free path is longer then a few wavelengths omitting this small volume does not influence the results. Furthermore, even if scattering is strong and the mean free path is of the order of the wavelength, this factor is not important.

The second term of Eq. (2.59), the kinetic energy, can be split:

$$\left\langle \omega^2 c^{-2}(\mathbf{r}) |G(\mathbf{r}, \mathbf{r}' = 0; \omega)|^2 \right\rangle = \kappa_0^2 \Pi(r; \omega) - \left\langle V(\mathbf{r}; \omega) |G(\mathbf{r}, \mathbf{r}' = 0; \omega)|^2 \right\rangle. \quad (2.63)$$

Now the condition that the scatterer position cannot coincide with the receiver position ensures that the second term vanishes, due to the step function in the potential (2.3). We can thus just disregard this term.

In 1D proving that

$$\Pi''(|x|; \omega) = |\kappa_e|^2 \Pi(|x|; \omega), \quad (2.64)$$

always holds is straightforward. We have to impose the condition the the receiver can not coincide with a scatterer to ensure that

$$\left\langle \omega^2 c^{-2} (x) |G(x, x' = 0; \omega)|^2 \right\rangle = \kappa_0^2 \Pi(|x|; \omega). \quad (2.65)$$

Only under the restrictions mentioned here, can the averaged energy density in 1D, 2D, and 3D be expressed as being proportional to the intensity

$$\langle W_\omega(\mathbf{r}) \rangle = \frac{1}{2\rho_0} \left(|\kappa_e|^2 + \kappa_0^2 \right) \langle I_\omega(\mathbf{r}) \rangle. \quad (2.66)$$

and this thus means that only the gradient of the energy density is well defined in the 1D and 2D cases.

2.6 The diffusion constant

Using the Bethe-Salpeter equation with the Ward identity we find expressions for the average energy flux (2.43-2.45), the (gradient of) the average intensity (2.56-2.58). The average energy density is just proportional to the average intensity (2.66). When $r/\ell_f \gg 1$ we expect (2.11) to hold and, as the gradient of the average energy density and the average flux are now known, we find an expression for the diffusion constant from Eq. (2.11). This means that the diffusion constant can be written as

$$D(\omega) = \frac{1}{d} c_{eff}(\omega) \ell_f(\omega), \quad (2.67)$$

where in the 1D and 3D case

$$c_{eff}(\omega) = c_0 \frac{2\kappa_r |\kappa_0|}{\kappa_r^2 + 1/(2\ell_f)^2 + \kappa_0^2}, \quad (2.68)$$

and in the 2D case

$$c_{eff}(\omega) = c_0 \frac{2\kappa_r |\kappa_0|}{\kappa_r^2 + 1/(2\ell_f)^2 + \kappa_0^2} g(2\kappa_r \ell_f), \quad (2.69)$$

where $g(2\kappa_r \ell_f)$ is given by Eq. (2.51). The effective transport velocity in 2D reduces to Eq. (2.68) in the weak scattering limit.

We can now investigate the frequency dependence of the diffusion constant for a medium with monodisperse scatterers. We relate the scatterer density n

2.6. The diffusion constant

to the average distance between scatterers ($\langle d_s \rangle$) so that $n = \langle d_s \rangle^{-1}$ in 1D, $n = 4\pi^{-1} \langle d_s \rangle^{-2}$ in 2D and $n = 3(4\pi)^{-1} \langle d_s \rangle^{-3}$ in 3D. Let us focus on the diffusion constant of the 2D medium. We write

$$a\kappa_e(a\kappa_0) = \sqrt{(a\kappa_0)^2 - \frac{4}{\pi} \left(\frac{a}{\langle d_s \rangle} \right)^2 t_0(a\kappa_0)}, \quad (2.70)$$

so that the dimensionless property $a\kappa_e$ depends on the dimensionless frequency $\kappa_0 a$ ($= \omega a / c_0$) and two dimensionless model parameters, i.e. the velocity contrast γ ($= c_{int} / c_0$) and the average distance between scatterers in number of scatterer radii ($\langle d_s \rangle / a$). The real and imaginary parts of $a\kappa_e$ are needed to obtain the diffusion constant

$$a\kappa_r(a\kappa_0) = |\text{Re}\{a\kappa_e(a\kappa_0)\}|, \quad (2.71)$$

$$\frac{\ell_f(a\kappa_0)}{a} = \frac{1}{2|\text{Im}\{a\kappa_e(a\kappa_0)\}|}. \quad (2.72)$$

The diffusion constant for a 2D medium is plotted in Fig. 2.2. The relevant frequency range is from $\kappa_0 a (= \omega a / c_0) = 0$ to $\kappa_0 a \approx \pi/2$, as for higher frequencies the isotropic scatterer assumption is no longer valid. For the plot, the density of scatterers was determined by setting $\langle d_s \rangle / a = 10$, increasing this value shifts the curves up. The shape of the curves is predominantly determined by the mean free path. The effective transport velocity c_{eff} only deviates considerably from c_0 when the scatterer velocity and the frequency are small and the scatterer density high. For the diffusion constants shown in the plot, this is only the case when $\gamma = 0.2$. This is also the only case that shows resonances in the relevant frequency range. Further lowering the internal velocity of the scatterers, would “pull in” more resonances in the relevant frequency range. These resonances appear because of resonances in the mean free path. When the scatterer-medium velocity ratio is increased, the mean free path (and thus the diffusion constant) increases until the ratio is larger than unity and then it drops again. However, increasing γ above 10, does not change the diffusion constant much in the frequency range we discuss.

The diffusion constants in 1D and 3D media show the same behavior. Of course, the resonances at low velocity, are caused by the fact that all scatterers are assumed to be of equal size. When solid scatterers in a fluid are considered even more resonances are expected to show up [27]. When scatterer sizes (or velocities) are allowed to vary, the resonances are averaged out.

When the scatterer velocity is zero we obtain an impenetrable model scatterer. This is not a useful model scatterer, as in the low frequency range the

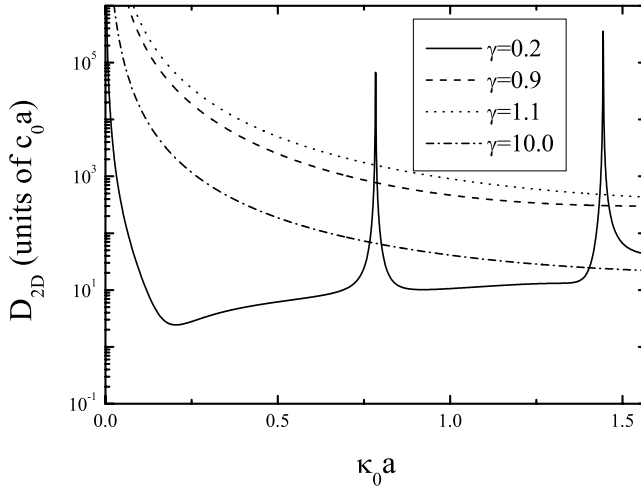


Fig. 2.2: Diffusion constant of the 2D disordered medium in units of $c_0 a$, as a function of the dimensionless frequency $\kappa_0 a$ for four different scatterer-medium velocity ratios (γ). The scatterer density is determined by setting $\langle d_s \rangle / a = 10$.

mean free path (and thus the diffusion constant) differ considerably from the penetrable scatterer case. The reason for this is that the limits for $\omega \rightarrow 0$ and $\gamma \rightarrow 0$ do not commute, as

$$\lim_{\omega \rightarrow 0} \lim_{\gamma \rightarrow 0} \ell_f = \text{const}, \quad (2.73)$$

while

$$\lim_{\gamma \rightarrow 0} \lim_{\omega \rightarrow 0} \ell_f = \infty. \quad (2.74)$$

The effect of this is that at the longer wavelengths, ℓ_f for the impenetrable scatterer is several orders of magnitude smaller than ℓ_f for non zero values of γ .

2.7 Time domain correlations in 3D media

We are not totally restricted to the frequency domain, as the configuration averaged intensity in this domain is related to autocorrelator in the time domain by a Fourier transform. In this section (that is not part of Ref. [22]) we discuss the properties of this correlator in 3D homogeneously disordered media. When the source is a delta function the wave equation reads

$$(\nabla^2 - c^{-2}(\mathbf{r}) \partial_t^2) \psi_\delta(\mathbf{r}; t) = -Q\rho_0 \delta^{(3)}(\mathbf{r}) \delta(t), \quad (2.75)$$

where the subscript δ denotes the impulse response in the time domain. The configuration averaged autocorrelator $\langle \chi_\delta \rangle$ of the wave function ψ_δ is related to the configuration averaged intensity propagator in the frequency domain by

$$\begin{aligned} \langle \chi_\delta(\tau) \rangle &\equiv \int dt \langle \psi_\delta(\mathbf{r}; t + \tau) \psi_\delta(\mathbf{r}; t) \rangle = \int \frac{d\omega}{2\pi} e^{-i\omega\tau} \langle |\psi_\delta(\mathbf{r}; \omega)|^2 \rangle \\ &= \rho_0^2 Q^2 \int \frac{d\omega}{2\pi} e^{-i\omega\tau} \langle |G(\mathbf{r}, \mathbf{r}' = 0; \omega)|^2 \rangle \\ &= \rho_0^2 Q^2 \int \frac{d\omega}{2\pi} e^{-i\omega\tau} \Pi(r; \omega). \end{aligned} \quad (2.76)$$

The analytical approximation for Π in 3D obtained in section 2.5

$$\Pi(r; \omega) \simeq \frac{1}{16\pi^2 r} \left(\frac{1}{r} e^{-r/\ell_f(\omega)} + \frac{3}{\ell_f(\omega)} \right), \quad (2.77)$$

is a sum of the coherent and totally diffuse contributions and all frequency dependence enters in the mean free path defined by Eq. (2.23). If we plot ℓ_f in the relevant frequency range for an average distance of scatterers of $\langle d_s \rangle / a = 10$ (see Fig. 2.3) we see that resonances are present in the relevant frequency range for low wave velocities of the scatterers. As long as the source-receiver distance r is larger than the minima in ℓ_f (here approximately ten times the scattering radius a), then the diffusive contribution of Π dominates the autocorrelation function and this reduces to a transform of the inverse mean free path.

The configuration averaged autocorrelator is not expected to have any interesting properties when the inverse mean free path depends smoothly on frequency. However, when resonances are present, for example for velocity ratios γ between 0 and (approximately) 0.2, this shows up in the autocorrelator. The minima in the mean free path turn out to contribute most to the autocorrelator. When the density of scatterers is low the inverse mean free path is well

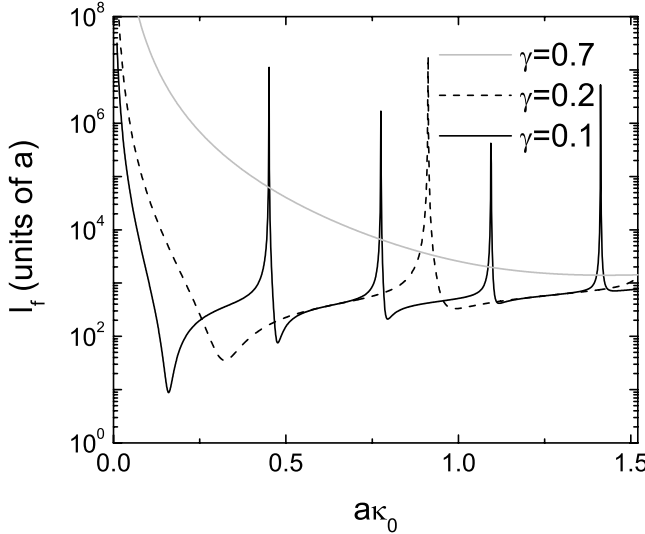


Fig. 2.3: Plot of the mean free path ℓ_f of the 3D homogeneously disordered medium in units of the scatterer radius a as a function of the dimensionless frequency $a\kappa_0$ for three different scatterer-medium velocity ratios γ . The scatterer density was determined by setting $\langle d_s \rangle / a = 10$.

approximated by

$$a\ell_f^{-1} \simeq \frac{3}{4\pi} \frac{a^3}{\langle d_s \rangle^3} \frac{1}{\kappa_0 a} \text{Im} \{t_0(\omega)/a\}. \quad (2.78)$$

In 3D the transition matrix is related to the scattering matrix by

$$t_0(\omega)/a = \frac{2\pi i}{\kappa_0 a} (S_0(\kappa_0 a) - 1), \quad (2.79)$$

and the scattering matrix for the 3D s-wave scatterer from Eq. (2.17) can also be written as a pole expansion [14]

$$S_0(\kappa_0 a) = e^{-i2\kappa_0 a} \prod_{n=0}^{\infty} \frac{(\kappa_0 a + i\beta)^2 - ((2n+1)\Omega_0)^2}{(\kappa_0 a - i\beta)^2 - ((2n+1)\Omega_0)^2}, \quad (2.80)$$

2.8. Conclusions

where $\Omega_0 = \pi\gamma/2$ and $\beta = \gamma \log \left(\left| \left(\gamma - 1 \right) / \left(\gamma + 1 \right) \right| \right) / 2$. The poles are located at the internal resonances of the scatterers, and these are responsible for the minima in the mean free path. These correspond to the maxima in the inverse mean free path and when only these are taken into account the dominant term in the autocorrelator can be approximated by a sum of peaks, so that

$$a\ell_f^{-1} \propto \frac{1}{(\kappa_0 a)^2} \sum_{n=0}^{\infty} \delta(\kappa_0 a - (2n+1)\Omega_0). \quad (2.81)$$

Using this approximation in Eq. (2.76) yields for the configuration averaged autocorrelator

$$\langle \chi_{\delta}(\tau) \rangle \propto \sum_{n=0}^{\infty} \frac{1}{((2n+1)\Omega_0)^2} \cos((2n+1)\Omega_0\tau c_0/a), \quad (2.82)$$

which are triangular oscillations as a function of the correlation time τ with a period that is governed by the velocity ratio γ .

When we calculate the configuration averaged autocorrelator numerically (see Fig. 2.4), we indeed see the triangular oscillations for low scatterer velocities. For the numerical Fourier transform we limit the bandwidth of the pulse (smoothly) to the relevant frequency range, which yields a pulse that is approximately $5a/c_0$ wide. The oscillations are visible on a much longer time scale than the correlator of the unscattered pulse or the correlator of the scattered pulse in a medium with scatterers with a higher wave velocity (see the grey solid line in Fig. 2.4 for example). We have seen here that the configuration averaged intensity in the frequency domain contains information about the autocorrelation function of the amplitude response, which helps in distilling information on the medium from the response.

2.8 Conclusions

We have calculated the transport of energy and intensity in disordered 1D, 2D, and 3D (infinite) media emitted by a monochromatic source. Using the ladder approximation to the Bethe-Salpeter equation we explicitly show that the total intensity is well approximated by the sum of the coherent and the fully developed diffuse wave field for all source-receiver distances. The results for 3D disordered systems agree with findings previously reported, except for the expression for the intensity in the crossover regime, which has not been reported before. We have obtained more new results studying energy and intensity propagation in

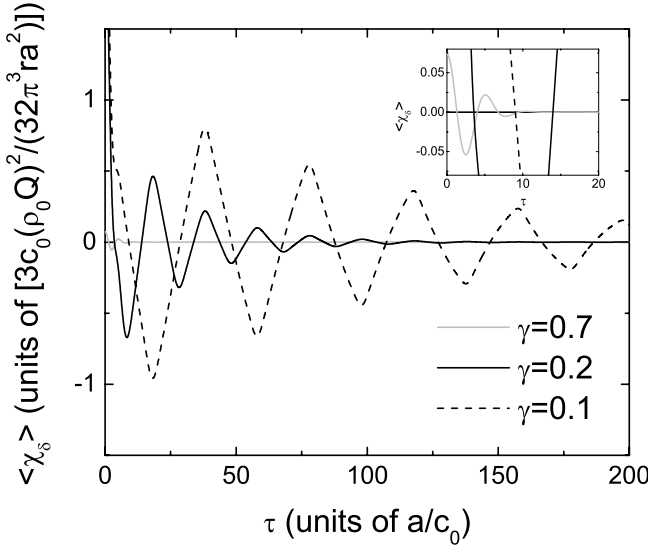


Fig. 2.4: The configuration averaged autocorrelator as a function of the correlation time τ for three different values of the velocity ratio γ . The inset shows an enlargement for $0 < \tau < 20a/c_0$.

2D system in detail. When compared to the 3D case, the 2D disordered system shows interestingly different behavior: In 2D, the average energy flux depends on the mean free path and the effective transport velocity depends differently in terms of the scattering parameters. The (gradient of the) intensity as a function of the source-receiver distance, on the other hand, behaves similarly in the 2D and the 3D case. The monochromatic source enables us to investigate the frequency dependence of the macroscopic diffusion constant where we particularly focused on the influence of the finite size of the scatterers. For a monodisperse distribution of scatterers shape resonances show up in the relevant frequency range for low internal scatterer velocities (γ small). In this frequency range (where scattering is expected to be isotropic) the dependence of the scattering properties on frequency cannot be neglected. This means that descriptions of broadband pulse propagation through these media should in principle incorpo-

rate both frequency dependent and multiple scattering effects. The development of a workable Ward identity in this case remains a challenge, however. Studying the autocorrelator in the time domain also yields interesting results for resonant scatterers, as resonances are responsible for long time-scale triangular oscillations in the autocorrelator. The period of these oscillations is directly related to the velocity ratio γ . Finally, we want point out that our model describes transport of scalar acoustic waves but results can be extended and many conclusions should also apply to vector wave fields random media.

2.9 Appendix: Energy and intensity in 2D

In this appendix we derive the configuration-averaged intensity and energy flux in a disordered 2D medium. Starting point is the 2D Green function propagator

$$G(r; \omega) = \begin{cases} -\frac{i}{4} H_0^{(1)}((\kappa_r + i/(2\ell_f))r) & \text{if } \omega > 0 \\ \frac{i}{4} H_0^{(2)}((\kappa_r - i/(2\ell_f))r) & \text{if } \omega < 0 \end{cases}. \quad (2.83)$$

We use the properties

$$H_0^{(2)}((\kappa_r - i/(2\ell_f))r) = H_0^{(1)}((- \kappa_r + i/(2\ell_f))r), \quad (2.84)$$

and

$$H_0^{(1)}((\pm \kappa_r + i/(2\ell_f))r) = -i \frac{2}{\pi} K_0((\mp i \kappa_r + 1/(2\ell_f))r), \quad (2.85)$$

to express the Hankel functions ($H_0^{(j)}$) in terms of modified Bessel function of the second kind (K_0). The Fourier transform of the coherent intensity

$$\Pi_0(k; \omega) = 2\pi \int_0^\infty dr |G(r; \omega)|^2 J_0(kr), \quad (2.86)$$

is then obtained from Ref. [29] and using properties of the associated Legendre polynomials [30] as

$$\Pi_0(k; \omega) = \frac{\ell_f^2}{\pi} \frac{1}{1 + (2\kappa_r \ell_f)^2} \frac{P_{-1/2}^{-1/2}(u)}{P_{1/2}^{-1/2}(u)}, \quad (2.87)$$

with

$$u = \frac{1 - (2\kappa_r \ell_f)^2}{1 + (2\kappa_r \ell_f)^2} + \frac{2k\ell_f}{1 + (2\kappa_r \ell_f)^2}. \quad (2.88)$$

This is can be rewritten as

$$\Pi_0(k; \omega) = \frac{\ell_f^2}{\pi} \frac{\arcsin\left(\frac{\sqrt{(2\kappa_r\ell_f)^2 - (k\ell_f)^2}}{\sqrt{1 + (k\ell_f)^2}}\right)}{\sqrt{1 + (k\ell_f)^2} \sqrt{(2\kappa_r\ell_f)^2 - (k\ell_f)^2}}. \quad (2.89)$$

$\Pi_0(k; \omega)$ is real, continuous and differentiable for all (real) $k \geq 0$.

The flux in the 2D system is given by

$$\langle \mathbf{n} \cdot \mathbf{F}_\omega(\mathbf{r}) \rangle = \frac{Q^2 \rho_0 \omega}{2} \frac{C}{r} \mathbf{n} \cdot \hat{\mathbf{r}}, \quad (2.90)$$

where C is the constant to be calculated:

$$C = \frac{\int_0^\infty dr \operatorname{Im}\{G(r; \omega) \partial_r G^*(r; \omega)\} r^2}{\Pi_0^{-1}(k=0; \omega) \partial_k^2 \Pi_0(k; \omega)|_{k=0}}. \quad (2.91)$$

The term in the denominator is easily obtained

$$\Pi_0^{-1}(k=0; \omega) \partial_k^2 \Pi_0(k; \omega)|_{k=0} = -\ell_f^2 \left(1 - \frac{1}{(2\kappa_r\ell_f)^2} + \frac{1}{2\kappa_r\ell_f \arctan(2\kappa_r\ell_f)} \right). \quad (2.92)$$

The solution to the integral

$$\begin{aligned} & \int_0^\infty dr \operatorname{Im}\{G(r; \omega) \partial_r G^*(r; \omega)\} r^2 \\ &= -\frac{\operatorname{sgn}(\omega)}{4\pi^2 \ell_f} \int_0^\infty dr r^2 \operatorname{Im}\{(i\kappa_r + 1/(2\ell_f)) K_0((-i\kappa_r + 1/(2\ell_f)) r) \\ & \quad \times K_1((i\kappa_r + 1/(2\ell_f)) r)\} \\ &= -\frac{\operatorname{sgn}(\omega)}{4\pi^2 \ell_f^2} \operatorname{Im} \left\{ 2 \frac{(1 + i2\kappa_r\ell_f)^2}{(1 - i2\kappa_r\ell_f)^4} F \left(2, 2; 3; 1 - \frac{(1 + i2\kappa_r\ell_f)^2}{(1 - i2\kappa_r\ell_f)^2} \right) \right\}, \end{aligned} \quad (2.93)$$

can be found from Ref. [29]. However, the proper solution (on the right Riemann sheet) needs to be chosen in order to simplify the hypergeometric series F . One

can check numerically that

$$\int_0^\infty dr \operatorname{Im} \{G(r; \omega) \partial_r G^*(r; \omega)\} r^2 = -\frac{\operatorname{sgn}(\omega)}{4\pi^2 \ell_f^2} \arctan(2\kappa_r \ell_f) \times \left(1 - \frac{1}{(2\kappa_r \ell_f)^2} + \frac{1}{2\kappa_r \ell_f \arctan(2\kappa_r \ell_f)}\right). \quad (2.94)$$

Hence, C is given by

$$C = \frac{\operatorname{sgn}(\omega)}{4\pi^2} \arctan(2\kappa_r \ell_f). \quad (2.95)$$

The intensity is proportional to the propagator $\Pi(r; \omega)$, expressed in terms of $\Pi_0(k; \omega)$ by the Fourier transform (2.46). As only the gradient of the intensity is a well-defined property, we calculate

$$\nabla \Pi(r; \omega) = -\hat{\mathbf{r}} \int_0^\infty \frac{dk}{2\pi} \frac{k^2 J_1(kr)}{\Pi_0^{-1}(k; \omega) - \Pi_0^{-1}(k=0; \omega)}. \quad (2.96)$$

This contains both the coherent and the scattered intensity. As the coherent intensity is known, we focus on the scattered intensity by calculating

$$\nabla \Pi_{sc}(r; \omega) = -\hat{\mathbf{r}} \int_0^\infty \frac{dk}{2\pi} J_1(kr) k^2 \Pi_{sc}(k; \omega), \quad (2.97)$$

with

$$\Pi_{sc}(k; \omega) = \frac{\Pi_0^{-1}(k=0; \omega) \Pi_0(k; \omega)}{\Pi_0^{-1}(k; \omega) - \Pi_0^{-1}(k=0; \omega)}. \quad (2.98)$$

Eq. (2.97) is the integral to calculate numerically when we need to calculate the gradient of the multiply scattered intensity. $\Pi_{sc}(k; \omega)$ is a monotonically decaying function with a maximum at $k=0$, that vanishes as $k \rightarrow \infty$. As the Bessel function is also decaying with r , we know that for $r/\ell_f \gg 1$

$$\nabla \Pi_{td}(r; \omega) = -\hat{\mathbf{r}} \frac{\Pi_{sc}(k=0; \omega)}{2\pi r}. \quad (2.99)$$

and

$$\nabla \Pi_{td}(r) = -\hat{\mathbf{r}} \frac{\arctan(2\kappa_r \ell_f)}{\pi^2 2\kappa_r \ell_f} \frac{1}{r} g^{-1}(2\kappa_r \ell_f), \quad (2.100)$$

where

$$g(2\kappa_r \ell_f) = 1 - \frac{1}{(2\kappa_r \ell_f)^2} + \frac{1}{2\kappa_r \ell_f \arctan(2\kappa_r \ell_f)}. \quad (2.101)$$

td stands for “totally diffusive”.

References

- [1] Proc. SPIE **1888** (1993), special issue on optical tomography, edited by B. Chance and R.R. Alfano; S.R. Arridge, Inverse Problems **15**, R41, (1999).
- [2] A.K. Fung, *Microwave Scattering and Emission Models and Their Applications* (Artech House, Boston, 1994).
- [3] F.J. Fry, *Ultrasound: Its Applications in Medicine and Biology* (Elsevier, Amsterdam, 1978); A. Migliori and J.L. Sarrao, *Resonant Ultrasound Spectroscopy, Applications to Physics, Materials Measurement and Nondestructive Evaluation* (Wiley, New York, 1997).
- [4] R. Snieder, in *Diffuse Waves in Complex Media*, edited by J.P. Fouque (Kluwer, Dordrecht, 1999).
- [5] E. Larose, A. Derode, M. Campillo, and M. Fink, J. Appl. Phys. **95**, 8393 (2004); A.E. Malcolm, J.A. Scales, and B.A. van Tiggelen, Phys. Rev. E **70**, 015601(R) (2004).
- [6] P. Sheng, *Introduction to Wave Scattering, Localization and Mesoscopic Phenomena* (Academic Press, New York, 1995).
- [7] D.S. Wiersma, P. Bartolini, A. Lagendijk, and R. Righini, Nature (London) **390**, 671 (1997).
- [8] M. Haney, and R. Snieder, Phys. Rev. Lett. **91**, 093902 (2003); S.E. Skipetrov, and B.A. van Tiggelen, *ibid.* **92**, 113901 (2004); S.K. Cheung, X. Zhang, Z.Q. Zhang, A.A. Chabanov, and A.Z. Genack, *ibid.* **92**, 173902 (2004); E. Larose, L. Margerin, B.A. van Tiggelen, and M. Campillo, *ibid.* **93**, 048501 (2004).
- [9] K.M. Yoo, F.Liu, and R.R. Alfano, Phys. Rev. Lett. **64**, 2647 (1990); R.H.J. Kop, P. de Vries, R. Sprik, A. Lagendijk, *ibid.* **79**, 4369 (1997); P.-A. Lemieux, M.U. Vera, and D.J. Durian, Phys. Rev. E **57**, 4498 (1998); Z.Q. Zhang, I.P.

References

Jones, H.P. Schriemer, J.H. Page, D.A. Weitz, and P. Sheng, *ibid.* **60**, 4843 (1999); X. Zhang, and Z.Q. Zhang, *ibid.* **66**, 016612 (2002).

[10] Y. Lai, S.K. Cheung, and Z.Q. Zhang, Phys. Rev. E **72**, 036606 (2005).

[11] M. Fink, Phys. Today **50**, 34 (1997).

[12] P. de Vries, D.V. van Coevorden, and A. Lagendijk, Rev. Mod. Phys. **70**, 447 (1998).

[13] M.C.W. van Rossum, and Th.M. Nieuwenhuizen, Rev. Mod. Phys. **71**, 313 (1999).

[14] G.E.W. Bauer, M.S. Ferreira, and C.P.A. Wapenaar, Phys. Rev. Lett. **87**, 113902 (2001).

[15] H. Sato and M.C. Fehler, *Seismic Wave Propagation and Scattering in the Heterogeneous Earth* (Springer, New York, 1998).

[16] A. Tourin, M. Fink, and A. Derode, Waves Random Media 10, R31 (2000).

[17] A. Lagendijk, and B.A. van Tiggelen, Phys. Rep. **270**, 143 (1996).

[18] R. Hennino, N. Trégourès, N.M. Shapiro, L. Margerin, M. Campillo, B.A. van Tiggelen, and R.L. Weaver, Phys. Rev. Lett. **86**, 3447 (2001); U. Wegler, and B.-G. Lühr, Geophys. J. Int. **145**, 579 (2001).

[19] J. de Rosny, A. Tourin, A. Derode, B. van Tiggelen, and M. Fink, Phys. Rev. E **70**, 046601 (2004).

[20] A. Tourin, A. Derode, P. Roux, B.A. van Tiggelen, and M. Fink, Phys. Rev. Lett. **79**, 3637 (1997); N.P. Trégourès, and B.A. van Tiggelen, Phys. Rev. E **66**, 036601 (2002); G. Samelsohn, and V. Freilikher, *ibid.* **70**, 046612 (2004).

[21] R. Sprik, and A. Tourin, Ultrasonics **42**, 775 (2004).

[22] S. Gerritsen, and G.E.W. Bauer, Phys. Rev. E. **73**, 016618 (2006).

[23] A. Messiah, *Quantum Mechanics* (North-Holland, Amsterdam, 1962). Vol. II.

[24] E. Merzbacher, *Quantum Mechanics* (Wiley, New York, 1961).

References

- [25] P. Exner, and P. Šeba, Phys. Lett. A **222**, 1 (1996).
- [26] N.G. Einspruch, E.J. Witterholt, and R.T. Truell, J. Appl. Phys. **31**, 806 (1960).
- [27] A. Derode, A. Tourin, and M. Fink, Phys. Rev. E **64**, 036605 (2001).
- [28] M.S. Ferreira, and G.E.W. Bauer, Phys. Rev. E **65**, 045604(R) (2002).
- [29] I.S. Gradshteyn, and I.M. Ryzhik, *Table of Integrals, Series and Products* (Academic Press, London, 1965).
- [30] M. Abramowitz, and I.A. Stegun, *Handbook of Mathematical Functions* (Dover Publications, New York, 1964).

3. DIFFUSE WAVE PROPAGATION AND INTERFACES

3.1 *Introduction*

Multiple scattering at small inhomogeneities in disordered (complex) media often limits the applicability of imaging and techniques with classical waves, such as electromagnetic waves in radar applications and optical tomography [1], or acoustic waves in ultrasonical imaging and geophysical exploration [2]. When scattering due to disorder is so weak that a substantial ballistic signal remains, larger objects with sufficient contrast in the constitutive parameters can be imaged by measuring travel times of pulsed sources. When the travel path of the waves exceeds the transport mean free path, wave energy is propagated diffusively, as explained in the introductory chapter, and this complicates imaging and detection considerably [3]. A formalism that relates diffuse wave propagation to the material properties in such systems in a simple physical picture could be useful for quantitative imaging techniques. However, describing systems that contain both many scatterers (that are small on the wavelength scale) and macroscopic objects using the diffusion equation requires careful consideration of the boundary conditions at the interfaces [4].

In this chapter, we focus on the influence of (sharp) interfaces between diffusive media on diffuse wave propagation. In a diffuse system it is possible to define a local energy density on the length scale of the (scattering) mean free path. This local energy density is position dependent and its gradient is related to the energy flux. Across (sharp) interfaces between different media, the energy density drops discontinuously. We develop a microscopic scattering formalism that relates this drop to the energy density on both sides of the interface by introducing an interface resistance. We start from a description of a point contact for classical (scalar) waves between large reservoirs where the net energy current is calculated by summing over propagating modes in a narrow constriction between the reservoirs. In wide and transparent contacts, corrections to the drift in the energy current become important and need to be quantified. The results are not just restricted to diffuse classical waves only, but we also

3.2. Classical wave transmission through point contacts

discuss their implications on the description of heat transport across solid-solid and solid-fluid boundaries. We end this chapter with a discussion on a different type of wave propagation, i.e. spin waves in ferromagnetic metals and insulators. We show that in this case the point contact description of spin wave transport can be extended to interfaces between bulk ferromagnets as well, in order to describe magnetization (spin) currents carried by spin waves through interfaces between ferromagnets.

3.2 Classical wave transmission through point contacts

An important formalisms to describe charge transport in mesoscopic systems such as narrow constrictions called quantum point contacts was developed by Landauer and Büttiker [5]. It has been successful in describing conduction quantization in electronic point contacts. Furthermore, the formalism is not restricted to electronic transport but has been employed to describe photon [6], phonon [7] and even magnon [8] propagation. Predictions of quantized heat conduction by phonons and photons have later been confirmed [9, 10].

We consider the propagation of phonon modes in the configuration schematically drawn in Fig. 3.1, where two large reservoirs are connected through leads and a narrow constriction (compared to the size of the reservoirs and the phonon wavelengths). The reservoirs are equipartitioned phonon baths (black bodies), and the net energy current from the left to the right reservoir flowing through the leads is given by [7]

$$J = \frac{1}{2\pi} \int d\omega \hbar\omega \left(n_L(\omega) \sum_{\alpha} T_{\alpha} - n_R(\omega) \sum_{\beta} T_{\beta} \right). \quad (3.1)$$

Here n_i is the energy distribution function and the index $i = L(R)$ stands for the left(right) lead. For a bath at a certain temperature Θ_i , n_i is the Planck distribution function

$$n_i(\omega) = \frac{1}{\exp\left(\frac{\hbar\omega}{k_B\Theta_i}\right) - 1}, \quad (3.2)$$

where k_B is the Boltzmann constant. When the reservoirs are externally pumped at a certain frequency ω_0 $n_{i0}\delta(\omega - \omega_0)$ has to be added to the thermal distribution, where n_{i0} has units of frequency. The summation in Eq. (3.1) runs over right(left) going quasi one-dimensional propagating modes in the real or fictitious leads indexed by $\alpha(\beta)$ and $T_{\alpha(\beta)}$ is the probability that a mode is

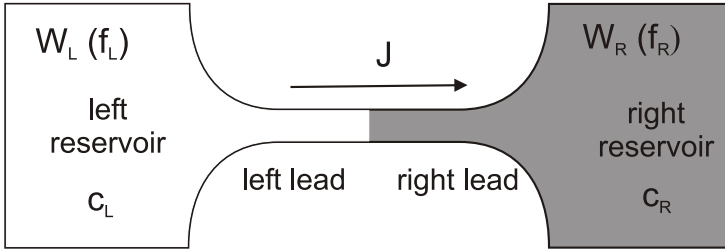


Fig. 3.1: Schematic representation of the reservoir-lead-interface-lead-reservoir configuration.

transmitted from left(right) to right(left). At thermal equilibrium with equal temperatures ($n_L = n_R$) in the left and right reservoir the net energy current vanishes, so that

$$\sum_{\alpha} T_{\alpha} = \sum_{\beta} T_{\beta}. \quad (3.3)$$

When the coupling of the lead modes is considered to be adiabatic (all lead modes are totally transmitted from the reservoirs into the leads) and in the absence of an interface or scattering region (equal lead and reservoir properties left and right) $T_{\alpha} = 1$ and the summation can just be replaced by the number of lead modes. The adiabatic regime is relevant for various quantized conduction problems.

As mentioned before, the Landauer-Büttiker formalism is usually applied to systems in which the number of propagating modes is small (narrow constriction compared to the wavelength) [11]. Furthermore, the expression for the energy current contains \hbar which suggests that this is in principle a quantum mechanical problem. In this section we show that we can make a connection between the classical macroscopic energy transport and the quantum description and that, in principle, in the classical case an expression for the energy current can be derived without introducing \hbar .

Let us take a closer look at the configuration in Fig. 3.1. We start with the energy density in the three-dimensional (3D) reservoirs of size $L_x \times L_y \times L_z$. For simplicity we disregard the polarization degree of freedom of the vibrational modes, so the medium under consideration is equivalent to a liquid. In a homogeneous liquid the acoustic modes are plane waves with frequency ω_{κ} and

3.2. Classical wave transmission through point contacts

wavevector κ described by

$$\psi_{\kappa}(\mathbf{r}; t) = A_{\kappa} \cos(\kappa \cdot \mathbf{r} - \omega_{\kappa} t), \quad (3.4)$$

where the amplitude A_{κ} depends on the amount of energy carried by the mode. The unit of A_{κ} is chosen to be Jsm^{-3} , as ψ is related to pressure by $p = \partial_t \psi$ and to local particle velocity by $\mathbf{v} = -\rho_0^{-1} \nabla \psi$, with ρ_0 the constant mass density. In the continuum limit the dispersion $\omega_{\kappa} = \omega_{\kappa} = c_i \kappa$ and in chapter two we obtained that the time-averaged energy density of the mode is

$$\bar{W}_{\kappa} = \frac{A_{\kappa}^2}{4\rho_0} \left(\kappa^2 + \frac{\omega^2}{c_i^2} \right), \quad (3.5)$$

where c_i is the wave velocity and the index $i = L(R)$ stands for the left(right) reservoir. In this chapter we concentrate on time-averaged properties and steady state situations, so for the time being we drop the bar that denotes time-averaging.

The total energy density in reservoir i from the contributions of all modes is

$$W_i = \sum_{\kappa} W_{\kappa}. \quad (3.6)$$

When the energy is equipartitioned over degenerate modes, the amplitude does not depend on the direction of κ . We assume that the volume of the bodies is so large that the energy exchange does not significantly disturb their equilibrium, so that they can be considered as baths (black-body radiators). For the moment we do not specify the energy distribution function A_{κ}^2 . Inserting the dispersion $\omega = c_i \kappa$ we can rewrite Eq. (3.6)

$$W_i = \sum_{\kappa} \frac{A_{\kappa}^2}{2\rho_0} \int d\omega \kappa^2 \delta(\omega - c_i \kappa), \quad (3.7)$$

where δ is the Dirac delta function. In the continuum limit

$$\sum_{\kappa} \rightarrow \frac{V}{(2\pi)^3} 4\pi \int d\kappa \kappa^2, \quad (3.8)$$

where V is the volume of the bath. This gives

$$W_i = \frac{1}{2\pi^2} \int d\omega \frac{\omega^4}{c_i^5} \frac{VA_{\omega/c_i}^2}{2\rho_0}. \quad (3.9)$$

3. Diffuse wave propagation and interfaces

The energy density is an intensive property which means that $A_{\omega/c_i}^2 \propto 1/V$.

When $c_L = c_R = c$ the energy current from left to right ($J_{L \rightarrow R}$) is obtained by summing over all modes propagating in the positive z -direction in the left reservoir that propagate into the lead

$$J_{L \rightarrow R} = \sum_{\kappa}^{\kappa_z > 0} J_{\kappa} = \sum_{\kappa}^{\kappa_z > 0} S_{Bath} \mathbf{F}_{\kappa} \cdot \mathbf{z}. \quad (3.10)$$

Here \mathbf{F}_{κ} is the time averaged energy flux of a mode with wave vector κ

$$\mathbf{F}_{\kappa} = \frac{A_{\kappa}^2}{2\rho_0} \omega_{\kappa} \kappa, \quad (3.11)$$

and $S_{Bath} = L_x \times L_y$, the cross section of the reservoir perpendicular to the transport direction. Again, we assume equipartition of energy over the modes and we substitute the continuum dispersion relation to obtain

$$J_{L \rightarrow R} = \frac{1}{L_z} \int d\omega \sum_{\kappa}^{\kappa_z > 0} \frac{V A_{\kappa}^2}{2\rho_0} \kappa_z c \kappa \delta(\omega - c\kappa). \quad (3.12)$$

Let us assume that many lead modes are available, which is the same when the wavelengths are much smaller than the width of the constriction. In this regime the wave vector component parallel to the plane perpendicular to the propagation direction is the proper ‘‘quantum number’’, i.e. the mode index $\alpha = \kappa_{\parallel}$. The integral over κ_z , with $\hat{\mathbf{z}}$ the transport direction, gives

$$J_{L \rightarrow R} = \frac{1}{2\pi} \int d\omega \frac{V A_{\omega/c}^2}{2\rho_0} \frac{\omega^2}{c^2} \sum_{\kappa_{\parallel}}^{\kappa_{\parallel} \leq \omega/c}. \quad (3.13)$$

The summation is just the number of propagating modes $N(\omega)$ in the constriction. Denoting the amplitudes in the right reservoir with B_{κ} , the net energy flow from left to right becomes

$$J = J_{L \rightarrow R} - J_{R \rightarrow L} = \frac{1}{2\pi} \int d\omega \frac{V}{2\rho_0} \left(A_{\omega/c}^2 - B_{\omega/c}^2 \right) \frac{\omega^2}{c^2} N(\omega). \quad (3.14)$$

Eq. (3.14) relates the energy current to the properties of the reservoirs and the leads. The energy density in the reservoir

$$W_i = \frac{1}{2\pi^2} \int d\omega \hbar \frac{\omega^3}{c_i^3} n_i(\omega). \quad (3.15)$$

3.2. Classical wave transmission through point contacts

enables us to relate the intensities of the modes with a certain frequency to the distribution function

$$\frac{VA_{\omega/c_i}^2}{2\rho_0} = \hbar \frac{c_i^2}{\omega} n_i(\omega). \quad (3.16)$$

We are now in a position to compare our classical description with the Landauer-Büttiker formalism. In the case of a simple wide constriction, the number of modes depends only on the area, not on the geometrical details of the constriction and $N(\omega) = S_C \omega^2 / (4\pi c^2)$. We can then relate the energy current to the difference in energy density in the baths as

$$J = \frac{1}{2\pi} \int d\omega \hbar \omega \frac{S_C \omega^2}{4\pi c^2} (n_L(\omega) - n_R(\omega)) = \frac{S_C c}{4} (W_L - W_R). \quad (3.17)$$

The analogy with charge currents driven by a voltage difference is clear. $4/(S_C c)$ is the geometric resistance of the constriction which is a result of the finite number of modes. In electronic transport this is the Sharvin resistance [12].

When $c_L \neq c_R$ there is a scattering interface at the position of the constriction. We have to take into account the probability that a right-going mode from the left reservoir is transmitted into the right lead and vice versa. The total energy current then becomes

$$J = \frac{1}{2\pi} \int d\omega \hbar \omega [n_L(\omega) - n_R(\omega)] \sum_{\kappa_{\parallel}}^{\kappa_{\parallel} \leq \omega/c_i} T_{ij}(\kappa_{\parallel}). \quad (3.18)$$

The coefficients T_{ij} are now energy transmission coefficients from side i to side j . Transmission depends only on the modulus of κ_{\parallel} and for a Sharvin point contact we can further simplify

$$\sum_{\kappa_{\parallel}}^{\kappa_{\parallel} \leq \omega/c_i} T_{ij}(\kappa_{\parallel}) \rightarrow \frac{S_C}{2\pi} \int_0^{\omega/c_i} d\kappa_{\parallel} \kappa_{\parallel} T_{ij}(\kappa_{\parallel}) = \frac{S_C \omega^2}{4\pi c_i^2} 2 \int_0^1 d\xi \xi T_{ij}(\xi), \quad (3.19)$$

so that

$$\sum_{\kappa_{\parallel}}^{\kappa_{\parallel} \leq \omega/c_i} T_{ij}(\kappa_{\parallel}) = N_i(\omega) \bar{T}_{ij}. \quad (3.20)$$

which defines the average transmission coefficient \bar{T}_{ij} .

3. Diffuse wave propagation and interfaces

With Eq. (3.20) the energy current is related to the energy density difference

$$J = \frac{S_C \bar{T}_{LR}}{4c_L^2} (c_L^3 W_L - c_R^3 W_R). \quad (3.21)$$

Drawing again the analogy with charge currents driven by a voltage difference we observe that the equivalent of the potential is not the energy density, but the property $c_i^3 W_i$. Since it is the difference in the energy distribution functions which drives the current, and in this case this is not equivalent to the difference in energy density between the reservoirs. Or in other words, a heat flux between two different materials is driven by a temperature difference and not by a difference in energy density. The resistance $R_{LR} = 4c_L^2 / (S_C \bar{T}_{LR})$ is now a result from both interfacial scattering and the constriction. When $\bar{T}_{LR} \rightarrow 1$ (which in our discussion comes down to $c_L \rightarrow c_R$) we recover the geometrical Sharvin resistance.

3.3 Energy transmission coefficients for wide contacts

3.3.1 The specular interface

We consider a constriction with a perfectly flat and sharp interface, i.e. a step function discontinuity in the wave velocity c_L to c_R . Interface scattering is then described by plane wave transmission and reflection at an infinite interface. The amplitude transmission (t_{LR}) and reflection (r_{LR}) coefficients for the wave amplitudes are calculated using the boundary conditions of continuity of pressure, $p = \partial_t \psi$, and continuity of the horizontal component of the particle velocity, $v_z = -\rho_0^{-1} \partial_z \psi$, across the interface. They depend on the angle of incidence, or κ_{\parallel} [13]:

$$r_{LR} = \frac{\sqrt{\frac{\omega^2}{c_L^2} - \kappa_{\parallel}^2} - \sqrt{\frac{\omega^2}{c_R^2} - \kappa_{\parallel}^2}}{\sqrt{\frac{\omega^2}{c_L^2} - \kappa_{\parallel}^2} + \sqrt{\frac{\omega^2}{c_R^2} - \kappa_{\parallel}^2}}, \quad (3.22)$$

$$t_{LR} = \frac{2\sqrt{\frac{\omega^2}{c_L^2} - \kappa_{\parallel}^2}}{\sqrt{\frac{\omega^2}{c_L^2} - \kappa_{\parallel}^2} + \sqrt{\frac{\omega^2}{c_R^2} - \kappa_{\parallel}^2}}. \quad (3.23)$$

$\kappa_{\parallel} < \omega/c_L$, so these coefficients are always real as long as $c_L > c_R$. When $c_L < c_R$ the coefficients can become complex. Propagating plane waves on the left are then connected with evanescent ones for angles of incidence higher than the critical angle and totally reflected. For the calculation of energy currents

3.3. Energy transmission coefficients for wide contacts

however, we need to know the energy transmission coefficient. For $c_L > c_R$ this is

$$T_{LR}(\kappa_{\parallel}) = t_{12}^2 \frac{\sqrt{\frac{\omega^2}{c_R^2} - \kappa_{\parallel}^2}}{\sqrt{\frac{\omega^2}{c_L^2} - \kappa_{\parallel}^2}} = \frac{4\sqrt{\frac{\omega^2}{c_L^2} - \kappa_{\parallel}^2}\sqrt{\frac{\omega^2}{c_R^2} - \kappa_{\parallel}^2}}{\left(\sqrt{\frac{\omega^2}{c_L^2} - \kappa_{\parallel}^2} + \sqrt{\frac{\omega^2}{c_R^2} - \kappa_{\parallel}^2}\right)^2}. \quad (3.24)$$

When $c_L < c_R$ all energy is reflected for $\kappa_{\parallel} > \omega/c_R$ and the energy transmission coefficient is given by

$$T_{LR}(\kappa_{\parallel}) = \begin{cases} \frac{4\sqrt{\frac{\omega^2}{c_L^2} - \kappa_{\parallel}^2}\sqrt{\frac{\omega^2}{c_R^2} - \kappa_{\parallel}^2}}{\left(\sqrt{\frac{\omega^2}{c_L^2} - \kappa_{\parallel}^2} + \sqrt{\frac{\omega^2}{c_R^2} - \kappa_{\parallel}^2}\right)^2} & \text{for } \kappa_{\parallel} \leq \frac{\omega}{c_R}; \\ 0 & \text{for } \kappa_{\parallel} > \frac{\omega}{c_R}. \end{cases} \quad (3.25)$$

The integrated transmission coefficient \bar{T}_{LR} of the wide point contact is defined by

$$\bar{T}_{LR} = 2 \int_0^1 d\xi \xi T_{LR}(\xi), \quad (3.26)$$

where $T_{LR}(\xi) = T_{LR}(\kappa_{\parallel} = \xi\omega/c_L)$. We find

$$\bar{T}_{LR} = \begin{cases} \gamma \frac{4(2+\gamma)}{3(1+\gamma)^2} & \text{for } \gamma < 1 \\ \frac{1}{\gamma^2} \frac{4(1+2\gamma)}{3(1+\gamma)^2} & \text{for } \gamma > 1 \end{cases}. \quad (3.27)$$

In Fig. 3.2 \bar{T}_{LR} for the specular interface is plotted as a function of the velocity contrast γ (black line).

3.3.2 The ideally diffuse interface

When an interface is not flat and sharp, for example, due to additional interface roughness, interface scattering in general becomes complicated and the transmission coefficients are difficult to calculate. On the other hand, for very rough interfaces, incoming modes are scattered equally into all the outgoing ones and all information about the history of the original incoming mode is lost. For such an ideally diffuse interface an energy transmission coefficient can be calculated analytically again [14].

Let us label the modes not with the parallel wave vector, but with an index i for incoming modes and j for outgoing modes (either left or right from the interface). The transmission coefficient T_{LR}^{ij} then determines the energy that is

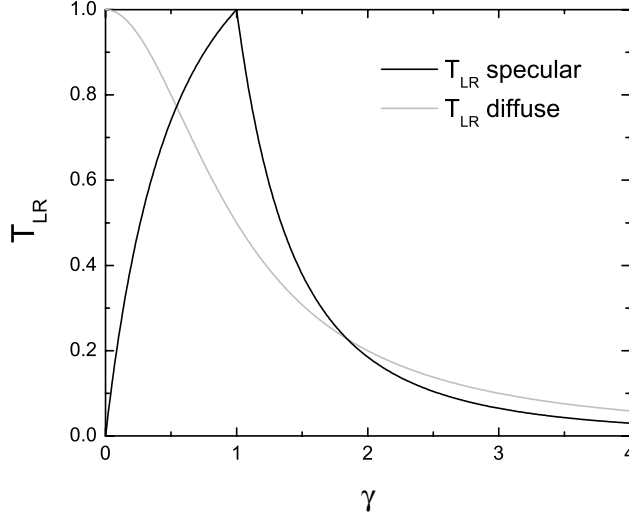


Fig. 3.2: The integrated transmission coefficient \bar{T}_{LR} as a function of the velocity contrast $\gamma = c_R/c_L$ for the specular (black line) and the diffuse (grey line) interface.

transmitted from a right going, incoming mode indexed by i into an outgoing mode with index j . The reflection coefficient R_{RR}^{ij} determines the energy that is reflected back into the right reservoir. Defined in this way, the T_{LR} of the previous section is related to T_{LR}^{ij} by

$$T_{LR} = \sum_{j=1}^{N_R} T_{LR}^{ij} = T_{LR}^i, \quad (3.28)$$

and energy conservation gives

$$\sum_{j=1}^{N_R} T_{LR}^{ij} + \sum_{j=1}^{N_L} R_{LL}^{ij} = T_{LR}^i + R_{LL}^i = 1, \quad (3.29)$$

3.3. Energy transmission coefficients for wide contacts

$$\sum_{j=1}^{N_L} T_{RL}^{ij} + \sum_{j=1}^{N_R} R_{RR}^{ij} = T_{RL}^i + R_{RR}^i = 1. \quad (3.30)$$

When an interface is totally diffuse, the transmission coefficients should not depend on the direction of the incoming modes at all, so therefore

$$\sum_{i=1}^{N_L} T_{LR}^i = N_L \bar{T}_{LR}, \quad (3.31)$$

and $\bar{T}_{LR} = T_{LR}^i$. So for the diffuse interface the condition of zero current at equal temperatures leads to

$$N_L \bar{T}_{LR} = N_R \bar{T}_{RL}. \quad (3.32)$$

Every incoming mode (either from the left or the right) that is scattered contributes the same amount of energy to the outgoing mode j . So for an outgoing right-mover, the condition of equipartitioned modes gives $T_{LR}^{ij} = R_{RR}^{ij}$ so that together with energy conservation one obtains

$$T_{LR}^i = 1 - T_{RL}^i. \quad (3.33)$$

Combining Eqs. (3.32) and (3.33) then gives

$$\bar{T}_{LR} = \frac{N_R}{N_L + N_R}. \quad (3.34)$$

As was mentioned before, for a wide lead we can write $N_i(\omega) = S_C \omega^2 / (4\pi c_i^2)$, so that

$$\bar{T}_{LR} = \frac{1}{c_R^2/c_L^2 + 1} = \frac{1}{\gamma^2 + 1}. \quad (3.35)$$

In Fig. 3.2 \bar{T}_{LR} for the diffuse interface is plotted as a function of the velocity contrast γ (grey line). Note that this expression is by construction not valid for small velocity contrasts ($\gamma \approx 1$), since the diffuse scattering can not be caused by other sources than the disorder in the sound velocities. Also, the fact that $T_{LR} = 1$ for $\gamma = 0$ is an artifact of this simple model. The most important difference with the specular interface is that diffusive scattering increases the transmission for large velocity contrasts.

3.4 Interfaces between diffusive media

Let us now turn to propagation through interfaces between diffusive media. In this case we are again able to describe wave energy propagation in much the same way as electronic transport [15, 16]. When two 3D diffusive slabs are in contact and a current (emitted by a planar source) runs from left to right, a gradient in diffuse energy density builds up, as is schematically depicted in Fig. 3.3. The distribution functions inside the slabs now only differ from the distribution in the reservoirs from the previous sections by a finite drift in the direction of the energy current. A simple approximation consists of separating the distribution function into isotropic right- and left going contributions. In this way we can regard the diffusive slabs as reservoirs and calculate the current through the interface that is driven by the jump in the distribution function of the right going states on the left hand side of the interface and the left going states on the right hand side of the interface. This requires that modes originating from one side of the interface “thermalize” into the equilibrium distribution on the other side [17], but this condition is fulfilled automatically at a distance approximately one transport mean free path from the interface itself [16]. The Ohmic relation we derive from these principles simply reads

$$J = \frac{1}{R_{Int}} (\phi_L - \phi_R), \quad (3.36)$$

where the potential is defined by $\phi_i = c_i^3 W_i$ (see Eq. (3.21)).

When the interface is transparent ($c_L \rightarrow c_R$ in the specular case), the resistance should vanish (there is no Sharvin resistance). It has been shown by Schep et al. [15, 16], and rediscovered by Chen [17] that we can take this into account by subtracting the average of the Sharvin resistances from R_{LR} to obtain the resistance of the interface between the two layers:

$$R_{Int} = R_{LR} - R_{Sh} = \frac{4}{S} c_L^2 \left[\bar{T}_{LR}^{-1} - \frac{1}{2} (1 + \gamma^2) \right], \quad (3.37)$$

where S is the surface area of the interface. The integrated transmission coefficient still has to be calculated from the microscopic scattering matrix of the interface and we showed how to do this for two particular types of interfaces in the previous section. Fig. 3.4 shows the interface resistances for a specular (black solid line) and a diffuse (grey solid line) interface as a function of the velocity contrast γ (left axis). The specular interface resistance vanishes around $\gamma = 1$ and increases rapidly for increasing velocity contrast as (plane

3.4. Interfaces between diffusive media

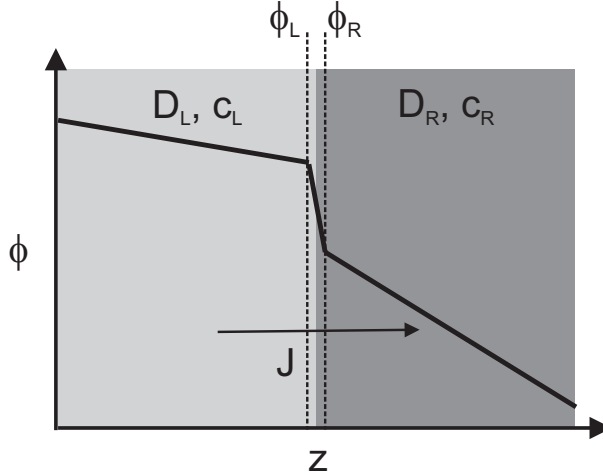


Fig. 3.3: Schematic plot of the diffuse intensity inside two connected diffusing slabs. The energy current across the interface is driven by the difference in potential $\phi_i = c_i^3 W_i$.

wave) transmission and reflection coefficients at a clean interface drop rapidly for increasing γ and modes from the side with the lower wave velocity are totally reflected for larger angles of incidence. For the ideally diffusive interface the resistance does not vanish at $\gamma = 1$. This is an artifact of the model. An ideally diffusive interface implies that $\bar{T}_{LR} = 1/2$ when $\gamma = 1$; the interface scattering condition does not vanish with $\gamma \rightarrow 1$ and this makes this model interface unsuitable for low velocity contrasts. Furthermore, it is clear that the different interface models yield very different results for large velocity contrasts ($\gamma \ll 1$ or $\gamma \gg 1$). The reason that the diffuse interface gives a much lower resistance in this regime, is due to the impossibility of total reflection of modes in this case. Also plotted in Fig. 3.4 is the difference between the interface resistances R_{LR} of the “point” contact discussion (dashed lines) and the interface resistance with the correction R_{Int} . It is clear that when the corrections for the Sharvin resistance are neglected the interface resistance is overestimated. Specifically, the interface resistance of the specular interface does not vanish for vanishing velocity contrast. In the diffuse case the resistance is always exactly 100% overestimated, independent of the velocity contrast. This has important

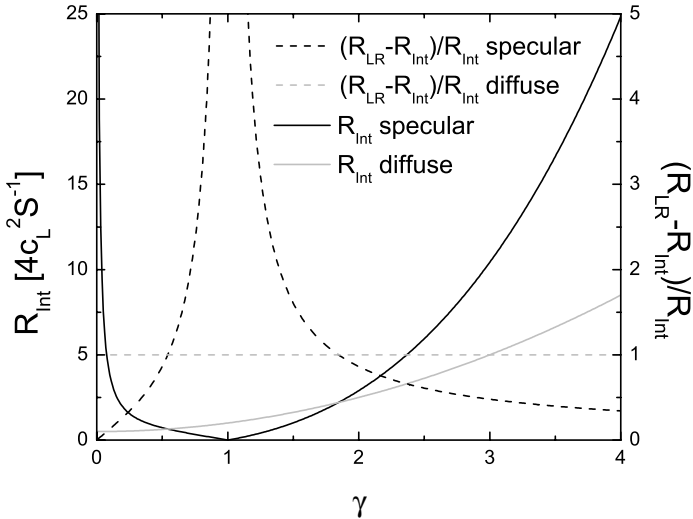


Fig. 3.4: Plot of the interface resistance R_{Int} between two diffusing slabs for a specular (black solid line) and a diffuse (grey solid line) interface as a function of the velocity contrast γ (left axis). Difference between the resistances without the correction for the Sharvin resistance R_{LR} are plotted with dashed lines (right axis).

consequences for the thermal boundary resistance that is discussed in the next section.

It is now straightforward to introduce a series resistor model for the energy current through multilayers of diffusing slabs. Let us assume a planar source in a 3D layered structure. The current between any two planes indexed by L and R in the multilayer structure is related to the driving potential $\phi_L - \phi_R$ by a total resistance R_{Tot} . This resistance is just the sum of bulk and interface resistances of the layers between L and R , where R_{Int} is given by Eq. (3.37). Within the bulk layers, energy density and current are related through Fick's law $J/S = -D_i \partial_z W$ (see chapter 2) and the resistance of a bulk layer is thus $L_i c_i^3 / (S D_i)$, where L_i is the layer thickness (much larger than the transport mean free path) and D_i the diffusion constant. In the next chapter we discuss

3.5. The thermal boundary resistance

how this picture can be extended to arbitrary geometries.

3.5 *The thermal boundary resistance*

In this section we discuss how the interface resistance defined by Eq. (3.37) can be used for the thermal boundary resistance of solid-solid and solid-fluid interfaces. When a temperature gradient is applied across such a boundary the heat flow \dot{Q} by phonons depends on the properties of the interface and the thermal boundary resistance is defined by

$$R_{Bd} = \dot{Q}/(S\Delta\Theta), \quad (3.38)$$

where S is the surface area and $\Delta\Theta = \Theta_L - \Theta_R$ the temperature difference between the left and right side of the interface. The thermal boundary resistance is an important concept in the field of cryogenics, as it influences the cooling capacity of cryostats. The solid-fluid boundary resistance between liquid helium and metals is also known as the Kapitza resistance [14].

The heat flow in Eq. (3.38) is the same as the energy current in the previous section. Several models are used to calculate R_{Bd} , and the most widely used method calculates the net energy flux by summing over the transmission of an isotropic distribution of phonon modes left and right of the interface [14]. This method is equivalent to the one we used in section 3.2 to obtain the resistance R_{LR} , although for phonons in solids two extra transverse modes of polarization need to be taken into account. It results in an expression for the temperature dependent R_{Bd} , where either the acoustic mismatch model (the specular interface) or the diffuse mismatch model (diffuse interface) is used to describe the transmission of the phonon modes. However, calculated in this way, the interface resistance does not vanish for a vanishing interface, it yields a non-physical, finite resistance for an interface between two equal materials.

The problem of the non-zero thermal boundary resistance for vanishing interfaces is a point that is recognized and explained to some extent in the literature. However, improvements of the type of corrections like in Eq. (3.37) are not used in this field [17]. From our discussion in the previous section it seems straightforward that applying the same corrections to the thermal boundary resistance between two bulk materials is a better way to model interface effects on the heat flow across interfaces.

3.6 Spin wave propagation through interfaces

We end this chapter on diffuse waves and interfaces with a totally different type of wave propagation, namely spin waves in ferromagnets. We discuss a result by Meier and Loss [8], who describe the magnetization current between two ferromagnetic insulators through a spin chain point contact. Then we argue that just as for electrons, phonons and classical waves, we can generalize the spin conductance derived by Ref. [8] to arbitrary point contacts and interfaces between bulk ferromagnets and in principle calculate magnetization (spin) currents from spin wave transport in these systems.

For concreteness consider a system with isotropic ferromagnetic exchange interaction in a magnetic field $\mathbf{B}(\mathbf{x}_i) = B_i \mathbf{e}_z$, where spins occupy sites \mathbf{x}_i of a simple lattice with lattice constant a . The Heisenberg spin Hamiltonian is then given by

$$\hat{H} = J \sum_{\langle ij \rangle} \hat{\mathbf{S}}_i \cdot \hat{\mathbf{S}}_j + g\mu_B \sum_i B_i \hat{\mathbf{S}}_{i,z}, \quad (3.39)$$

with $J < 0$ (the exchange integral), μ_B the Bohr magneton, g the g-factor and the summation runs over nearest neighbour sites. The low energy excitations of the ferromagnetic ground state (excited at low temperatures) are long-wavelength spin waves, that may be treated in a continuum model. The motion of the spins is then described by the Landau-Lifschitz equation [19]

$$\partial_t \mathbf{S} = F \mathbf{S} \times \nabla^2 \mathbf{S} + \frac{g\mu_B}{\hbar} \mathbf{S} \times \mathbf{B}, \quad (3.40)$$

where $F = Ja^2/\hbar$ is the spin wave stiffness. For a weakly excited one-dimensional spin chain, with $S^x, S^y \ll S^z \approx S$, the solutions are running spin waves

$$S^x(x; t) \propto \cos(\pm kx - \omega_k t), \quad (3.41)$$

$$S^y(x; t) \propto \sin(\pm kx - \omega_k t), \quad (3.42)$$

with dispersion

$$\varepsilon_k = \hbar\omega_k = g\mu_B B + 2JS(1 - \cos(ka)) \simeq g\mu_B B + \hbar FS k^2, \quad (3.43)$$

for $ka \ll 1$ (so a quadratic dispersion, like in the electron case). Spin waves carry angular momentum, just as pressure waves carry linear momentum. Spin wave excitations are quantized by magnons, and one magnon lowers the total spin of a ferromagnet with saturation magnetization NS by exactly 1. It carries a magnetic moment $-g\mu_B \mathbf{e}_z$ [20]. In a large 3D ferromagnetic reservoir at

temperature Θ magnon states are occupied according to the Planck distribution function. The non-interacting magnon picture holds as long as $\Theta \ll g\mu_B B/k_B$.

When two large reservoirs at temperatures Θ_L (left) and Θ_R (right) and with applied magnetic fields B_L and B_R are connected through a one-dimensional spin chain that is adiabatically coupled to the reservoirs, excited magnons propagate through the chain between the reservoirs analogously to the phonons in a point contact that we discussed earlier. We consider the case $\Theta_L = \Theta_B = \Theta$, the magnetic field gradient is such that $B_L = B - \Delta B/2$, $B_R = B + \Delta B/2$ with $\Delta B \ll B$, and other properties of the reservoirs (like the exchange integral and the spin wave stiffness) are equal. As the energies in the left(right) reservoir are shifted down(up) by $g\mu_B \Delta B/2$, the net magnetization current can be calculated by

$$\begin{aligned}
 I_m &= I_{m,L \rightarrow R} - I_{m,R \rightarrow L} \\
 &= \frac{-g\mu_B}{2\pi\hbar} \left(\int_{g\mu_B \Delta B/2}^{\infty} d\varepsilon n(\varepsilon + g\mu_B B + g\mu_B \Delta B/2) \right. \\
 &\quad \left. - \int_{g\mu_B \Delta B/2}^{\infty} d\varepsilon n(\varepsilon + g\mu_B B - g\mu_B \Delta B/2) \right) \\
 &= \frac{g\mu_B}{2\pi\hbar} \int_0^{g\mu_B \Delta B} d\varepsilon n(\varepsilon + g\mu_B B). \tag{3.44}
 \end{aligned}$$

When $B \gg \Delta B$ the magnetization current can be approximated as

$$I_m \simeq \frac{(g\mu_B)^2}{2\pi\hbar} n(g\mu_B B) \Delta B \equiv \frac{1}{R_m} \Delta B. \tag{3.45}$$

So, because there is a net magnon current from the right to the left, the magnetization current runs from the left to the right reservoir and it is proportional to the inverse of the “magnetization resistance” $R_m \equiv 2\pi\hbar \left[(g\mu_B)^2 n(g\mu_B B) \right]^{-1}$.

Completely analogous to the discussion for electrons, phonons and classical waves in point contacts, this description of the magnon point contact can be extended towards wider contacts and interfaces. When the contact is wider than a single atomic chain, the Planck distribution functions Eq. (3.44) should be multiplied by the number of occupied standing magnon modes N at energy ε

3. Diffuse wave propagation and interfaces

above $g\mu_B B$. Using the approximation for wide contacts with cross section $S_C \gg (2\pi/k)^2$ this becomes

$$N(\varepsilon) = \frac{S_C}{4\pi} \frac{1}{\hbar FS} \varepsilon. \quad (3.46)$$

Using this in Eq. (3.44) in the limit $B \gg \Delta B$ we find that for a wide contact the resistance R_m is multiplied by $2\pi\hbar FS / (S_C g\mu_B \Delta B)$.

When magnon transport between two different ferromagnetic materials (with different spin wave stiffness) is studied, the quadratic dispersion makes the problem very similar to that of electron transport between two free-electron-like metals with different effective electron mass. In this case, interface properties obviously play a role in the transport of magnons and the spin wave transmission coefficients have to be calculated. Also, the extension towards magnetization (spin) currents through interfaces between bulk ferromagnets goes along the same line as discussed earlier. We can therefore conclude that applying the Landauer-Büttiker formalism for wide interfaces and interfaces between diffusive media (with the proper correction for the Sharvin resistance) is an extension that is both widely applicable and useful in many types of elementary transport phenomena.

References

- [1] A.F. Fercher, W. Drexler, C.K. Hitzenberger, and T. Lasser, *Rep. Prog. Phys.* **66**, 239-303 (2003).
- [2] R. Snieder, in *Diffuse Waves in Complex Media*, edited by J.P. Fouque (Kluwer, Dordrecht, 1999).
- [3] S.B. Colak, D.G. Papaioannou, G.E. 't Hooft, M.B. van der Mark, H. Schomberg, J.C.J. Paasschens, J.B.M. Melissen and N.A.A.J. van Asten, *Appl. Opt.* **36**, 180 (1997).
- [4] R. Aronson, *J. Opt. Soc. Am. A* **12**, 2532 (1995); J. Ripoll, and M. Nieto-Vesperinas, *ibid. A* **16**, 1947 (1999); J. Ripoll, and M. Nieto-Vesperinas, *ibid. A* **17**, 1671 (2000); J. Ripoll, and M. Nieto-Vesperinas, *ibid. A* **18**, 940 (2001); S.A. Walker, D.A. Boas, and E. Gratton, *Appl. Opt.* **37**, 1935 (1998).
- [5] M. Büttiker, Y. Imry, R. Landauer and S. Pinhas, *Phys. Rev. B* **31**, 6207 (1985).
- [6] E.A. Montie, E.C. Cosman, G.W. 't Hooft, M.B. van der Mark, and C.W.J. Beenakker, *Nature* **350**, 594 (1991).
- [7] L.G.C. Rego and G. Kirczenow, *Phys. Rev. Lett.* **81**, 232 (1998).
- [8] F. Meier, and D. Loss, *Phys. Rev. Lett.* **90**, 167204 (2003).
- [9] K. Schwab, E.A. Henriksen, J.M. Worlock, and M.L. Roukes, *Nature* **404**, 974 (2000).
- [10] M. Meschke, W. Guichard, and J.P. Pekola, *Nature* **444**, 187 (2006).
- [11] S. Datta, *Electronic Transport in Mesoscopic Systems* (Cambridge University Press, Cambridge, 1995).
- [12] Y.V. Sharvin, *Sov. Phys. JETP* **27**, 655 (1965).

References

- [13] K. Aki, and P.G. Richard, *Quantitative Seismology*, (University Science Books, Sausalito, 2002).
- [14] E.T. Swartz, and R.O. Pohl, Rev. Mod. Phys. **61**, 605 (1989).
- [15] K.M. Schep, J.B.A.N. van Hoof, P.J. Kelly, G.E.W. Bauer, and J.E. Inglesfield, Phys. Rev. B **56**, 10805 (1997).
- [16] G.E.W. Bauer, K.M. Schep, and P.J. Kelly, J. Phys. D: Appl. Phys. **35**, 2410 (2002).
- [17] G. Chen, Appl. Phys. Lett. **82**, 991 (2003).
- [18] S. Simons, J. Phys. C **7**, 4048 (1974); J.A. Katerberg, C.L. Reynolds, Jr., and A.C. Anderson, Phys. Rev. B **16**, 673 (1977).
- [19] C. Kittel, Pys. Rev. **110**, 1295 (1958).
- [20] N.W. Ashcroft, and N.D. Mermin, *Solid State Physics*, (Saunders, Philadelphia, 1976).

References

4. INTERFACES IN DIFFUSE IMAGING PROBLEMS

4.1 *Introduction*

As discussed in the introductory chapter of this thesis, an important example of a diffuse imaging technique is diffuse optical tomography. This technique is used to image biological tissue, especially in cases where conventional imaging methods (x-ray, ultrasonic) can not be used or do not give satisfactory results. Diffuse optical tomography makes use of the fact that in the near infrared window, the transport mean free path of electromagnetic waves is much longer than the absorption length [1]. As light is non-ionizing, high intensities can be used for imaging, either in the form of pulsed (time domain), amplitude modulated (frequency domain) or continuous sources [1]. One important example is the location and characterization of anomalies in tissue, like cancer tumors in breast tissue (mammography). Solving the inverse problem, i.e. relating the scattered field to the properties and the location of the anomaly is the main challenge in this field [2].

Several methods have been developed to solve the inverse problem in diffusive media. Analytical models are mostly based on the diffusion equation, focussing on the disturbance in intensity caused by a scattering or absorbing anomaly in a homogeneous diffusive medium [3]. The methods usually rely on the assumption that the object is small compared to the medium. Numerical methods are either based on the diffusion or radiative transfer equations and use both finite element and Monte Carlo solving schemes [2, 4]. When solving the diffusion equation, numerically or analytically, boundary conditions need to be considered carefully, especially at boundaries with non-diffusive regions or abrupt interfaces [5, 6].

4.2 *Formulation of the imaging problem*

In this section we apply the concept of the interface resistance to an analytical description of a diffuse imaging problem. We use a formalism developed by

4.2. Formulation of the imaging problem

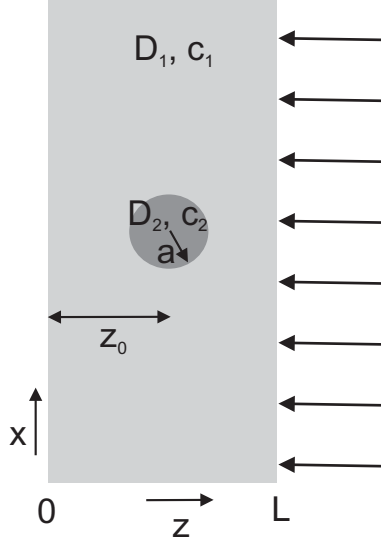


Fig. 4.1: Schematic view of the multiple-scattering system with an embedded spherical object [3].

Den Outer, Nieuwenhuizen and Lagendijk [3] that describes the disturbance in transmitted and backscattered intensity caused by an object embedded in a diffusive slab. In the present discussion we focus on scattering only and neglect absorption effects, although these can in principle be included at the cost of more complexity. The geometry is schematically depicted in Fig. 4.1. The diffusive slab is infinitely large in the x - and y -directions, stretches from $z = 0$ to $z = L$ and is characterized by a wave velocity c_1 and a diffusion constant D_1 . A spherical object with radius a , wave velocity c_2 and diffusion constant D_2 is positioned at $\mathbf{r} = (0, 0, z_0)$ inside the slab. From the right hand side the slab is illuminated by a continuous planar source and from the transmitted and backscattered intensity one would like to be able to characterize and locate the object.

The intensity distribution inside the slab and the object is obtained from the stationary diffusion equation with the proper boundary conditions. The conditions on the boundaries of the slab are $I(z = 0) = 0$ and $I(z = L) = I_0$. Solving $\nabla^2 I = 0$ inside the slab and the object has an electrostatic equivalent,

namely solving the Poisson equation for the potential in a dielectric slab with an embedded sphere with a different dielectric constant. Therefore, the concept of image charge and multipoles may be employed to find the solution [7]. When absorption is neglected and the object is spherical the “dipolar field” dominates. The intensity as a function of the position in the slab is then given by a sum over image dipoles

$$I(\mathbf{r}) = I_0 \frac{z}{L} + p \sum_{n=-\infty}^{\infty} \frac{z - z_0 + 2nL}{[(z - z_0 + 2nL)^2 + \rho^2]^{3/2}} + \frac{z + z_0 + 2nL}{[(z + z_0 + 2nL)^2 + \rho^2]^{3/2}}, \quad (4.1)$$

where $\rho^2 = x^2 + y^2$. The first part is the unperturbed intensity and the second part describes the perturbation caused by the object. An expression for p is obtained from the boundary conditions. Inside the spherical object the intensity is in leading order a linear solution of the diffusion equation

$$I_{in}(\mathbf{r}) = A + B(z - z_0). \quad (4.2)$$

Just outside the object the intensity is described by Eq. (4.1), which in this region is approximated by

$$I_{out}(\mathbf{r}) \approx I_0 \frac{z}{L} + p \frac{z - z_0}{|\mathbf{r} - \mathbf{r}_0|^3}, \quad (4.3)$$

where $\mathbf{r}_0 = (0, 0, z_0)$. If we have obtained p then the transmitted intensity $T(\rho)$ can be obtained by [8]

$$T(\rho) \equiv \frac{\ell_1 \partial I}{I_0 \partial z} \Big|_{z=0} = \frac{\ell_1}{L} + 2p\ell_1 \sum_{n=-\infty}^{\infty} \frac{\rho^2 - 2(z_0 + 2nL)^2}{[(z_0 + 2nL)^2 + \rho^2]^{5/2}}, \quad (4.4)$$

where ℓ_1 is the transport mean free path of the slab.

4.3 Smooth boundary conditions on the intensity

The picture shown in Fig. 4.1 is not exactly the one used by Den Outer et al. In their discussion, the difference in wave velocity in the two materials is neglected and it is assumed that they are characterized by a diffusion constant only. In order to relate p to the medium properties “smooth” boundary conditions are

4.3. Smooth boundary conditions on the intensity

imposed on the intensity. This means that the intensity across the interface is assumed to be continuous

$$I_{in}(a^-) = I_{out}(a^+), \quad (4.5)$$

where a^- denotes the position in the object close to the boundary and a^+ the position in the medium just outside the boundary. Furthermore, according to intensity flux conservation

$$D_1 \frac{\partial I_{out}}{\partial n} \Big|_{a^+} = D_2 \frac{\partial I_{in}}{\partial n} \Big|_{a^-}, \quad (4.6)$$

where the normal derivative is taken on the surface of the object. Applying these gives

$$A_{sm} = I_0 \frac{z_0}{L}, \quad (4.7)$$

$$B_{sm} = I_0 \frac{1}{L} \frac{3D_1}{2D_1 + D_2}, \quad (4.8)$$

and

$$p_{sm} = I_0 \frac{a^3}{L} \frac{D_1 - D_2}{2D_1 + D_2}. \quad (4.9)$$

The subscript sm denotes the smooth boundary conditions on the intensity. For $D_1 \neq D_2$ the transmitted and backscattered intensity shows either a dip or a peak at the position (in ρ) of the anomaly. If $D_2 > D_1$ light diffuses easily into the object and the transmitted intensity is enhanced. For $D_2 < D_1$ more light moves away from the object and the transmitted intensity shows a minimum near the object. The height or depth of the peak in transmitted (and backscattered) intensity depends both on z_0 and on the ratio of diffusion constants.

Now let us take a closer look at the boundary conditions used to obtain p_{sm} . When a difference in wave velocity (a refractive index mismatch) is taken into account the continuous intensity assumption is not valid anymore and an interface effect has to be taken into account. Second, the energy, not the intensity flux, is conserved by default. These two are equivalent only in the absence of a refractive index mismatch. We use $D_i = c_i \ell_i / 3$, where ℓ_i is the transport mean free path and the effective energy transport velocity is assumed to be equal to the wave velocity c_i . We rewrite

$$p_{sm} = I_0 \frac{a^3}{L} \frac{1 - \gamma \xi}{2 + \gamma \xi}, \quad (4.10)$$

with $\gamma = c_2/c_1$ and $\xi = \ell_2/\ell_1$. The smooth boundary conditions are only valid for $\gamma = 1$, so only different transport mean free paths are described properly in this way. In the following section we include an effective index mismatch and interfacial scattering properly in the boundary conditions and obtain an expression for p that is also valid for $\gamma \neq 1$ as well as interface scattering from other sources such as a coating of the object.

4.4 Including interface scattering in the boundary conditions

Effective index mismatches and interface scattering modifies the boundary conditions deduced from flux conservation. Although we derived the description for the interface resistance with acoustic waves in mind, it applies just as well to diffuse light propagation, or any type of waves, though our study is limited to a scalar approximation. Let us assume we are dealing with a monochromatic planar source. When the permeability is constant throughout the whole system the energy density in a medium (W_i) is related to the intensity by [7]

$$W_i = \frac{\chi}{c_i^2} I_i, \quad (4.11)$$

where χ is constant throughout the whole multiple scattering system. We can then relate the flux to the intensity in a diffusive medium as

$$\mathbf{F}_i = -D_i \nabla W_i = -\frac{\chi D_i}{c_i^2} \nabla I_i. \quad (4.12)$$

So, energy flux conservation left and right from the interface between the medium and the spherical object now requires that

$$\frac{D_1}{c_1^2} \left. \frac{\partial I_{out}}{\partial n} \right|_{a^+} = \frac{D_2}{c_2^2} \left. \frac{\partial I_{in}}{\partial n} \right|_{a^-}. \quad (4.13)$$

In chapter 3 we described the influence of interface scattering and refractive index mismatch on the diffuse energy current through interfaces between diffusive media. We apply this description to the medium-object interface and use the expressions for the interface resistance obtained in the previous chapter, which is a valid approximation as long as we can treat the interface as planar, i.e. $a \gg \ell_i$. If this condition is fulfilled the sharp boundary is characterized by an interface resistance SR_{Int} (in units of velocity squared), and the flux through the interface between the spherical object and the medium is related to the

4.4. Including interface scattering in the boundary conditions

potential difference across the interface by

$$F_{Int} = \frac{1}{SR_{Int}} (c_2^3 W_{in}(a^-) - c_1^3 W_{out}(a^+)) = \frac{\chi}{SR_{Int}} (c_2 I_{in}(a^-) - c_1 I_{out}(a^+)). \quad (4.14)$$

This yields the second boundary condition

$$\frac{1}{SR_{Int}} (c_2 I_{in}(a^-) - c_1 I_{out}(a^+)) = -\frac{D_1}{c_1^2} \frac{\partial I_{out}}{\partial n} \Big|_{a^+}. \quad (4.15)$$

Where SR_{Int} is given by

$$SR_{Int} = 4c_1^2 \left[\bar{T}_{12}^{-1} - \frac{1}{2} (1 + \gamma^2) \right], \quad (4.16)$$

The total transmission coefficient \bar{T}_{12} depends on the surface properties and for either a specular or a diffuse interface the expressions are given in chapter 3. Boundary conditions for refractive index mismatched problems are also described in Ref. [6], where analytical expressions are given for negligible interface resistance and numerical results for finite interface resistance are described.

With conditions (4.13) and (4.15) we obtain

$$A_{sh} = \frac{c_1}{c_2} I_0 \frac{x_0}{L}, \quad (4.17)$$

$$B_{sh} = \frac{c_2^2 D_1}{c_1^2 D_2} I_0 \frac{1}{L} \frac{3c_1^3 D_2}{2c_2^3 D_1 + c_1^3 D_2 + 2SR_{Int} D_1 D_2 / a}, \quad (4.18)$$

and

$$p_{sh} = I_0 \frac{a^3}{L} \frac{c_2^3 D_1 - c_1^3 D_2 + SR_{Int} D_1 D_2 / a}{2c_2^3 D_1 + c_1^3 D_2 + 2SR_{Int} D_1 D_2 / a}, \quad (4.19)$$

where the subscript sh denotes the sharp boundary conditions. The results for the smooth boundary are recovered if we let $c_1 \rightarrow c_2$ and $SR_{Int} \rightarrow 0$, and the results in Ref. [6] are recovered for $SR_{Int} \rightarrow 0$. If we rewrite

$$p_{sh} = I_0 \frac{a^3}{L} \frac{1}{2} \frac{1 + \frac{SR_2}{SR_{Int}} - \frac{SR_1}{SR_{Int}}}{1 + \frac{SR_2}{SR_{Int}} + \frac{1}{2} \frac{SR_1}{SR_{Int}}}, \quad (4.20)$$

then disturbance is expressed in terms of ratios of the interface resistance SR_{Int} and the bulk resistance of a layer with the width of the object radius a , $SR_i =$

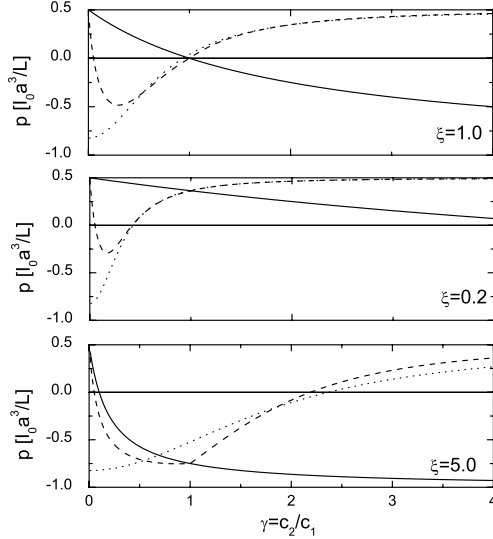


Fig. 4.2: Plots of the strength of the disturbance p as a function of the velocity ratio $\gamma = c_2/c_1$ for three different values of the transport mean free path ratio $\xi = \ell_2/\ell_1$. Solid line is the result for smooth boundary conditions (p_{sm}). Results for sharp boundary conditions (p_{sh}) with a specular interface shown by dashed line and for the diffuse interface the dotted line. For all plots $a/\ell_1 = 10$.

ac_i^3/D_i (see section 3.4). When we fill in $D_i = c_i\ell_i/3$ we can write p_{sh} in terms of the ratios $\xi = \ell_2/\ell_1$ and $\gamma = c_2/c_1$

$$p_{sh} = I_0 \frac{a^3}{L} \frac{1}{2} \frac{1 + 3 \frac{a}{\ell_1} \frac{c_1^2}{SR_{Int}} \left(\frac{1}{\xi} \gamma^2 - 1 \right)}{1 + 3 \frac{a}{\ell_1} \frac{c_1^2}{SR_{Int}} \left(\frac{1}{\xi} \gamma^2 + \frac{1}{2} \right)}. \quad (4.21)$$

The property SR_{Int}/c_1^2 is a dimensionless function of γ (see Fig. 3.4) and the ratio a/ℓ_1 needs to be large so that the interface resistance description is valid. In Fig. 4.2 we plot p as a function of the velocity ratio $\gamma = c_2/c_1$ for three different values of mean free path ratio $\xi = \ell_2/\ell_1$ (1.0, 0.2 and 5.0). We set $a/\ell_1 = 10$ so

4.5. Conclusions

that our flat interface formalism is applicable. The results for smooth boundary conditions (p_{sm}) are shown by the solid lines. Dashed lines represent results for sharp boundary conditions and a specular interface, whereas the results for sharp boundaries with a diffusive interface are shown by the dotted line. When the medium and the object are only characterized by a difference in wave velocity ($\xi = 1.0$), sharp and smooth boundary conditions give different signs for p . Of course we argued before that smooth boundary conditions only are valid only when $c_1 = c_2$, and these results clearly show that applying them to index mismatch problems gives very dissimilar results. Also for smaller (0.2) and larger (10.0) values of the mean free path ratios different boundaries give results that are only comparable when $\gamma \approx 1.0$.

The difference between a diffuse and a specular boundary is only significant for small velocity ratios, due to the fact that the difference between the two resistances is large here, as can be seen from Fig. 3.4. In other γ regimes (relevant for imaging in biological tissue) the disturbance is quite unsensitive with respect to the specific interface model, as was previously reported in numerical studies [6].

The effect of a larger diffusion constant of the object can be cancelled by interface scattering, so that $p = 0$ even when the scattering properties of object and medium are definitely not the same. This means that it is possible that objects that have distinctly different properties than the surrounding tissue can not be detected because bulk and interface scattering effects cancel. This can also be reversed, i.e. adding a particular partially reflecting coating on an object could change it from being observable to being invisible. These cloaking effects in diffusive imaging applications have not been reported before.

4.5 Conclusions

From our calculations we conclude that the interface effects can indeed be included by an interface resistance in diffuse imaging problems. When the interface is due to a refractive index mismatch between object and medium different boundary conditions are applied and this yields quite different results for the intensity perturbation, compared to when smooth boundary conditions are used. With the more widely applicable boundary conditions and the interface resistance analytical expressions for the perturbed intensity are obtained which not only improve earlier approximations, but also demonstrate that diffusive objects can be cloaked in diffusive media. When combined with the frequency-dependence of the scattering properties of the object and interface,

these expressions could be helpful for imaging biological tissue.

References

- [1] A. Yodh, and B. Chance, Physics Today **48**, 34 (1995).
- [2] S.R. Arridge, Inverse Problems **15**, R41, (1999).
- [3] P.N. den Outer, Th. M. Nieuwenhuizen and A. Lagendijk, J. Opt. Soc. Am. A **10**, 1209 (1993); J.C.J. Paasschens, and G.W. 't Hooft, *ibid.* **15**, 1797 (1998).
- [4] J. Ripoll, and M. Nieto-Vesperinas, J. Opt. Soc. Am. A **16**, 1453 (1999); S. Carraresi, T.H. Mohamed Shatir, F. Martelli, and G. Zaccanti, Appl. Opt. **40**, 4622 (2001).
- [5] R. Aronson, J. Opt. Soc. Am. A **12**, 2532 (1995); J. Ripoll, and M. Nieto-Vesperinas, *ibid.* **17**, 1671 (2000); J. Ripoll, and M. Nieto-Vesperinas, *ibid.* **18**, 940 (2001); S.A. Walker, D.A. Boas, and E. Gratton, Appl. Opt. **37**, 1935 (1998).
- [6] J. Ripoll, and M. Nieto-Vesperinas, J. Opt. Soc. Am. A **16**, 1947 (1999).
- [7] J.D. Jackson, *Classical Electrodynamics*,(Wiley, New York, 1998).
- [8] M.C.W. van Rossum, and Th.M. Nieuwenhuizen, Rev. Mod. Phys. **71**, 313 (1999).

5. RECURSIVE GREEN FUNCTIONS FOR 2D DISORDERED SYSTEMS

5.1 *Introduction*

With the ever increasing capacities of computers, both in memory and processor speed, studying systems numerically has become an important addition to analytical theories and experiments, both in condensed matter physics as in fields studying classical wave propagation. Direct solutions of the wave equation are obtained numerically for relatively clean systems, such as layered media with possibly some lateral inhomogeneities. For the propagation of waves (and electrons) in strongly disordered systems, numerical work is frequently based on solving the radiative transfer equation (equivalent to the Boltzmann equation) or the diffusion equation, since it is often not possible to solve the wave equation directly in these media. The radiative transfer approach, for example, successfully describes the energy decay of coda waves in seismology [1]. However, these methods neglect the phase of the propagating waves, describing properties of the average fields only. Under the influence of mesoscopic physics, it has become clear during the last two decades that phase effects (like interference) play a role also for waves that are scattered many times [2], even in inhomogeneous systems like the heterogeneous earth [3]. To study these effects numerically, a technique is needed that solves the wave equation in very inhomogeneous media.

Solving the wave equation by direct inversion is numerically demanding, as inversions scale with the third power of the system size. In this case one obtains the whole propagator, while most of the time, only part of this information is required. In electronic transport, the propagation of electrons in molecules or (dirty) metals and semi-conductors has been studied by directly solving the Schrödinger equation with a recursive Green function technique [4]. In this technique, large segments of the system are represented by their surface Green function, which contains the full information about how these segments react on changes in the part of the system which is studied in detail. In this way, the inversion of a single large matrix is replaced by many small matrices with a

relatively small size. It has been demonstrated that this technique is also useful to solve the classical wave equation in one-dimensional (1D) structures [5].

The recursive Green function technique for classical waves in 1D can be used to study plane wave propagation in layered structures with random thickness of individual layers. Obviously, it would be much more interesting if the propagation of pulsed sources in 3D disordered systems could be studied using this technique, as results could be directly used for applications like geophysical or medical imaging. However, even with this efficient solving scheme, treating realistic 3D systems does still seem to be numerically too expensive, especially for broadband sources. Still, solutions in 2D disordered systems (line sources and line impurities) bare in many ways much more resemblance with 3D than 1D inhomogeneous systems (see, for example, chapter 2 of this thesis).

In this chapter, we discuss solving the classical wave equation in 2D by the recursive Green function method for studying layered structures with many small lateral inhomogeneities and show that results for these systems can be translated to equivalent 3D media. We first review the theory in 1D in section 5.2 and explain the differences for 2D in section 5.3. We discuss the boundary conditions and improvements that enable us to study pulse propagation in disordered layered systems in section 5.4. As a first application we study the influence of interfacial disorder on head wave propagation (critically refracted waves). We end with a discussion and conclusions in section 5.6.

5.2 Recursive Green functions in 1D

We start with describing the recursive Green function technique for one-dimensional (1D) systems [5]. The scalar wave equation in the frequency domain reads

$$\partial_x^2 \psi + \frac{\omega^2}{c_0^2} \psi + \frac{\omega^2}{c_0^2} \left[\frac{c_0^2}{c^2(x)} - 1 \right] \psi = 0, \quad (5.1)$$

where $\psi(x; \omega)$ is the wave field amplitude, ω the angular frequency, $c(x)$ is the position-dependent wave velocity, and c_0 is a reference velocity. After discretization on a grid x_i with grid spacing $x_{i+1} - x_i = \Delta$ the differential equation becomes a finite difference equation for the wave field ψ_i evaluated at x_i . In matrix form this is written as

$$[H] |\psi\rangle = E |\psi\rangle. \quad (5.2)$$

where

$$[H] = \begin{bmatrix} \dots & & & & \\ & \varepsilon_{i-1} & \tau & 0 & \\ & \tau & \varepsilon_i & \tau & \\ & 0 & \tau & \varepsilon_{i+1} & \\ & & & & \dots \end{bmatrix}, \quad (5.3)$$

$$|\psi] = \begin{bmatrix} \dots \\ \psi_{i-1} \\ \psi_i \\ \psi_{i+1} \\ \dots \end{bmatrix}, \quad (5.4)$$

$\varepsilon_i = 1 + V_i \Delta^2 / 2$, $\tau = -1/2$, $E = \omega^2 \Delta^2 / (2c_0^2)$ and

$$V_i = V(x_i) = (\omega^2 / c_0^2) [1 - c_0^2 / c^2(x_i)]. \quad (5.5)$$

This eigenvalue equation has the same form as the problem of electrons hopping on a 1D chain with on-site potentials V_i and hopping rates τ .

As discussed before, the Green function $G(x, x'; \omega)$ associated with the classical wave equation (5.1) describes the propagation of waves emitted by a point source at x' to a receiver at position x . The matrix Green function corresponding to Eq. (5.2) is defined by

$$[\mathcal{G}] = (E[I] - [H])^{-1}, \quad (5.6)$$

with $[I]$ the identity matrix. This is the discretized form of the Green function and in the continuum limit $G(x_k, x_i; \omega) = -\tau [\mathcal{G}]_{i,k}$, i.e. the propagation from x_i to x_k is given by (i, k) of the matrix $(E[I] - [H])^{-1}$. When we invert the whole matrix, we obtain all the Green function's elements, i.e. every source-receiver combination, while in practice we are only interested in just one or a few of the matrix elements. The recursive Green function technique exploits this fact together with the tridiagonal structure and replaces the matrix inversion (of which the numerical costs scale as N_x^3 , with N_x the number of grid points) with a recursive procedure that scales linearly with N_x .

In wave propagation problems one usually uses either hard (hard wall) or absorbing boundary conditions. We study a system with a finite disordered region, sandwiched between two semi-infinite homogeneous regions, called *leads*. This is in fact equivalent to perfectly absorbing boundary conditions, since waves that enter the leads from the disordered region never return.

Let us define a disordered region between lattice sites $i = 1$ and $i = N_x$ with a source positioned at x_L and a receiver at x_M ($0 < L < M < N_x + 1$). When we decouple the system between the receiver at $i = M$ and the right part of the medium that starts at $i = M + 1$ we write

$$[\mathcal{G}]^{-1} = \underbrace{\begin{bmatrix} E - \varepsilon_{M-1} & -\tau & 0 \\ -\tau & E - \varepsilon_M & 0 \\ 0 & 0 & E - \varepsilon_{M+1} \end{bmatrix}}_{[\mathcal{G}_0]^{-1}} + \underbrace{\begin{bmatrix} 0 & 0 & 0 \\ 0 & 0 & -\tau \\ 0 & -\tau & 0 \end{bmatrix}}_{[-V]}, \quad (5.7)$$

where the infinite matrix is represented as a 3×3 matrix. The matrix $[\mathcal{G}_0]$ consists of two semi-infinite matrices that describe the system left from $i = M + 1$ (upper part) and right from $i = M$ (lower part). With the Dyson equation $[\mathcal{G}] = [\mathcal{G}_0] + [\mathcal{G}_0] [V] [\mathcal{G}]$ that is derived from Eq. (5.7) one finds that the matrix element $[\mathcal{G}]_{L,M}$ that describes the propagation from source to receiver is given by [5]

$$[\mathcal{G}]_{L,M} = [\mathcal{G}_0]_{L,M} + [\mathcal{G}_0]_{L,M} \tau \left\{ \left([\mathcal{G}_0]_{M+1,M+1} \right)^{-1} - \tau [\mathcal{G}_0]_{L,M} \tau \right\}^{-1} \tau [\mathcal{G}_0]_{M,M}. \quad (5.8)$$

The elements $[\mathcal{G}_0]_{L,M}$, $[\mathcal{G}_0]_{M,M}$ and $[\mathcal{G}_0]_{M+1,M+1}$ are elements of the matrix $[\mathcal{G}_0]$ that can be treated as two separate semi-infinite matrices, one that describes the system from $x = -\infty$ to x_M and another that describes the other half of the system.

We can also decouple the system between $i = 0$ and $i = 1$ and supposing that we know $[\mathcal{G}_0]_{0,0}$ (the solution of the surface Green function of the left homogeneous lead) we then add rows and columns to this matrix and use

$$[\mathcal{G}]_{i+1,i+1} = \left\{ \left([\mathcal{G}_0]_{i+1,i+1} \right)^{-1} - \tau [\mathcal{G}_0]_{i,i} \tau \right\}^{-1}, \quad (5.9)$$

with $\left([\mathcal{G}_0]_{i+1,i+1} \right)^{-1} = E - \varepsilon_{i+1}$ to calculate the element $[\mathcal{G}_0]_{L,L}$ of the semi-infinite matrix that describes the system from $x = -\infty$ to x_L . To obtain $[\mathcal{G}_0]_{L,M}$ and $[\mathcal{G}_0]_{M,M}$, that are both needed to calculate $[\mathcal{G}]_{L,M}$ with Eq. (5.8) we again add rows and columns until we have completed the matrix until $i = M$ by using the updating recursive relations

$$[\mathcal{G}]_{i,i+1} = [\mathcal{G}_0]_{i,i} \tau \left\{ \left([\mathcal{G}_0]_{i+1,i+1} \right)^{-1} - \tau [\mathcal{G}_0]_{i,i} \tau \right\}^{-1}, \quad (5.10)$$

and

$$[\mathcal{G}]_{i,i} = [\mathcal{G}_0]_{i,i} + [\mathcal{G}_0]_{i,i} \tau [\mathcal{G}]_{i,i+1}, \quad (5.11)$$

(here also $([\mathcal{G}_0]_{i+1,i+1})^{-1} = E - \varepsilon_{i+1}$). $[\mathcal{G}_0]_{M+1,M+1}$ is obtained by supposing that we know $[\mathcal{G}_0]_{N+1,N+1}$ (the solution of the surface Green function of the right homogeneous lead) and applying

$$[\mathcal{G}]_{i-1,i-1} = \left\{ \left([\mathcal{G}_0]_{i-1,i-1} \right)^{-1} - \tau [\mathcal{G}_0]_{i,i} \tau \right\}^{-1}, \quad (5.12)$$

with $([\mathcal{G}_0]_{i-1,i-1})^{-1} = E - \varepsilon_{i-1}$. Knowing $[\mathcal{G}_0]_{L,M}$, $[\mathcal{G}_0]_{M,M}$ and $[\mathcal{G}_0]_{M+1,M+1}$ Eq. (5.8) yields $[\mathcal{G}]_{L,M}$.

This scheme requires the solutions of the surface Green functions of the semi-infinite leads $[\mathcal{G}_0]_{0,0}$ and $[\mathcal{G}]_{N+1,N+1}$. Since in these regions the wave velocity is constant

$$[\mathcal{G}]_{i+1,i+1} = \left\{ \left([\mathcal{G}_0]_{i+1,i+1} \right)^{-1} - \tau [\mathcal{G}_0]_{i,i} \tau \right\}^{-1}, \quad (5.13)$$

and this is used iteratively to obtain the surface Green functions, or one obtains an analytical solution by substituting $[\mathcal{G}_0]_{i,i} = [\mathcal{G}]_{i+1,i+1}$. The iteration only converges by adding a (small) imaginary part η to the frequency. From the Green function $G(x_M, x_L; \omega) = -\tau [\mathcal{G}]_{L,M}$ for a certain range of frequencies, a solution in the time domain is obtained by an inverse Fourier transform.

As mentioned before, the recursive solving scheme is often used in electronic transport problems. The discrete grid points usually coincide with atomic sites with a certain onsite potential and coupling strength with (nearest) neighbours. Also the homogeneous lead - scattering region - homogeneous lead configuration resembles experiments which study transport properties of structures (metals, semiconductors or molecules) that are connected to low impedance contacts. The electronic Green function gives an electronic probability amplitude which is not an observable. However, its modulus squared can be interpreted as the probability of transmission of travelling lead states at the Fermi level.

5.3 Recursive Green functions in 2D

For 2D systems the scalar wave equation is given by Eq. (5.1) as well, with an extra y -dependence of the wave function $\psi(x, y; \omega)$ and the wave velocity $c(x, y)$, and ∂_x^2 is substituted by $\nabla^2 = \partial_x^2 + \partial_y^2$. Discretization on a square grid (x_i, y_j)

with grid spacing $x_{i+1} - x_i = y_{j+1} - y_j = \Delta$ again yields a matrix equation like Eq. (5.2). This time the elements of the matrix $[H]$ are the matrices $[\tau]$ and $[\varepsilon_i]$ with size $N_y \times N_y$ and the elements of the rows $|\psi\rangle$ are row vectors with length N_y , where N_y is the number of grid points in the y -direction.

We apply periodic boundary conditions on the wave velocity in the y -direction, $c(x, y + nN_y\Delta) = c(x, y)$ for $n \in \mathbb{Z}$. Such a lateral “supercell” is a very effective method to model random disorder provided the size of this unit cell is sufficiently large [6]. In the y -direction we define a region from $y = -N_y\Delta/2$ to $y = N_y\Delta/2$ for which a certain wave velocity profile is defined. We then repeat this velocity profile for $y < -N_y\Delta/2$ and $y > N_y\Delta/2$ so that the potential becomes periodic with a primitive lattice “vector” $N_y\Delta$, see Fig. 5.1 for a schematic picture. From solid state physics we know that in this case Bloch’s theorem applies to the solutions $\psi(y)$ (omitting the x -dependence). Introducing the reciprocal lattice number q

$$\psi_q(y) = e^{iqy} u_q(y), \quad (5.14)$$

where the Bloch states $u_q(y)$ have the same periodicity as the potential

$$u_q(y + nN_y\Delta) = u_q(y). \quad (5.15)$$

The states ψ_q in different supercells are related by

$$\psi_q(y + nN_y\Delta) = e^{iqnN_y\Delta} \psi_q(y). \quad (5.16)$$

The “total” solution is a linear combination of the ψ_q s (as these are the eigenfunctions)

$$\psi(y) = \sum_{q=-\pi/(N_y\Delta)}^{\pi/(N_y\Delta)} \psi_q(y). \quad (5.17)$$

where the normalization of ψ is determined by an extra condition. The summation of runs over N_q q -points in the reciprocal lattice, where N_q is chosen such that the summation converges. The periodicity of the superlattice requires the first Brillouin zone between $q = -\pi/(N_y\Delta)$ and $q = +\pi/(N_y\Delta)$ to be considered only.

The solutions ψ_q for the unbounded periodic system are given by the matrix equation (5.2) where the elements of the matrix $[H]$ are now submatrices $[\varepsilon_i]$ and $[\tau]$ with size $N_y \times N_y$. The matrix $[\tau]$ is diagonal with elements $[\tau]_{j,j} = \tau = -1/4$. $[\varepsilon_i]$ is tridiagonal, except for two elements $(1, N_y)$ and $(N_y, 1)$ that

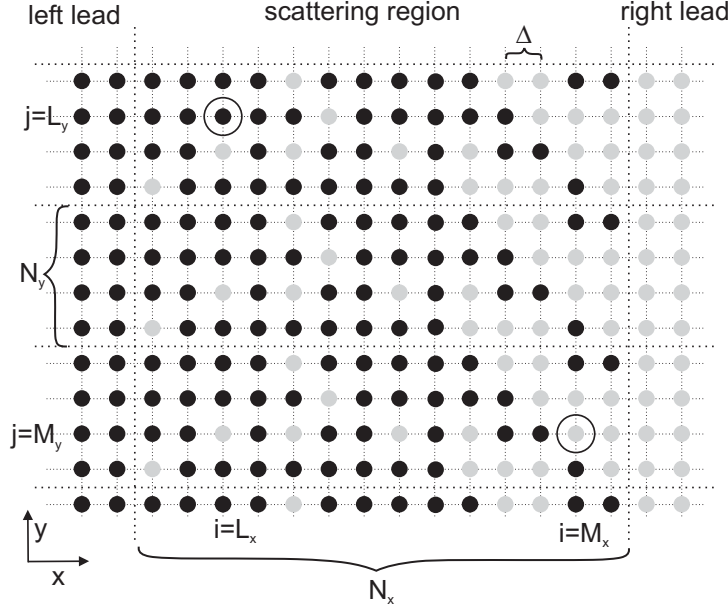


Fig. 5.1: Schematic picture of the lead-scattering region-lead configuration for the 2D recursive Green functions technique. The scattering region has a length of N_x grid points and the supercell in the y -direction has width N_y . Two different wave velocities are used in this geometry, represented by the black and grey dots. The source position (L_x, L_y) and receiver position (M_x, M_y) are represented by the black circles. In the y -direction the supercell is repeated and in the x -direction the leads are assumed to be homogeneous.

are nonzero because of the coupling to the neighbouring supercells, for example, when $N_y = 5$

$$[\varepsilon_i] = \begin{bmatrix} \varepsilon_{i1} & \tau & 0 & 0 & \tau e^{-iqN_y\Delta} \\ \tau & \varepsilon_{i2} & \tau & 0 & 0 \\ 0 & \tau & \varepsilon_{i3} & \tau & 0 \\ 0 & 0 & \tau & \varepsilon_{i4} & \tau \\ \tau e^{+iqN_y\Delta} & 0 & 0 & \tau & \varepsilon_{i5} \end{bmatrix}, \quad (5.18)$$

5.3. Recursive Green functions in 2D

with $\varepsilon_{ij} = 1 + V_{ij}\Delta^2/4$. The Green function matrix is then given by

$$[\mathcal{G}] = \sum_{q=-\pi/(N_y\Delta)}^{\pi/(N_y\Delta)} [\mathcal{G}_q] e^{iqnN_y\Delta} = \sum_{q=-\pi/(N_y\Delta)}^{\pi/(N_y\Delta)} (E[I] - [H_q])^{-1}, \quad (5.19)$$

where n is the number of supercells between the source and the receiver. The elements of $[\mathcal{G}]$ are related to the propagation of the point source at (x_{L_x}, y_{L_y}) to a receiver at (x_{M_x}, y_{M_y}) by $G((x_{M_x}, y_{M_y}), (x_{L_x}, y_{L_y}); \omega) = -\tau [\mathcal{G}]_{(L_x, L_y), (M_x, M_y)}$.

The recursion relations derived for the 1D problem in the previous section still apply, but the scalar elements are now replaced by matrices of size $N_y \times N_y$. The input for a calculation is a frequency ω , a grid spacing Δ , a reference wave velocity c_0 , the wave velocities for the left and right lead c_L and c_R , a wave velocity distribution in the disordered region c_{ij} , where $i \in [1, N_x]$, with N_x the number of grid points in the x -direction, and $j \in [1, N_y]$, with N_y the size of the supercell in the y -direction. Furthermore the source and receiver positions (x_{L_x}, y_{L_y}) and (x_{M_x}, y_{M_y}) are supplied (see Fig. 5.1) together with N_q , the number reciprocal lattice numbers q in the Brillouin zone summation and a small number η that is added as complex part to the frequency ω . The numerical procedure for 2D systems then works as follows. The calculation runs over N_q reciprocal lattice numbers q . For every q the solutions of the surface Green functions and the source-receiver propagation are calculated with the recursive relations from the previous section. An important difference now is that in every recursive step a $N_y \times N_y$ matrix is inverted. When $[\mathcal{G}]_{(L_x, L_y), (M_x, M_y)}$ is obtained for every q , the summation over the first Brillouin zone is calculated and the result $[\mathcal{G}]_{(L_x, L_y), (M_x, M_y)}$ for a certain frequency ω is obtained.

The calculations are repeated for a number of frequencies to obtain time domain results for pulsed sources. As $G(-\omega) = G^*(\omega)$ (omitting the position dependence) the inverse Fourier transform can be written as

$$G(t) = \frac{1}{\pi} \int_0^\infty d\omega \operatorname{Re} \{ G(\omega) e^{-i\omega t} \}. \quad (5.20)$$

A sharp high frequency cut-off creates undesired oscillations in the time domain. We therefore apply a smooth cut-off by multiplying G with a Fermi function $f(\omega) = 1 / (\exp((\omega - \omega_c)/s) + 1)$ so that

$$G(t) = \frac{1}{\pi} \int_0^{\omega_m} d\omega \operatorname{Re} \{ f(\omega) G(\omega) e^{-i\omega t} \}, \quad (5.21)$$

as “band limited” pulse propagator. For convenience we use this definition $G(t)$ in the remainder of this chapter. The pulse shape is calculated by

$$f(t) = \frac{1}{2\pi} \int_0^{\omega_m} d\omega \frac{\cos(\omega t)}{\exp\left(\frac{\omega - \omega_c}{s}\right) + 1}. \quad (5.22)$$

Obviously we have to chose ω_m such that the tail contribution can be neglected. The cut-off frequency ω_c and the “smoothness” parameter s are chosen in such a way the pulse shape is peaked, but side oscillations are suppressed.

5.4 Optimization and performance

As described in the previous two sections, calculating wave propagation in a disordered medium with iterative steps requires one matrix inversion in every step. Although the matrices that are inverted are small compared to the total system size, the number of steps scales with the system length, and this can be large. The numerical effort depends on the size of the matrices to be inverted and on the total number of matrix inversions. The improvements implemented by us are aimed particularly at decreasing the number of matrix inversions, since the matrix size itself is already quite small. In this section we discuss two of those optimizations together with the accuracy and the scaling of the numerical costs of the recursive Green function technique for 2D disordered systems.

5.4.1 Optimization of the lead surface Green function calculation

The solutions for the surface Green functions can be obtained iteratively, adding layer by layer, as explained in section 5.2, using the recursive relation (for 1D):

$$[\mathcal{G}]_{i+1,i+1} = \left\{ \left([\mathcal{G}_0]_{i+1,i+1} \right)^{-1} - \tau [\mathcal{G}_0]_{i,i} \tau \right\}^{-1}, \quad (5.23)$$

until $[\mathcal{G}]_{i+1,i+1} = [\mathcal{G}_0]_{i,i}$. The surface Green function can be found more efficiently by making better use of the properties of the semi-infinite matrix that describes the leads [7]. Let us start with the matrix $[\mathcal{G}_0]$ that describes the right lead stretching from $i = N + 1$ to $i = \infty$. We re-index the rows and columns so that the element we are looking for becomes $[\mathcal{G}_0]_{0,0}$ ($= [\mathcal{G}_0]_{N+1,N+1}$ in section

5.4. Optimization and performance

5.2). We know that $[\mathcal{G}_0]$ is the inverse of the semi-infinite matrix

$$[\mathcal{G}_0]^{-1} = \begin{bmatrix} E - \varepsilon_R & -\tau & 0 & 0 & 0 & \dots \\ -\tau & E - \varepsilon_R & -\tau & 0 & 0 & \dots \\ 0 & -\tau & E - \varepsilon_R & -\tau & 0 & \dots \\ 0 & 0 & -\tau & E - \varepsilon_R & -\tau & \dots \\ 0 & 0 & 0 & -\tau & E - \varepsilon_R & \dots \\ \dots & \dots & \dots & \dots & \dots & \dots \end{bmatrix}, \quad (5.24)$$

Since $[\mathcal{G}_0]^{-1} [\mathcal{G}_0] = [I]$ we find for the first column of $[\mathcal{G}_0]$

$$\begin{aligned} (E - \varepsilon_R) [\mathcal{G}_0]_{0,0} + (-\tau) [\mathcal{G}_0]_{0,1} &= 1, \\ (-\tau) [\mathcal{G}_0]_{0,0} + (E - \varepsilon_R) [\mathcal{G}_0]_{0,1} + (-\tau) [\mathcal{G}_0]_{0,2} &= 0, \\ &\dots \\ (-\tau) [\mathcal{G}_0]_{0,j-1} + (E - \varepsilon_R) [\mathcal{G}_0]_{0,j} + (-\tau) [\mathcal{G}_0]_{0,j+1} &= 0. \end{aligned} \quad (5.25)$$

Combining the first and the second equation yields

$$\tilde{\Gamma}_1 [\mathcal{G}_0]_{0,0} + \beta_1 [\mathcal{G}_0]_{0,2} = 1, \quad (5.26)$$

with $\tilde{\Gamma}_1 = (E - \varepsilon_R) - (-\tau) (E - \varepsilon_R)^{-1} (-\tau)$ and $\beta_1 = -(-\tau) (E - \varepsilon_R)^{-1} (-\tau)$. The equations for the second, third, and fourth element of the column combined give

$$\beta_1 [\mathcal{G}_0]_{0,0} + \Gamma_1 [\mathcal{G}_0]_{0,2} + \beta_1 [\mathcal{G}_0]_{0,4} = 0, \quad (5.27)$$

with $\Gamma_1 = (E - \varepsilon_R) - 2(-\tau) (E - \varepsilon_R)^{-1} (-\tau)$, which leads to

$$\tilde{\Gamma}_2 [\mathcal{G}_0]_{0,0} + \beta_2 [\mathcal{G}_0]_{0,4} = 1, \quad (5.28)$$

with $\beta_2 = -\beta_1 (\Gamma_1)^{-1} \beta_1$ and $\tilde{\Gamma}_2 = \tilde{\Gamma}_1 - \beta_1 (\Gamma_1)^{-1} \beta_1$. This leads to a recipe for finding the surface Green function by the iterative relations

$$\beta_i = -\beta_{i-1} (\Gamma_{i-1})^{-1} \beta_{i-1}, \quad (5.29)$$

$$\Gamma_i = \Gamma_{i-1} - 2\beta_{i-1} (\Gamma_{i-1})^{-1} \beta_{i-1}, \quad (5.30)$$

and

$$\tilde{\Gamma}_i = \tilde{\Gamma}_{i-1} - \beta_{i-1} (\Gamma_{i-1})^{-1} \beta_{i-1}, \quad (5.31)$$

where $\beta_0 = (-\tau)$ and $\Gamma_0 = \tilde{\Gamma}_0 = (E - \varepsilon_R)$. The asymptotic value for β_i is zero, so that when $\beta_n = 0$

$$[\mathcal{G}_0]_{0,0} = -\left(\tilde{\Gamma}_n\right)^{-1}. \quad (5.32)$$

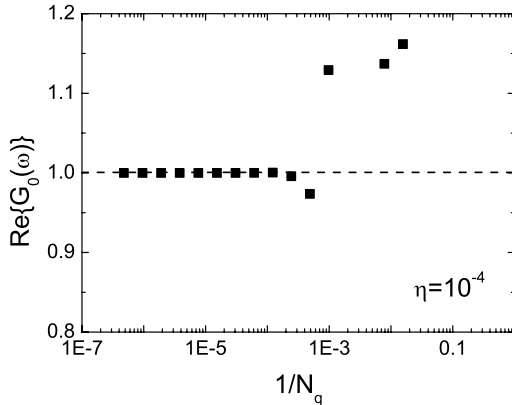


Fig. 5.2: $\text{Re}\{G_0\}/\left(\text{Re}\{G_0\}|_{N_q=2^{21}}\right)$ as a function of the inverse of the number of points in the first Brillouin zone, $1/N_q$. Convergence of the real part of the Green function is reached at $N_q \approx 2^{12}$. Dotted line is the (normalized) analytical value.

Effectively one adds 2^i layers to the semi-infinite matrix in every iteration step, which makes this procedure exponentially faster compared to the conventional “layer by layer” approach. We can directly translate this procedure from 1D systems to 2D problems by substituting the scalar elements by the matrices defined in the previous section. Both iterative procedures require the calculation of one matrix inversion in every step, so the number of inversions to be done is drastically reduced by this optimization. As a result calculating the lead solutions is reduced to a very small fraction of the numerical costs of the entire calculation.

5.4.2 Convergence as a function of N_q and η

The summation over reciprocal wave numbers q in the first Brillouin zone (the BZ integration) is equivalent to calculating an inverse Fourier transform of G with respect to y . Just as in the analytical transform of the Green function a small imaginary part has to be added to the frequency to avoid the pole at $q = 0$. In the numerical calculations this shows up as a dependence on

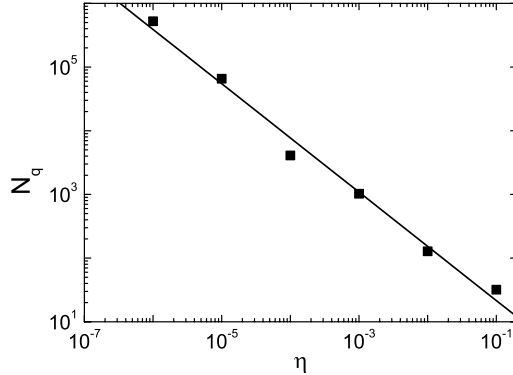


Fig. 5.3: Minimum number of points in the first Brillouin zone needed for convergence as function of η , the imaginary part added to the frequency. Solid line is a linear fit.

the number of points N_q needed for a converged BZ integration on the small imaginary part η . For a certain width ΔN_y of the supercell, a certain η and a desired accuracy one has to determine the minimum value for N_q . We calculate the real and imaginary parts of the Green function for a homogeneous 2D system $G_0(|\mathbf{r} - \mathbf{r}'|; \omega) = -iH_0^{(1)}(\omega|\mathbf{r} - \mathbf{r}'|/c_0)/4$ for $\omega = 0.1c_0/\Delta$ and $|\mathbf{r} - \mathbf{r}'| = 60\Delta$, $N_y = 5$ and $\Delta = 1$. In Fig. 5.2 the real part of G is normalized to the value calculated with the highest number of $N_q (= 2^{21})$ and plotted as a function $1/N_q$ for $\eta = 10^{-4}$. From this figure (and a similar one for the imaginary part) we conclude that convergence is reached for $N_q \approx 2^{12}$. If we do the same calculations for five other values of η ($10^{-6}, 10^{-5}, 10^{-3}, 10^{-2}$ and 10^{-1}) and plot the values of N_q where the BZ integration converges then it is clear from Fig. 5.3 that there is a linear dependence of the optimal N_q on η .

The optimum between calculation speed and accuracy has to be chosen, as strictly speaking it is $G(\omega + i\eta)$ that is being calculated. However, it is clear from Fig. 5.3 that the calculation time decreases linearly with increasing η . When we are looking for the solution in the time domain, we can use contour integration in the complex plane to use this to our advantage. With the contour shown in Fig. 5.4 the inverse Fourier transform to the time domain in Eq. (5.21)

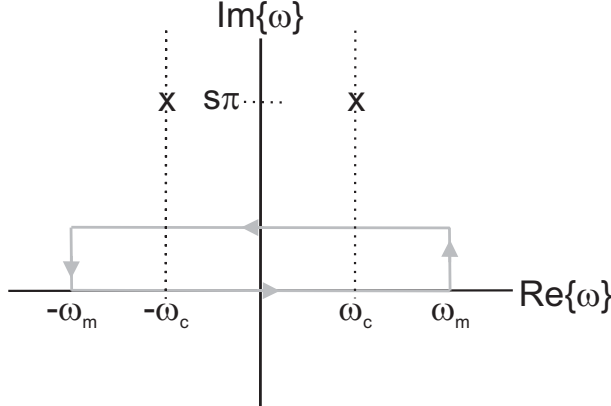


Fig. 5.4: Contour in the complex frequency plane used to calculate the band-limited pulse propagator $G(t)$.

is rewritten to give

$$\begin{aligned}
 G(t) = & \operatorname{Re} \left\{ e^{\eta t} \frac{1}{\pi} \int_0^\infty d\omega e^{-i\omega t} G(\omega + i\eta) f(\omega + i\eta) \right\} \\
 & + \operatorname{Im} \left\{ \frac{1}{\pi} e^{-i\omega_m t} \int_0^\eta d\varepsilon e^{i\varepsilon t} G(\omega_m + i\varepsilon) f(\omega_m + i\eta) \right\}. \quad (5.33)
 \end{aligned}$$

This is only allowed if there are no poles inside the contour. Causality requires that all poles of G lie in the lower part of the complex plane. The poles of the Fermi function f are given by $\omega = \omega_c + is\pi(2n + 1)$, $n \in \mathbb{Z}$, so this expression can only be used for $\eta < is\pi$. For calculations it is most convenient if only the first integral needs to be calculated (because one then can work with a single η and one N_q) and the second integral can be neglected. This can be done whenever $(\omega_m - \omega_c)/s \gg \eta t$. This determines up to which frequency we should calculate the Green function as $\omega_m - \omega_c \gg s\eta t$.

5.4.3 Numerical accuracy and scaling of the numerical costs

The code was programmed in Fortran90 and compiled with the Intel ifort compiler where standard LAPACK routines were used for the matrix inversions.

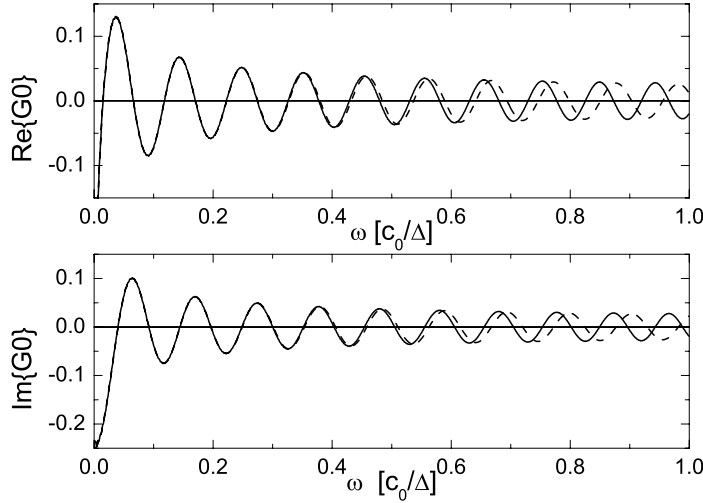


Fig. 5.5: Real (upper panel) and imaginary (lower panel) part of $G_0(|\mathbf{r} - \mathbf{r}'|; \omega)$ as a function of ω in units of Δ/c_0 with $|\mathbf{r} - \mathbf{r}'|/c_0 = 60\Delta/c_0$. Solid line is the numerical, and the dashed line the analytical result. See text for other relevant parameters.

In Fig. 5.5 the Green function of a homogeneous 2D system is plotted in the frequency domain. The dashed line is the analytical result (see chapter 1) and the solid line is the numerical calculation using the 2D recursive Green functions technique. For this calculation source and receiver were positioned 60 grid points apart and we used $\Delta = 1$, $\eta = 10^{-4}$, $c_0 = c_R = c_L = 1.0$, $N_q = 2^{12}$ and $N_y = 5$ (although in the homogeneous case a supercell of one grid point is sufficient). It is clearly seen from this plot that finite grid size causes a significant deviation from the analytical result for $\omega\Delta/c_0 = 0.5$. Obviously, the maximum frequency (or the grid spacing) has to be chosen such that the wavelength is not too short so that the properties of the discrete grid start to play a role. For shorter wavelengths Δ should be decreased. As a rule of thumb we adopt for

the maximum frequency at which finite grid effects are still small by

$$\omega_m = 0.5 \frac{c_{\min}}{\Delta}, \quad (5.34)$$

where c_{\min} is the lowest (bulk) wave velocity in the medium.

The choice of the pulse properties (bandwidth, side oscillations etc.) and the time interval we want to study differs from case to case. The number of frequencies to be evaluated and the value of η varies as well. For every frequency approximately $N_x N_q$ matrices of size $N_y \times N_y$ are inverted, so the numerical costs scale like $N_x N_y^3 N_q \propto N_x N_y^2 / \Delta$.

5.5 Results: Head waves and disordered interfaces

By imposing periodic boundary conditions in the y -direction, we restrict the type of lateral disorder. The most important limitation is the scale of (lateral) inhomogeneities; they should be small compared to the size of the supercell. In the perpendicular x -direction we can introduce an arbitrary layered structure, our method therefore allows us to study layered media with lateral disorder that consist of many small scatterers. Such a model should quite realistically represent the earth's subsurface. In order to test our code and to show that it can in principle be used for such applications, we investigate the effects of interface disorder on head wave propagation.

The basic theory for head wave propagation for at interfaces is explained in the introductory chapter [8, 9]. Head waves are critically refracted waves with a travel path along the interface between two media. The head wave arrival time in a pulse propagation experiment depends linearly on the wave velocity of the lower lying medium and the source-receiver distance. In the case of 2D media (line sources), analytical expressions can be obtained for the reflected wave field of a delta pulse. However, non-abrupt interfaces, interface roughness and other inhomogeneities influence head wave propagation. A few studies treat head waves at rough interfaces in the far and near field limits [10]. With the recursive Green functions method we are not restricted to these limits, we can study frequencies in the far field, the near field as well as in the intermediate regime. We use our method to study the influence of two types of interfacial disorder (smooth interfaces and interface roughness) on the head wave amplitude and arrival times.

5.5.1 Headwaves and smooth interfaces

As a first step we calculate the reflection of a (band-limited) pulse emitted at $t = 0$ by a source in a semi-infinite medium with wave velocity c_1 from a differentiable interface with another semi-infinite medium with wave velocity $2c_1$. The wave velocity in the interfacial region is parametrized by

$$c_{int}(x) = c_1 \left(1 + \frac{1}{\exp(-(x - x_0)/a) + 1} \right), \quad (5.35)$$

where x_0 is the distance from the interface to the source at $x = 0$, and a is a parameter that determines the width of the transition of the wave velocity from c_1 to $2c_1$. The pulse response between the source and a receiver at $(x_M = 0, y_M)$ is calculated for four different source-receiver distances $y_M = x_0$, $y_M = 2x_0$, $y_M = 3x_0$ and $y_M = 4x_0$, where $x_0 = 60l$, with l the unit length. Since there is no lateral disorder, the unit cell size in the y -direction is $N_y = 1$, and matrix inversions reduce to scalar divisions. The bandwidth of our pulse is set by choosing $\Delta = 0.1l$, so that $\omega_m = 5c_1/l$. We calculate the response in the frequency domain for 250 frequencies on a equidistant ω grid, with a small imaginary part $\eta = 2.5 \times 10^{-3}$, and for the inverse Fourier transform of Eq. (5.21) pulse-shape parameters $\omega_c = 2.5$ and $s = 1/3$. One unit length l then roughly corresponds to the shortest wavelength in the pulse. The pulse is then a superposition of frequencies in the near field, the far field and the intermediate regime, with a width in time of approximately $5l/c_1$.

From the calculated response $G(t)$ we subtract the response of the homogeneous medium $G_0(t)$ in order to separate the direct arrival from the reflection response $G_r(t)$. The results of the calculations are given in Fig. 5.6 where in every panel the response of a sharp interface (grey solid line) and the response for three different smooth interfaces (black lines) are plotted. The corresponding interface velocity profile is shown in the inset of the upper left panel, with c_{int} from Eq. (5.35). The solid line represents $a = 0.5$, the dashed line $a = 1.0$ and the dotted line $a = 2.0$.

The upper left panel shows the response measured at $y_M = x_0$. The reflection angle is below the critical angle $\theta_c = \pi/6$. The width of the reflected pulse increases with increasing interface width, because of the dispersive interface transmission and reflection. The reflection angles for the configurations of the other three panels are larger than θ_c , so almost all energy is reflected. In the upper right panel, for $y_M = 2x_0$, the head wave and directly reflected arrivals are not clearly separated yet, but for $y_M = 3x_0$ and $y_M = 4x_0$ the two separate arrivals are clearly visible. Comparing the reflection response for the

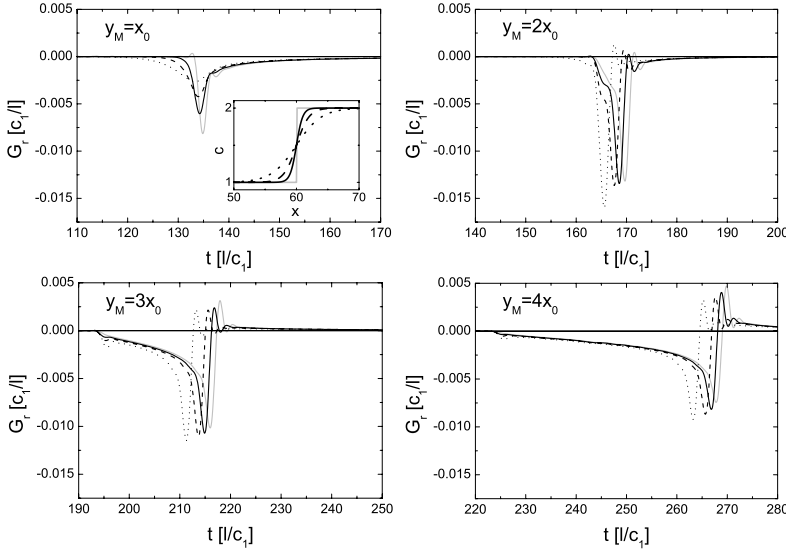


Fig. 5.6: The reflected broadband pulse response G_r from a smooth interface for four different source-receiver configurations. The grey solid lines show the response for a sharp interface and the black lines represent the response for interfaces with different widths. In the inset of the upper leftt panel the sound velocity profile in the interface region is plotted for the four cases.

sharp interface (solid grey line) with the most smoothly varying interface we observe that the direct reflection arrives earlier. Interestingly, the head wave arrival is not influenced by the gradual interface with even a slightly enhanced amplitude in the front of the head wave arrival.

5.5.2 Head waves and rough interfaces

With the recursive Green function method we are able to include fluctuations of the wave velocity in the y -direction, as long as the lengthscale of these fluctuations is smaller than the width of the lateral supercell. We can simulate the expected self-averaged results in random systems by averaging properties like

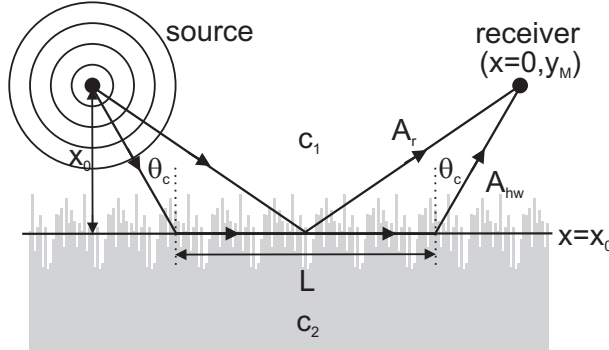


Fig. 5.7: Schematic representation of the paths of the directly reflected pulse and the head wave contribution from a rough interface. The size of the lateral supercell determines the periodicity of the interface roughness.

the amplitude or intensity over several ensemble configurations. To study the influence of surface roughness on the head wave arrival time and amplitude with our code, we use a random interface model to simulate the disorder. Here we vary the height of the (sharp) interface randomly between $x = 50$ and $x = 70$ (normalized at $x = 60$), schematically depicted in Fig. 5.7. Along the interface, the wave velocity then varies on the length scale of the grid spacing, which is much less than any wavelength. This interface structure is repeated in the y -direction with the width of the lateral supercell. We calculate the reflected response in the time domain for a source emitting a broadband pulse at $t = 0$, where we used the same pulse parameters as for the smooth interface.

The time traces of G_r for four different source-receiver distances are plotted in Fig. 5.8, for one interface configuration (black solid lines). The grey solid lines represent the response for the sharp interface. The arrivals of the reflected energy for this configuration are plotted in the four panels of Fig. 5.9, where for comparison the reflections from the smooth interface are included (black dotted lines) as well. For these calculations the width of the supercell is $8l$, or $N_y = 80$ grid points and the calculation of the reflection response for four other configurations of the disordered interface yields similar pictures. The weak dependence on the detailed random configuration indicates that we reached the self-averaging regime for this width of the unit cell.

We also study the dependence on the size of the lateral supercell, by calcu-

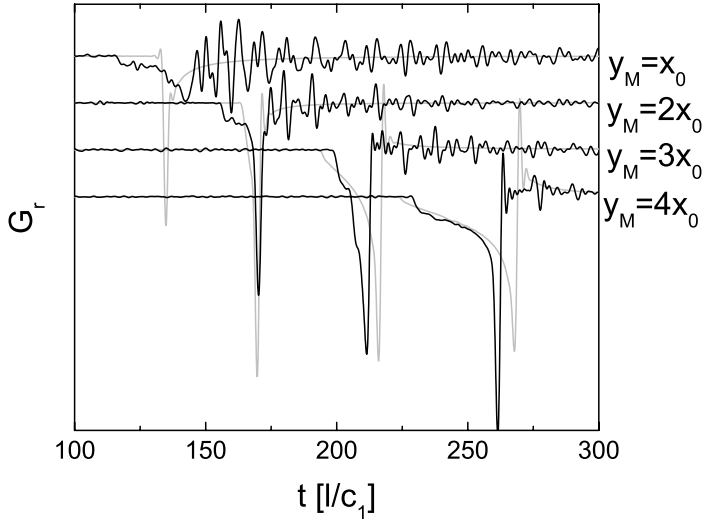


Fig. 5.8: The reflected response G_r for one configuration of the rough interface for four different source-receiver configurations (black lines). The grey lines represent the response for the sharp interface.

lating the response for $y_M = 3x_0$ for ten different configurations for $N_y = 5, 10, 20$ and for 5 different configurations for $N_y = 40$. With the smaller unit cells, the differences in the response between different configurations increase as, for example, the fluctuations in the arrival times for the head wave and direct reflection arrival increases. However, the configuration averaged arrival times do not depend on the width of the supercell. We attribute this to the self-averaging effect of our random interface model. We also did not find clear signs of coherent oscillations in the scattered field, which one might expect to show up as a signature of a periodic potential when the width of the unit cell is smaller than some of the wavelengths.

In the plots of Figs. 5.8 and 5.9 we clearly observe that the head wave arrival is delayed when the interface is rough and that delay seems to be independent of the detector off-set. Furthermore, for $y_M = x_0$ and $y_M = 2x_0$ the direct reflection from the rough interface arrives after the reflected arrivals of the

5.5. Results: Head waves and disordered interfaces

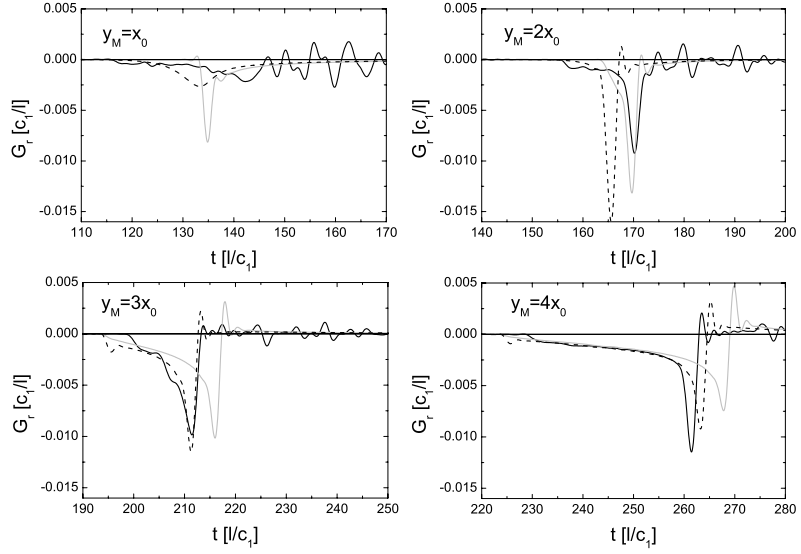


Fig. 5.9: The arrival of the reflection in the reflection responses G_r for four different source-receiver configurations. Black solid lines represent the results for a rough interface, grey solid lines the sharp interface and the black dotted line the gradual interface.

sharp and smooth interfaces, while for larger source-receiver off-sets this arrival is accelerated compared to both the smooth and sharp interfaces. Besides the head wave and direct reflection, some scattered waves are observed after these arrivals in every panel. The ratio of the amplitude of the scattered waves over the amplitude of the reflection arrival is largest for the narrow-angle reflection.

The average head wave arrival time is approximately $4l/c_1$ delayed compared to the arrivals for the smooth and sharp interfaces, for both $y_M = 3x_0$ and when $y_M = 4x_0$. It appears that the head wave velocity is not affected by the interface roughness. The constant delay indicates that the effective head wave propagation path is shifted down in the presence of randomness. On the other hand, the accelerated arrival of the direct reflection can be explained by a shift of the effective reflecting interface in the opposite direction since at

higher angles of incidence, the directly reflected waves are primarily affected by the peaks in the random interface. The time between head wave arrival and directly reflected arrival therefore becomes shorter when compared to the sharp and smooth interface studies. The ratio between head wave arrival and primary reflection as a function of the source-receiver distance differs in the case of a rough interface. If not taken into account these effects could distort seismic images. On the other hand, it could possibly be used to image properties of rough interfaces.

We finish the discussion on the results of our calculations by looking closer at the scattered field of the response of the disordered interface for the narrow angle reflection when $y_M = x_0$. In Fig. 5.10 the intensity and amplitude averaged over five different ensemble configurations are plotted. Although this is an average over a relatively small number of ensembles, and the speckle is not well averaged out, it is clear that the averaged amplitude of the waves that arrive after the direct reflection vanishes. The intensity does not, so this part is the averaged coda that results from (multiple) scattering of waves at the disordered interface.

5.6 Conclusions and discussion

With the head wave calculations in layered 2D media with lateral disorder, we have demonstrated that the recursive Green function method can indeed be useful to solve the classical wave equation for complex media. The main conclusion from these calculations is that interface roughness shortens the time between the head wave arrival and the arrival of the directly reflected waves and that this is an interface effect, i.e. it depends on the interface properties. This effect could lead to possible errors for seismic imaging when interfaces are rough. When it can be seen as a signature of the interface, the dependence of the ratio between head wave arrival and direct reflection arrival as a function of the source-receiver distance might reveal information about the interface topography and could possibly be used for imaging interface properties. Our results are obtained for 2D media, but we expect that our conclusions about the arrival times are general enough to be applicable to point sources in 3D media as well, although the shape of the head waves and the dependence of their amplitude on distance will differ in this case, of course.

The optimizations discussed in this chapter reduce the numerical effort such that the broadband reflection response for rough interfaces with supercells of up to 80 grid points can be obtained on a pc. However, other optimization can make the code even faster. For the head wave calculations, the layers between

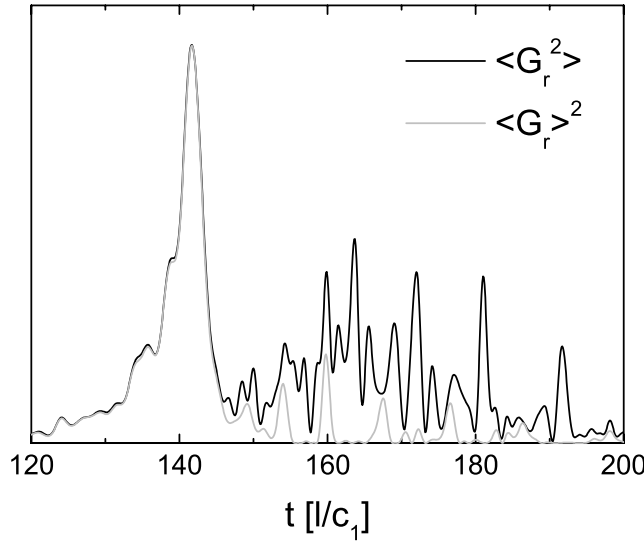


Fig. 5.10: Configuration averaged intensity $\langle G_r^2 \rangle$ (black line) and the square of the configuration averaged amplitude $\langle G_r \rangle^2$ (grey line) for a narrow angle reflection ($y_M = x_0$) on a rough interface. Average over five configurations.

$x = 0$ and $x = 50$ are presently treated as inhomogeneous, although they are not. Along the same lines as we optimized the calculation of the surface Green function it should be possible to find the bulk Green function at $x = 50$, so that we can decrease the size of the system in the x -direction by 500(!) grid points. Furthermore, finding a clever way to sample the second integral in Eq. (5.33), would allow us to increase η even further, so that even less lattice vectors in the first Brillouin zone need to be evaluated.

There are other potentially interesting applications for the recursive Green function method. By including bulk disorder (small scatterers) in the layers we could directly study the multiple scattered field (or coda) from the propagating pulse. Relating the properties of these multiple scattered waves to the properties of the medium, i.e. the inverse problem, is an ongoing scientific challenge.

Another interesting study is the influence of anisotropic scatterers, for example needles instead of point scatterers. The anisotropic scattering and diffusive properties of complex systems containing these impurities has received attention in the literature lately, both in experimental and theoretical work [11]. Studying localization effects in these media is also an interesting topic, although one has to carefully avoid artefacts of the periodicity of the potential in this case.

References

- [1] H. Sato, and M.C. Fehler, *Seismic Wave Propagation and Scattering in the Heterogeneous Earth*, (Springer-Verlag, New York, 1998).
- [2] M.P. van Albada, and A. Lagendijk, Phys. Rev. Lett. **55**, 2692 (1985); A. Tourin, A. Derode, P. Roux, B.A. van Tiggelen, and M. Fink, *ibid.* **79**, 3637 (1997).
- [3] E. Larose, L. Margerin, B.A. van Tiggelen, and M. Campillo, Phys. Rev. Lett. **93**, 048501 (2004).
- [4] A.R. Williams, P.J. Feibelman, and N.D. Lang, Phys. Rev. B **26**, 5433 (1982); A. MacKinnon, Z. Phys. B **59**, 385 (1985).
- [5] M.S. Ferreira, G.E.W. Bauer, and C.P.A. Wapenaar, Ultrasonics **40**, 355 (2002).
- [6] K. Xia, P.J. Kelly, G.E.W. Bauer, I. Turek, J. Kudrnovský, and V. Drchal, Phys. Rev. B **63**, 064407 (2001); M. Zwierzycki, Y. Tserkovnyak, P.J. Kelly, A. Brataas, and G.E.W. Bauer, *ibid.* **71**, 064420 (2005); K. Xia, M. Zwierzycki, M. Talanana, P.J. Kelly, and G.E.W. Bauer, *ibid.* **73**, 064420 (2006).
- [7] M.P. López Sancho, J.M. López Sancho, and J. Rubio, J. Phys. F **15**, 851 (1985).
- [8] K. Aki, and P.G. Richards, *Quantitative Seismology*, (University Science Books, Sausalito, 2002).
- [9] A.T. de Hoop, Applied Science Research **B8**, 349 (1960).
- [10] I. Lerche, J. Acoust. Soc. Am. **82**, 319 (1987); G.C. Bishop, and J. Smith, J. Acoust. Soc. Am. **91**, 744 (1992); J.A. DeSanto, and P.A. Martin, J. Acoust. Soc. Am. **102**, 67 (1997); R.J. Greaves, and R.A. Stephen, J. Acoust. Soc. Am. **108**, 1013 (2000); F. Buiochi, O. Martínez, L. Gómez-Ullate, and F.

References

Montero de Espinosa, IEEE Trans. on Ultrasonics, Ferroelectrics, and Frequency Control, **51**, 181 (2004).

[11] P.M. Johnson, B.P.J. Bret, J. Gómez Rivas, J.J. Kelly, and A. Lagendijk, Phys. Rev. Lett. **89**, 243901 (2002); B.P.J. Bret, and A. Lagendijk, Phys. Rev. E **70**, 036601 (2004); R. Sapienza, D.S. Wiersma, C. Cheung, A.G. Yodh, and D. Delande, in Photonic Metamaterials: From Random to Periodic on CD-ROM (The Optical Society of America, Washington, DC, 2006), ThB6; B.C. Kaas, private communications.

References

SUMMARY

In this thesis we study wave propagation in inhomogeneous media. Examples of the classical (massless) waves we consider are acoustic waves (sound) and electromagnetic waves (light, for example). Interaction with inhomogeneities embedded in a reference medium alter the propagation direction, velocity and amplitude of waves. We describe the properties of these (multiple) scattering processes to answer some questions in the field of waves in complex media, both on a fundamental level and from the point of view of applications.

In the introductory chapter we motivate our research by discussing two applications for which studying wave propagation in inhomogeneous media is essential, namely seismic exploration to image the earth's subsurface, and diffuse optical tomography (DOT) with near infrared (NIR) light for medical imaging purposes. Both imaging techniques detect waves that are emitted by a source and scattered by inhomogeneities to obtain information about the medium under study. In seismic exploration and seismology the scientific challenge is to relate the properties of multiply scattered waves, that form the seismic coda in seismograms, to the properties of the inhomogeneous subsurface. In DOT, an alternative method in medical imaging for tumor detection in breast tissue and brain oxygenation studies, diffuse light is used to image objects embedded in biological tissue. Here reconstructing the properties of the objects requires quite some study, as the inverse problem is ill-defined and forward modelling of wave propagation in diffusive media requires careful consideration of the boundary conditions. As wave propagation in different fields is described by the same wave equation, formalisms describing (multiple) scattering that are developed in a certain field can also be applied to problems in a totally different one.

Chapter 2 discusses propagation of monochromatic waves in one-, two- and three-dimensional (3D) inhomogeneous media. Here, the complex medium is an acoustic reference medium with many embedded, similar, spherical scatterers with a finite radius smaller than the wavelength. The waves from the monochromatic point source are scattered by the inhomogeneities, which are characterized by an acoustic wave velocity contrast with the reference medium. In the fre-

quency domain, we calculate the configuration averaged amplitude, intensity, energy flux and energy density in the independent scatterer approximation and the ladder approximation to the Bethe-Salpeter equation. This relates the microscopic scattering properties of the individual scatterers to the macroscopic properties of the effective medium. We obtain expressions for the (gradient of the) averaged intensity in the medium for all source-receiver distances, which enables us to study the crossover regime between ballistic and diffuse wave propagation. We find that the crossover contribution is small for 2D and 3D media, and that the intensity everywhere in the medium is well approximated by just the superposition of the ballistic and totally diffuse contributions. We obtain expressions for the frequency dependent effective medium properties, such as the mean free path and the effective transport velocity. Resonances that can be attributed to the single scatterer resonances become important when the wave velocity inside the scatterer is much lower than the reference velocity. By Fourier transforming the configuration averaged intensity in the frequency domain we obtain the averaged time domain correlator of a short pulse. We show that the internal scatterer resonances are responsible for long time-scale triangular oscillations in the averaged correlator.

In chapter 3 we study boundary conditions between scattering objects. We formulate these by applying the Landauer-Büttiker formalism, that was originally developed to describe electronic currents in mesoscopic structures, to classical waves. We focus on acoustic waves, but the results apply to any type of classical (scalar) waves. We find expressions for the energy current between two large (black body) reservoirs coupled through leads and a constriction that is much wider than the wavelength. When the system is homogeneous we find that the energy current depends on the difference in energy density between the reservoirs and the resistance of the constriction. In the case that the wave velocities on the left and the right from the constriction differ, the driving potential is the energy density times the velocity cubed. Also, the scattering properties of the interface have to be taken in to account when calculating the resistance. This resistance is calculated analytically for two cases: the specular (clean) interface, and the diffuse (dirty) interface. We then extend this discussion to interfaces between semi-infinite 3D diffusive media. In this case, the diffusive media become the reservoirs and the interface resistance is obtained by simply correcting for the absence of the constriction. We show how analogies between different types of wave propagation can be exploited and apply this formalism to the thermal boundary resistance and the transport of spin waves (magnons) through interfaces between ferromagnets.

In chapter 4 we apply the concept of the interface resistance to a diffuse

imaging problem. When a continuous light source illuminates a diffusive slab of width L , an embedded (diffusive) object with different scattering properties affects the light propagation. The disturbance to the transmitted and backscattered light can be measured in order to localize and characterize the object. The properties of the disturbed intensity can be expressed in terms of the position of the object, its size and diffusion constant by solving the diffusion equation with the appropriate boundary conditions. With the formalism developed in chapter 3 we can take into account a refractive index mismatch between object and medium, and other types of interface scattering in the boundary conditions. We find that in case of a wave velocity mismatch it is essential to take the interface properties into account in order to be able to characterize the object correctly. Furthermore, we find that in some cases bulk and interface scattering effects cancel and the object (with clearly different properties than the medium) becomes invisible for the imaging technique (cloaking in diffusive media). Including boundary conditions for interface scattering in a physically transparent way by introducing an interface resistance is potentially useful for diffuse imaging techniques like diffuse optical tomography.

The fifth and final chapter of this thesis deals with a numerical method, the recursive Green function technique, to solve the classical wave equation in 2D media. Using absorbing boundary conditions in the x -direction and periodic boundary conditions on the potential in the y -direction, the method can be used to study the propagation of cylindrical waves in layered media with short-lengthscale lateral disorder. We discuss the principles of the method and the optimizations that are needed to study the propagation of pulsed signals. With this method we look at the influence of interface disorder on the propagation of (critically) refracted head waves. We compare the head waves from a sharp interface (jump in wave velocity from c to $2c$) to those from smooth interfaces (gradual change from c to $2c$), and from a disordered interface (where the interface roughness is periodic with the width of the supercell in the y -direction). We find that the interface roughness affects the arrival time of both the head waves and the directly reflected waves, when compared to the arrivals from the sharp and smooth interfaces. This effect could possibly cause errors in seismic imaging when interfaces are rough. It might also be possible to use the shape of the head wave arrival in a seismogram to image the topography of the interface.

SAMENVATTING

In dit proefschrift bestuderen we golfpropagatie in inhomogene media. Voorbeelden van de klassieke (massaloze) golven die we beschouwen, zijn akoestische golven (geluid) en elektromagnetische golven (licht, bijvoorbeeld). Interactie met inhomogeniteiten in een referentiemedium veranderen de propagatierichting, snelheid en amplitude van golven. We beschrijven de eigenschappen van deze (veelvoudig) verstrooiende processen om vragen te beantwoorden op het gebied van golven in complexe media, zowel van fundamentele als van toepassingsgerichte aard.

In het inleidende hoofdstuk motiveren we ons onderzoek door twee toepassingen te bespreken waarvoor het bestuderen van golfpropagatie in inhomogene media belangrijk is; namelijk seismische exploratie voor beeldvorming van aardlagen, én diffuse optische tomografie (DOT) met nabij infrarood (NIR) licht voor medische beeldvorming. Beide beeldvormingstechnieken detecteren golven, die uitgezonden zijn door een bron en verstrooid door inhomogeniteiten, om informatie te vergaren over het medium dat wordt onderzocht. De wetenschappelijke uitdaging in de seismische exploratie en de seismologie is het relateren van de eigenschappen van de veelvoudig verstrooiende golven, die deel uit maken van de seismische coda in seismogrammen, aan de eigenschappen van de inhomogene ondergrond. In DOT, een alternatieve methode in de medische beeldvorming om of tumoren te detecteren in borstweefsel of het zuurstofgehalte in de hersenen te bepalen, wordt diffuus licht gebruikt om een beeld te vormen van objecten in biologisch weefsel. Hier vergt het reconstrueren van de eigenschappen van de objecten veel studie, aangezien het inverse probleem slecht is gedefinieerd. Daarnaast is voor het modelleren van golfpropagatie in diffuse media een zorgvuldige behandeling van randvoorwaarden nodig. Daar golfpropagatie in verschillende gebieden beschreven wordt door dezelfde golfvergelijking, kunnen formalismen die veelvoudige verstrooiing beschrijven, welke zijn ontwikkeld in een bepaald gebied, ook toegepast worden op problemen in een totaal ander gebied.

Hoofdstuk twee bespreekt propagatie van monochromatische golven in één-, twee-, en driedimensionale inhomogene media. Hier is het complexe medium

een akoestisch referentiemedium met daarin veel gelijke, sferische verstrooiers met een eindige straal kleiner dan de golflengte. De golven van de monochromatische puntbron worden verstrooid door de inhomogeniteiten, die door een contrast in akoestische golfsnelheid met het referentiemedium worden gekarakteriseerd. We berekenen de configuratie-gemiddelde amplitude, intensiteit, energieflux en energiedichtheid in het frequentiedomein met de onafhankelijke verstrooierbenadering en de ladderbenadering op de Bethe-Salpeter vergelijking. Dit relateert de microscopische verstrooingseigenschappen van de individuele verstrooiers aan de macroscopische eigenschappen van het effectieve medium. We vinden uitdrukkingen voor de (gradiënt van de) gemiddelde intensiteit in het medium voor alle bron-ontvanger afstanden, wat het mogelijk maakt om het overgangsregime tussen ballistische en diffuse golfpropagatie te bestuderen. We vinden dat de overgangsbijdrage aan de intensiteit klein is in 2D en 3D media, en dat de intensiteit overal in het medium goed benaderd kan worden door slechts de superpositie van de ballistische en de totaal-diffuse bijdrages. We verkrijgen uitdrukkingen voor de frequentie-afhankelijke effectieve mediumeigenschappen, zoals de vrije weglenge en de effectieve transportsnelheid. Resonanties, die toegeschreven kunnen worden aan de resonanties van de individuele verstrooiers, worden belangrijk wanneer de golfsnelheid in de verstrooier veel lager is dan de referentiesnelheid. Door Fouriertransformatie van de configuratie-gemiddelde intensiteit verkrijgen we de gemiddelde tijdsdomeincorrelator voor een korte puls. We laten zien dat de interne resonanties van de verstrooiers verantwoordelijk zijn voor driehoekige oscillaties in de gemiddelde correlator op een veel langere tijdschaal dan de duur van de puls.

In hoofdstuk 3 bestuderen we randvoorwaarden tussen verstrooiende objecten. We formuleren deze door het Landauer-Büttikerformalisme, dat oorspronkelijk voor het beschrijven van elektronenstromen door mesoscopische structuren is ontwikkeld, toe te passen op klassieke golven. We focussen op akoestische golven, maar de resultaten zijn toepasbaar op elk type klassieke (scalaire) golven. We vinden uitdrukkingen voor de energiestroom tussen twee grote reservoirs die verbonden zijn door een constrictie die veel wijder is dan de golflengte. Wanneer het systeem homogeen is, vinden we dat de energiestroom afhankelijk is van het verschil in energiedichtheid tussen de reservoirs en de weerstand van de constrictie. In het geval dat de golfsnelheden rechts en links van de constrictie verschillen, is de drijvende potentiaal gelijk aan de energiedichtheid maal de golfsnelheid tot de derde macht. De verstrooiende eigenschappen van het grensvlak moeten dan in acht genomen worden bij de berekening van de weerstand. Deze weerstand wordt analytisch berekend voor twee gevallen: het perfect gladde grensvlak en het diffuse (vuile) grensvlak. Vervolgens breiden

we deze discussie uit naar grensvlakken tussen halfoneindige 3D diffuse media. In dit geval worden de diffuse media de reservoirs, en de grensvlakweerstand wordt verkregen door te corrigeren voor de afwezigheid van de constrictie. We laten zien hoe analogieën tussen verschillende soorten van golfpropagatie benut kunnen worden door dit formalisme toe te passen op de thermische grensvlakweerstand en het transport van spingolven (magnonen) door grensvlakken tussen ferromagneten.

In hoofdstuk 4 passen we het concept van de grensvlakweerstand toe op een diffuus beeldvormingsprobleem. Wanneer een continue lichtbron een diffuus medium met eindige dikte L beschijnt, zal een ingebed (diffuus) object, met andere verstrooiende eigenschappen, de lichtpropagatie beïnvloeden. De verstoring van het getransmitteerde en gereflecteerde licht wordt gemeten om het object te lokaliseren en te karakteriseren. De eigenschappen van de verstoerde intensiteit worden uitgedrukt in de positie, de grootte en de diffusieconstante van het object, door de diffusievergelijking op te lossen met de juiste randvoorwaarden. Met het formalisme beschreven in hoofdstuk 3, kunnen we een brekingsindexverschil tussen object en medium en andere vormen van grensvlakverstrooing meenemen in de randvoorwaarden. We vinden dat in het geval van een verschil in golfsnelheid het essentieel is om de grensvlak-eigenschappen mee te nemen, teneinde het object goed te kunnen karakteriseren. Verder vinden we dat in sommige gevallen bulk-, en grensvlakverstrooingseffecten elkaar opheffen zodat het object onzichtbaar wordt voor de beeldvormingstechniek (hoewel de eigenschappen van het object wel duidelijk verschillen van die van het medium). Het meenemen grensvlakverstrooing in de randvoorwaarden door het introduceren van een grensvlakweerstand op een fysisch transparante wijze, is een mogelijk bruikbaar principe voor diffuse beeldvormingstechnieken als diffuse optische tomografie.

Het vijfde en laatste hoofdstuk van dit proefschrift gaat over een numerieke methode, de recursieve Greense functiemethode, om de klassieke golfvergelijking in 2D media op te lossen. Door gebruik te maken van absorberende randvoorwaarden in de x -richting en periodieke randvoorwaarden in de y -richting, kan de methode worden gebruikt om propagatie van cilindrische golven in gelaagde media met laterale wanorde te bestuderen. We beschrijven de principes van deze methode en de optimalisaties die nodig zijn om de propagatie van gepulste signalen te kunnen bestuderen. Met deze methode onderzoeken we de invloed van grensvlakwanorde op de propagatie van (kritisch) gebroken “head waves”. We vergelijken de “head waves” van een scherp grensvlak (een sprong in de golfsnelheid van c naar $2c$) met die van geleidelijke grensvlakken (geleidelijke overgang van c naar $2c$), en met die van een wanordelijk grensvlak (waarbij de

grensvlakwanorde periodiek is met de breedte van de supercel in de y -richting). We vinden dat de grensvlakwanorde de aankomsttijd van zowel de “head waves” als de direct gereflecteerde golven beïnvloedt, wanneer ze worden vergeleken met de aankomsttijden voor de scherpe en de geleidelijke grensvlakken. Dit effect kan mogelijk voor fouten zorgen in seismische beeldvorming wanneer de grensvlakken wanordelijk zijn. Dit kan mogelijk ook worden gebruikt om de vorm van de “head waves”-aankomst in een seismogram te gebruiken voor beeldvorming van de topografie van het grensvlak.

CURRICULUM VITAE

30 - 10 - 1977 Born in Zevenaar, The Netherlands.

1990 - 1996 Secondary school at the Liemers College, Zevenaar, The Netherlands.

1996 - 2002 Applied Physics at the University of Twente, Enschede, The Netherlands.

2000 Internship at the University of Technology, Sydney, Australia.
Experimental research on the optical properties and characterization of discontinuous metal films.

2001 - 2002 M.Sc. in Applied Physics under supervision of Prof. P. J. Kelly, in the group of Computational Materials Science, University of Twente, Enschede, The Netherlands.
M.Sc. research on numerical calculations on spin-dependent electron transport in ferromagnetic multilayers. Thesis title: “An ab initio calculation of the current-in-plane giant magnetoresistance of Cu/Co multilayers”.

2002 - 2007 Ph.D. in Physics under the supervision of Prof. G. E. W. Bauer, in the Theoretical Physics group, Kavli Institute of Nanoscience, Technical University Delft, The Netherlands.
Ph.D. research on methods and formalisms that describe wave propagation in disordered media. Thesis title: “Waves in inhomogeneous media”.

LIST OF PUBLICATIONS

Studying head waves from disordered interfaces with a recursive Green function technique, S. Gerritsen, J. M. Thijssen, M. S. Ferreira, and G. E. W. Bauer, (in preparation).

Interfaces in diffuse imaging problems, S. Gerritsen and G. E. W. Bauer, (in preparation).

Energy transport by classical waves through multilayers of diffusing slabs, S. Gerritsen and G. E. W. Bauer, in Photonic Metamaterials: From Random to Periodic on CD-ROM (The Optical Society of America, Washington, DC, 2006), ThD17.

Diffusion of monochromatic classical waves, S. Gerritsen and G. E. W. Bauer, Phys. Rev. E **73**, 016618 (2006).

Plasmon-mediated visible and near-infrared transmission through sub-30-nm holes in metal films: potential in solar energy applications, G. B. Smith, S. Gerritsen, M. Hossain, and G. McCredie, Proc. SPIE 4458, 29-37 (2001).